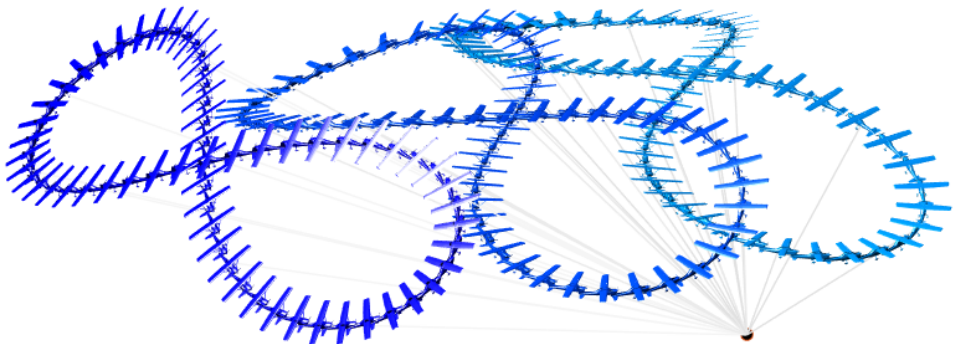


Identification and Optimization of an Airborne Wind Energy System

Giovanni Licitra



University of Freiburg
Faculty of Engineering
Department of Microsystems Engineering
Systems Control and Optimization Laboratory

18 July 2018

Identification and Optimization of an Airborne Wind Energy System

Giovanni LICITRA

Dean: Prof. Dr. Oliver Paul

Examination committee:

Supervisor/First referee: Prof. Dr. Moritz Diehl

Second referee: Prof. Dr. Lorenzo Fagiano

Observer: Prof. Dr. Lars Pastewka

Chair of committee: Prof. Dr. Christoph Eberl

Dissertation zur Erlangung des Doktor-
grades der Technischen Fakultät der
Albert-Ludwigs-Universität Freiburg
im Breisgau

18 July 2018

© 2018 University of Freiburg – Faculty of Engineering
Self-published,
Giovanni Licitra, Georges-Köhler-Allee 101, DE-79110 Freiburg i. Br. (Germany)

Alle rechten vorbehalten. Alle Inhalte dieses Werkes, insbesondere Texte, Fotografien und Grafiken, sind urheberrechtlich geschützt. Das Urheberrecht liegt, soweit nicht ausdrücklich anders gekennzeichnet, bei der Albert-Ludwigs-Universität Freiburg.

All rights reserved. No part of the publication may be reproduced in any form by print, photoprint, microfilm, electronic or any other means without written permission from Albert-Ludwigs-Universität Freiburg.

*To Michelle,
for her love, support, and patience.*

Abstract

Airborne Wind Energy (AWE) refers to systems capable of harvesting energy from the wind by flying crosswind patterns with tethered airfoils. This thesis focuses on a specific technology called *pumping mode* AWE. We consider as a case study the real plant developed by the Dutch company Ampyx Power B.V., where the airborne component is a high lift rigid wing autonomous aircraft designed for an extremely challenging operational environment.

The techniques developed within this manuscript rely on mathematical models described in state-space representation. As a consequence, the first part of the manuscript introduces a suitable mathematical representation of the case study for identification and optimization purposes.

Normally, the system identification procedure of aircraft deployed for AWE is ultimately addressed via an intensive flight test campaign in order to gain additional insight about the aerodynamic properties. For that purpose, we provide a comprehensive guideline on how to reliably identify the aerodynamic models via flight tests. More precisely, we focus on the flight test operations procedure, signal input design and parameter estimation algorithm. Additionally, we show how to optimize system identification flight tests by solving a time domain model-based optimum experimental design problem.

In an AWE system, the airfoil is required to fly in cyclic patterns to maximize net power produced per cycle. Due to the numerous variables that need to be taken into account simultaneously, the computation of efficient and feasible flight trajectories is not trivial. We show how to systematically obtain such flight trajectories via an optimal control approach. Several scenarios are analyzed in terms of control strategy, average power output, and trajectory topology. Finally, we show how many tasks relative to the scaling up of such systems can be significantly facilitated by means of the optimization algorithm developed within this work.

Zusammenfassung

In dieser Doktorarbeit werden Flugwindkraftwerke zur Nutzung von Höhenwindenergie untersucht. Als Flugwindkraftwerke werden Systeme bezeichnet, welche aus einem seilgebundenen Flügel bestehen und Höhenwindenergie ernten, indem sie auf Flugbahnen quer zum Wind geflogen werden. Als Fallstudie ziehen wir eine existierende Anlage heran, die von der niederländischen Firma Ampyx Power B.V. entwickelt wird. Deren fliegende Komponente ist ein autonom fliegendes Flugzeug mit starren Flügeln und hohem Auftrieb, welches für anspruchsvolle Betriebsumgebungen gefertigt wurde. Zur Modellierung der Flugwindkraftwerke werden in dieser Doktorarbeit mathematische Zustandsraummodelle eingeführt, welche sich zur Systemidentifikation und zur Optimierung der Flugbahnen dieser Systeme eignen.

Für die Systemidentifikation von Flugwindkraftwerken wird üblicherweise eine Reihe von Flugtests benötigt, um Informationen über die aerodynamischen Eigenschaften des Flügels zu erhalten. Zu diesem Zweck beschreiben wir eine umfassende Methode, wie aerodynamische Modelle mit Flugtests zuverlässig identifiziert werden können. Insbesondere konzentrieren wir uns auf den Ablauf der Flugtests, den Entwurf von Eingangssignalen und den Algorithmus zur Bestimmung von Parametern. Darüber hinaus zeigen wir, wie Flugtests zur Systemidentifikation durch Lösung eines modellbasierten Optimierungsproblems entworfen werden können.

In einem Flugwindkraftwerk muss der Flügel zyklische Bahnen fliegen, um die Energieproduktion pro Zyklus zu maximieren. Da eine Vielzahl von Parametern gleichzeitig betrachtet werden müssen, ist die Berechnung von effizienten und umsetzbaren Flugbahnen nicht trivial. Wir zeigen daher, wie derartige Flugbahnen über den Ansatz einer optimalen Steuerung systematisch erzeugt werden können. Mehrere Szenarien hinsichtlich Regelungs-Ansätzen, durchschnittlicher Leistungsabgabe und Topologie der Flugbahn werden untersucht. Schließlich zeigen wir, dass viele Aufgaben, die mit der Skalierung solcher Systeme verbunden sind, durch die in dieser Arbeit entwickelten Optimierungsmethoden vereinfacht werden können.

Acknowledgements

This thesis is the result of four years of research within Ampyx Power B.V. and the Systems Control and Optimization Laboratory at the University of Freiburg. I am indebted to many persons who contributed to this research.

Above all I would like to thank Michelle for her love and constant support, especially in the stressful moments when writing up my thesis. Without her I would not be the person that I am today. I am so grateful to her for taking care alone of our beautiful and smiley daughter Isabella during my time in Freiburg.

My deepest gratitude goes to my PhD mentor, Moritz Diehl, for believing in me from the start. He provided me the right tools to perform a meaningful research within the Airborne Wind Energy field. This dissertation and my future career would not have been the same without him. With his enthusiasm he was always able to motivate me during our meetings. Thanks also to the flexible working environment I had in Freiburg.

I would like to thank all the incredible people of Ampyx Power, especially Sören Sieberling and Richard Rüterkamp for their guidance, and Veerle Hellin for her administrative support. I own my sincere gratitude to Paul Williams, who has largely contributed to the academic quality of this thesis. I really appreciated his invaluable suggestions on practical topics that really matter. His impeccable precision and deep knowledge will always be an inspiration for me. I am also sincerely grateful to Jonas Koenemann for being my closest colleague during my time at Ampyx Power. We managed to get along well after sharing the flight trajectory optimization project. I am so grateful for his patience and support for all my problems in coding and Git.

A big thank you goes also to my office mates, Marco D'Alessio and Stefano Cottafavi. I will deeply miss our intense chats, walks around unit55, and coffee breaks!!!

Adrian Bürger deserves a huge thank for his help during the maneuver design phase. Together we were able to publish our first journal paper! Thanks also

for keeping a close eye on the structure of my publications.

I gratefully acknowledge the funding from the EU Marie Curie project TEMPO that allowed me to pursue my doctorate without budget limitation. It was a privilege be part of a network together with people deeply knowledgeable in the field control and optimization.

I would like to express my gratitude to all the TEMPO fellows for all the time spent together during our events, workshops and conferences. Among them, a big thank you goes to Bartomeo Stellato for being a trusted friend. I am sure you will be a great godfather for Isabella. I am grateful to all the incredible colleagues in Freiburg for the great time we had together in and outside the office. Especially, I would like to thank Andrea Zanelli and Matilde Gargiani for all the delicious dinners at their house.

Last but surely not least, I would like to thank my parents, Luigi and Lucia for their unconditional love and the significant effort they made in these years. Without them my path in life would be totally different.

Giovanni Licitra

Freiburg im Breisgau, July 2018

Contents

Abstract	iii
Zusammenfassung	v
Acknowledgements	vii
List of Abbreviations	ix
List of Symbols	xi
Contents	xi
List of Figures	xv
List of Tables	xxiii
1 Introduction	1
1.1 Introduction to AWES	2
1.2 Contributions of outline of this thesis	6
1.3 List of publications	7
2 Modeling of a Rigid Wing AWES	9
2.1 Wind profile modeling	10
2.2 Tethered aircraft modeling	10
2.2.1 Reference frames and aircraft attitude	10

2.2.2	Airframe and physical characteristics	13
2.2.3	Rigid body equations	14
2.2.4	Aerodynamic forces and moments	16
2.2.5	The Lift-to-Drag ratio	18
2.2.6	Wind axes equations for tethered aircraft	20
2.3	Tether modeling	21
2.4	Ground station modeling	24
2.5	Modeling of AWES via DAEs	26
2.5.1	Index reduction	28
2.5.2	Baumgarte stabilization	30
3	Aerodynamic Model Identification	33
3.1	Experimental design set-up	35
3.1.1	Flight test procedure and the rationale behind	35
3.1.2	Flight envelope limit detection	38
3.1.3	Flight test instrumentation	39
3.2	Grey-box model selection	39
3.2.1	Model structure selection	40
3.2.2	Model assumptions and neglected dynamics	41
3.2.3	A priori aerodynamic model	43
3.3	Design of conventional experiments	44
3.3.1	Steady condition and decoupling of dynamics	44
3.3.2	Modal analysis	46
3.3.3	Design of conventional maneuvers	47
3.3.4	Features of the 3-2-1-1 maneuver	48
3.3.5	Experimental data	50
3.4	Design of optimal experiments	53
3.4.1	Historical background and motivation	53
3.4.2	Optimum experimental design formulation	54
3.4.3	Algorithm implementation	56

3.4.4	Constraints selection	57
3.4.5	Control input initialization	57
3.4.6	Flight tests optimization	58
3.4.7	Performance assessments	62
3.4.8	Effects of parameter uncertainties on the a priori model	64
3.4.9	Signal inputs set-up and safety assessments	69
3.4.10	Experimental data	71
3.5	Aerodynamic parameter estimation	76
3.5.1	Preliminary estimation accuracy analysis	76
3.5.2	Formulation of estimation algorithm	77
3.5.3	Data fitting	79
3.5.4	Model validation	85
4	Optimization and Analysis of Crosswind Flight Trajectories	91
4.1	Formulation of an OCP for AWES	92
4.1.1	Overview of continuous time OCPs	93
4.1.2	Characterization of cost function	94
4.1.3	Characterization of the mathematical model	95
4.1.4	Characterization of path constraints	96
4.1.5	Characterization of boundary constraints	97
4.1.6	Formulation of an OCP for trajectory optimization	99
4.1.7	Algorithm initialization	100
4.1.8	Algorithm implementation	103
4.2	Flight trajectory analysis	103
4.2.1	Optimal control strategy	103
4.2.2	Reverse pumping mode	108
4.2.3	Lemniscate versus circular optimal trajectory	111
4.2.4	Size trajectory comparison and AWE wind farm	114
4.3	Algorithm validation	117
4.4	Performance analysis	123

4.4.1	Annual energy production and capacity factor	125
5	Conclusions	129
A	List of Tables	133
B	List of Figures	137
	Bibliography	143

List of Figures

1.1	Basic principle of an AWES. An Airborne Wind Energy System (AWES) can potentially reach higher altitudes where the wind resources are abundant with less material compared to conventional wind turbines.	2
1.2	Working principles of a lift mode AWES with a production (left) and consumption (right) phase. A lift mode AWES produces power by performing periodical variation of both length and tether tension. Power generation occurs during the so called reel-out phase, where the tether tension is used to rotate a drum, driving an electric generator located on the ground. A reel-in phase is required due to finite tether length. By changing the flight pattern in such a way that less lifting force is produced, the tether can be wound up with a significant lower energy investment than what was gained in the power production phase.	4
1.3	The 2 nd prototype high lift, rigid wing autonomous aircraft designed by Ampyx Power B.V. [3].	4
1.4	The 3 rd prototype high lift, rigid wing autonomous aircraft designed by Ampyx Power B.V [3] (side view).	5
1.5	The 3 rd prototype high lift, rigid wing autonomous aircraft designed by Ampyx Power B.V [3] (top view).	5
2.1	Representation of Body and NED Frame.	11
2.2	Airframe of the case study.	14
2.3	Definition of body, stability and wind axes, body angular rates $\omega^{\mathbf{b}}$ and velocity $\mathbf{v}^{\mathbf{b}}$, Euler angles (ϕ, θ, ψ) , aerodynamic states (V_T, β, α) , forces (X, Y, Z) and moments (l, m, n) of an aircraft.	16

2.4	Lift and drag coefficient with the corresponding L/D for the proposed case study. The look-up values are shown in 'x', whereas their corresponding polynomial interpolation is shown in solid line.	19
2.5	Balance of forces of a pumping mode AWES during power generation under the assumption of $\beta \approx 0$. Angles Θ and ϕ denote the elevation and roll angle, respectively, whereas $f_{t\lambda}$ corresponds to the tether tension.	21
2.6	Graphical representation of the tether drag components. The tether is modeled as a rigid link and its velocity V_t is approximated as a function of both tether length l and aircraft speed V_T	23
2.7	The ground station converts the mechanical energy from tether tension into electrical power and feeds it to the grid.	24
2.8	Graphical representation of a rigid wing pumping mode AWES. The ground station is located at the origin of a right-handed Cartesian coordinate system. Within this work the wind direction points North.	27
3.1	[Experimental data] Example of a flight test procedure for a high lift, autonomous aircraft. After a coordinated turn [99], the aircraft performs a straight flight (roll angle $\phi \approx 0$ deg) with constant airspeed $V_{T_e} \approx 20$ m/s and corresponding constant angle of attack $\alpha_e \approx -2$ deg held by elevator deflection angle $\delta_{e_e} \approx 3.5$ deg. The flight path angle γ is approximately zero prior to the gliding mode. Throughout the excitation of the longitudinal motion performed in gliding mode, the aircraft slightly descends as also shown by γ , though, the angle of attack response remain within a neighborhood of α_e . The data set is collected during the open-loop phase and despite a significant excitation of the longitudinal dynamics, the lateral motion is barely perturbed thanks to both the steady wing level flight condition and the motion stabilization via aileron δ_a and rudder δ_r deflection.	37
3.2	[Simulation data] Example of flight envelope limit detection. A badly designed maneuver is performed along the longitudinal axis via elevator deflection. The detection of flight envelope violation involves the stop of the open-loop phase, with recovery of the previous trim condition.	38

3.3	Five hole pitot tube and FCC mounted at the nose and inside the fuselage, respectively.	39
3.4	CFD of the 3 rd prototype high lift, rigid wing autonomous aircraft designed by Ampyx Power B.V. [3].	43
3.5	Example of a 3-2-1-1 maneuver with $A = 1$ and $\Delta T = 0.6$	47
3.6	Frequency content of a 3-2-1-1 maneuver with $A = 5$ and $\Delta T = 0.8$ s and analysis of the a priori aircraft modes.	50
3.7	[Experimental data] Three experimental data sets obtained through conventional maneuvers ($V_{T_e} = 20$ m/s). Average wind speed ≈ 7 m/s.	51
3.8	[Experimental data] Stabilization of lateral dynamics by δ_a and δ_r during excitation signal along the longitudinal dynamics via conventional maneuvers ($V_{T_e} = 20$ m/s). Average wind speed ≈ 7 m/s. Note that, roll rate p and roll angle ϕ appear sensitive to the turbulence, which involves a major control effort from the aileron deflection δ_a in order to both stabilize this axis and prevent flight envelope violation.	52
3.9	Optimal input design within identification procedure [90].	55
3.10	[Simulation data] Initial longitudinal response using the 3-2-1-1 maneuver (left column) and optimal response (right column). In grey line the OED constraints whereas in dark red line the flight envelope.	59
3.11	[Simulation data] Initial lateral response via aileron deflection using the 3-2-1-1 maneuver (left column) and optimal response (right column). In grey line the OED constraints whereas in dark red line the flight envelope.	60
3.12	[Simulation data] Initial lateral response via rudder deflection using the 3-2-1-1 maneuver (left column) and optimal response (right column). In grey line the OED constraints whereas in dark red line the flight envelope.	61
3.13	[Simulation data] Output response using 3-2-1-1 maneuvers. The a priori model responses are in dot line while the "true" model responses are in solid line. The output responses are in blue line for the case $\Delta \mathbf{p}_{\%} = 100\%$, green line for the case $\Delta \mathbf{p}_{\%} = 20\%$, red line for the case $\Delta \mathbf{p}_{\%} = 5\%$. Flight envelope limits in dark red dash-dot line while the enforced constraints are in grey dash line.	66

3.14 **[Simulation data]** Output response using optimized maneuvers. The a priori model responses are in dot line while the "true" model responses are in solid line. The output responses are in blue line for the case $\Delta\mathbf{p}\% = 100\%$, green line for the case $\Delta\mathbf{p}\% = 20\%$, red line for the case $\Delta\mathbf{p}\% = 5\%$. Flight envelope limits in dark red dash-dot line while the constraints are in grey dash line. 67

3.15 **[Simulation data]** Comparison between initial (dot lines) and optimal (solid lines) 1- σ confidence ellipsoids for the pair of estimates (M_q, M_α). Blue line denotes the case $\Delta\mathbf{p}\% = 100\%$, green line the case $\Delta\mathbf{p}\% = 20\%$ and red line the case $\Delta\mathbf{p}\% = 5\%$. 68

3.16 **[Simulation data]** Top view of the aircraft during loss of track caused by the optimized aileron sequence. 69

3.17 **[Simulation data]** Simulated flight test during roll excitation via optimal aileron deflection. The sequence start setting the aircraft at steady state wing-level trim condition; afterwards, the optimal signal input is performed along the roll axis via δ_a . The roll angle ϕ oscillates and move far from the trim condition which causes a deviation from the flight path. At ≈ 11 [s] flight envelope protection triggers and the open-loop sequence stops, recovering the aircraft attitude via feedback controls. In dash lines the OED constraints whereas dash-dot line the flight envelope for ϕ, p and limiters from δ_a 70

3.18 Simulated optimal longitudinal response of the a priori model (left column) versus three real experiments (right column). The real experiments are in green, magenta and cyan thin solid lines whereas their average is in thick blue solid line. In grey dash line the OED constraints while dark red dash-dot line the flight envelope. 72

3.19 Simulated lateral response of the a priori model using optimal aileron deflection (left column) versus three real experiments (right column). The real experiments are in green, magenta and cyan thin solid lines whereas their average is in thick blue solid line. In grey dash line the OED constraints while dark red dash-dot line the flight envelope. 73

3.20	Simulated lateral response of the a priori model using optimal rudder deflection (left column) versus two real experiments (right column). The real experiments are in green and cyan thin solid lines whereas their average is in thick blue solid line. In grey dash line the OED constraints while dark red dash-dot line the flight envelope.	74
3.21	[Experimental data] Five real optimal longitudinal response for the steady state wing-level flight condition with $V_{T_e} = 18$ m/s (left column) and for $V_{T_e} = 25$ m/s. In grey dash line the OED constraints while dark red dash-dot line the flight envelope. . .	75
3.22	Jacobian and Hessian Sparsity of the NLP.	80
3.23	[Experimental data] Data fitting for multiple experiments along the longitudinal dynamics for $V_{T_e} = 20$ m/s: airspeed V_T . .	81
3.24	[Experimental data] Data fitting for multiple experiments along the longitudinal dynamics for $V_{T_e} = 20$ m/s: angle of attack α	82
3.25	[Experimental data] Data fitting for multiple experiments along the longitudinal dynamics for $V_{T_e} = 20$ m/s: pitch angle θ . .	83
3.26	[Experimental data] Data fitting for multiple experiments along the longitudinal dynamics for $V_{T_e} = 20$ m/s: pitch rate q . .	84
3.27	[Experimental data] Observed Phugoid period of oscillation P_O . .	87
3.28	[Experimental data] Model structure assessment via validation data set. The a priori pitch angle θ response is not shown due to its large deviation w.r.t. the obtained experimental values. . . .	88
3.29	[Experimental data] Residual distribution analysis for the validation data set with corresponding mean value μ and standard deviation σ	89
4.1	Initial trajectory generated by the Algorithm 1 with $N = 60$, $T = 44$ and trajectory = 'lemniscate'.	102
4.2	Optimal solution relative to the angle of roll ϕ and pitch θ for a rigid wing pumping mode AWES. Path constraints are shown in dash dot grey line.	104

4.3	Optimal trajectory for a rigid wing pumping mode AWES in 3D (lemniscate pattern). The blue tether corresponds to the reel-in (power consumption) phase, while the orange tether denotes the reel-out (power production) phase. The main reel-in phase arises in the left corner, though, a further reel-in phase occurs in the right corner so as to prevent the loss of airspeed of the airborne component.	105
4.4	Optimal solution relative to tether length l , tether speed v_l , airspeed V_T , angle of attack α , angle of side slip β and tether tension f_{t_λ} for a rigid wing pumping mode AWES. Path constraints are shown in dash dot grey line.	106
4.5	Optimal solution relative to the winch angular speed ω_d , torque m_λ , instantaneous mechanical power P_m with corresponding averaged value P_{AV} for a rigid wing pumping mode AWES. Under optimal conditions, the expected average power output P_{AV} is roughly 4.6 kW	107
4.6	Optimal solution relative to tether speed v_l , airspeed V_T , angle of attack α , angle of side slip β and tether tension f_{t_λ} and mechanical power P_m for low wind conditions. Path constraints are shown in dash dot grey line.	109
4.7	Optimal holding pattern in 3D for low wind conditions. The blue tether corresponds to the reel-in (power consumption) phase, while the orange tether denotes the reel-out (power production) phase.	110
4.8	Average power outputs comparison with normalized time between lemniscate and circular trajectory.	111
4.9	Optimal solution relative to tether length l , tether speed v_l , airspeed V_T , angle of attack α , angle of side slip β and tether tension f_{t_λ} for a circular flight trajectory. Path constraints are shown in dash dot grey line.	112
4.10	Optimal trajectory for a rigid wing pumping mode AWES in 3D (circular pattern). The blue tether corresponds to the reel-in (power consumption) phase, while the orange tether denotes the reel-out (power production) phase.	113
4.11	Layout of conventional wind farms [38]. l_B denotes the blade length.	114
4.12	AWE farm layout with facility density of $1.2/l_{\max}^2$ for a given wind direction proposed in [67]. l_{\max} denotes the maximum tether.	115

- 4.13 Size comparison between lemniscate and circular trajectory under equal boundary conditions. 116
- 4.14 Comparison in 3D between optimal open-loop trajectory (left) and simulated closed-loop trajectory (right) used as initial guess with average wind speed at operating altitude $w(h) \approx 10$ m/s. In the open(closed)-loop solution the reel-in phase is denoted with blue(pink) tether, whereas the orange(green) tether corresponds to the reel-out phase. The main reel-in phase arises in the right corner (picture view), though, a further reel-in phase occurs in the left corner to prevent loss of airspeed of the airborne component. 119
- 4.15 Comparison between optimal open-loop (blue) and closed-loop simulation (orange) used as initial guess. From the top it is shown in normalized time scale the tether length l , tether speed v_l , airspeed V_T , angle of attack α , angle of side slip β (dot lines) and tether tension $f_{t,\lambda}$. Path constraints are shown in dash dot grey line. In both cases a second reel-in phase occurs in order to prevent the loss of airspeed of the aircraft. The pumping cycle time is $T \approx 50$ s and $T \approx 43$ s for the optimal and initial trajectory, respectively. Finally, as far as it regards the angle of side slip β , on the one hand its value is kept close to zero (as required) along the entire optimal trajectory. On the other hand, the control system designed by Ampyx Power B.V. is capable to bound β under realistic atmospheric conditions. 120
- 4.16 Mechanical power P_m comparison between optimal open-loop trajectory and closed-loop simulation with corresponding average power output P_{AV} , with normalized time scale. The tether speed v_l and tether tension $f_{t,\lambda}$ produce a certain amount of mechanical power P_m that is subsequently converted to electrical power P_e by the generator. Under optimal conditions, the expected average mechanical power output P_{AV} is roughly 4.6 kW, whereas it is expected that the current control system implemented by Ampyx Power B.V. causes a loss of performance $\approx 10\%$ w.r.t. the optimal scenario. 121
- 4.17 Optimal average power output P_{AV} (grey dots) with corresponding interpolation (blue line) compared against an experimental data set (black dots). 122
- 4.18 Example of trajectories associated to the cases of low, medium and high wind conditions. The grey arrows denote the wind direction. 124

4.19	System performance expressed in power curve. In the y-axis, optimal average mechanical power P_{AV} (blue dot line), theoretical power produced by a wing of area A (orange line), and power harvesting factor ξ (dash-dot red line) versus average wind speed at operating altitude $w(h)$ (x-axis).	125
4.20	Wind class-1A density function with corresponding cumulative distribution function.	126
4.21	Power Production per year relative to the case study. The blue area denotes the total energy used to keep the aircraft airborne during low wind conditions, whereas the green area correspond to the total energy harvested.	127
B.1	1-D look-up tables of C_X derivatives versus α with their corresponding polynomial interpolation.	137
B.2	1-D look-up tables of C_Y derivatives versus α with their corresponding polynomial interpolation.	138
B.3	1-D look-up tables of C_Z derivatives versus α with their corresponding polynomial interpolation.	139
B.4	1-D look-up tables of C_l derivatives versus α with their corresponding polynomial interpolation.	140
B.5	1-D look-up tables of C_m derivatives versus α with their corresponding polynomial interpolation.	141
B.6	1-D look-up tables of C_n derivatives versus α with their corresponding polynomial interpolation.	142

List of Tables

3.1	Aircraft modal analysis for steady wing-level flight at $V_{T_e} = 20$ m/s	46
3.2	Dimensional aerodynamic derivatives longitudinal dynamics	63
3.3	Dimensional aerodynamic derivatives lateral dynamics: aileron input	63
3.4	Dimensional aerodynamic derivatives lateral dynamics: rudder input	64
3.5	CRLB reduction in percentage relative to the longitudinal derivatives.	68
3.6	Dimensional aerodynamic longitudinal derivatives with corresponding expected estimation accuracy via 2CRLB.	76
3.7	Dimensionless aerodynamic longitudinal derivatives estimates carried out for different trimmed airspeed V_{T_e}	85
3.8	Collection of the a priori \mathbf{p}_{init} and estimated \mathbf{p}^* dimensionless aerodynamic longitudinal derivatives. \mathbf{p}_v is the set of parameters chosen for model validation.	86
3.9	Identified longitudinal modes.	86
3.10	Theil Inequality Coefficients	87
A.1	friction coefficient c_f for various terrain types [81].	133
A.2	Physical properties of the aircraft designed by Ampyx Power B.V. [3].	133
A.3	Polynomial coefficients relative to C_X , C_Y and C_Z	134
A.4	Polynomial coefficients relative to C_l , C_m and C_n	134

A.5	Physical properties of tether.	134
A.6	Sensors noise standard deviation σ_y	134
A.7	A priori longitudinal dimensional aerodynamic derivatives for the steady wing-level flight condition with $V_{T_e} = 20[\text{m/s}]$	134
A.8	A priori lateral dimensional aerodynamic derivatives for the steady wing-level flight condition with $V_{T_e} = 20[\text{m/s}]$	135
A.9	Flight envelope and OED constraints relative to the trim condition at $V_{T_e} = 20[\text{m/s}]$	135
A.10	Path constraints.	136

Chapter 1

Introduction

In a world of continuing industrialization the demand for energy grows constantly. Nowadays, nearly the 80% of the global energy demand is covered by fossil sources, such as oil, coal and natural gas [16], which lead to severe climate changes and environmental disasters. In order to reverse this trend, numerous governments all around the globe have provided massive subsidies for the installation of renewable energy systems. However, alternative technologies (hydro-power, solar, wind, biomass, geothermal) are normally less economically viable than fossil fuel technologies due to the high investment costs, nonuniform availability and low generated power density per unit area [38]. Nevertheless, if it was possible to exploit only 20% of the global land sites with average wind speed greater than 6.9 m/s at 80 m above the ground, the entire world's energy demand could be satisfied using exclusively wind sources [12]. In this chapter we introduce new technologies that could possibly unlock the abundant wind resource available at high altitude, and simultaneously reduce the installation costs, using tethered aircraft. In particular, we focus on a specific system designed by the Dutch company Ampyx Power B.V. [3] and known as an Airborne Wind Energy (AWE) pumping system.

1.1 Introduction to AWES

Wind speed increases significantly with altitude. On a typical onshore site, available wind energy at 500 meters altitude is two to three times the available wind energy at 100 meters altitude [11]. Conventional wind turbine manufacturers are constantly increasing the size of their systems in order to reach altitudes where the wind sources are abundant. However, such scaling up procedure leads to significant increments in terms of material for both tower structure and foundations, and costs relative to transportation, installation and maintenance. Additionally, it is not possible to arbitrarily increase the size of conventional wind turbines due to physical constraints.

As an alternative, the novel AWE technology promises to efficiently capture the wind resources at higher altitudes by replacing the tips of the blades of a wind turbine with a tethered airborne airfoil, e. g., a soft kite or a rigid wing as depicted in Figure 1.1.

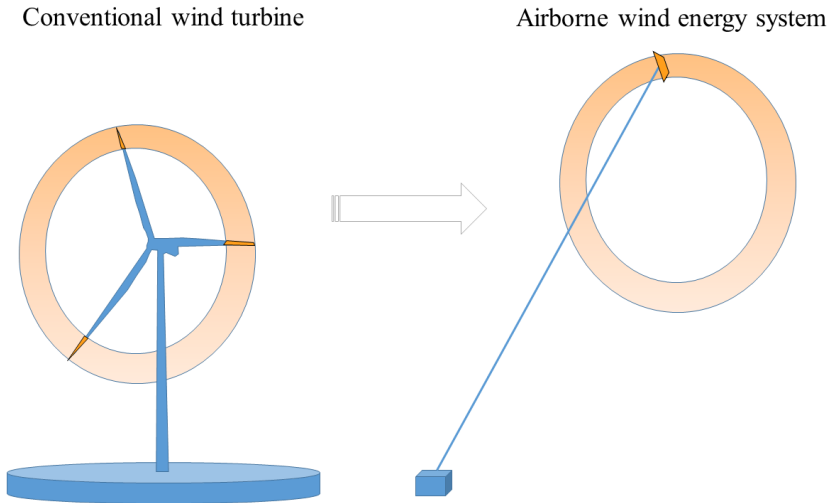


Figure 1.1: Basic principle of an AWES. An Airborne Wind Energy System (AWES) can potentially reach higher altitudes where the wind resources are abundant with less material compared to conventional wind turbines.

The key idea is based on the possibility to harvest energy from the wind by flying crosswind patterns with such tethered airfoils. As a consequence, an AWES is characterized by a high power-to-mass ratio, high capacity factors and significantly lower installation costs compared with conventional wind turbines,

up to a level that could render these systems even more economically viable than fossil fuels [34, 39].

Despite the fact that the idea of using tethered aircraft for wind power generation appeared for the first time in the late 1970s by Miles Loyd [75], it is only in the last decade that academia and industry made substantial progress in turning the idea into a practical implementation. The postponement of AWE technology is mainly due to the significant complexities in terms of control [95], modeling [47, 65], identification [73, 69], materials [40], mechanics and power electronics [28]. Furthermore, AWES need to fulfill a high level of reliability while simultaneously operating close to optimality. Such requirements have brought many developers to the use of rigid wing autonomous aircraft as airborne component [3, 2, 8, 5, 4].

A wide variety of concepts in the field of AWE can be found in the literature [34], although according to [75] two main branches can be distinguished. *Drag mode* AWES generate power using on-board turbines, transmitting power to the ground via a conductive tether. A drag mode AWES is being developed by Makani Power [2].

Lift mode or *Pumping mode* AWES produce power by performing periodical variation of tether length and tether tension. More precisely, in pumping systems a *production phase* follows a *retraction phase* periodically. During the production phase, the airfoil exerts a high tension on the tether which is anchored to a ground station composed of a winch and an electric generator. The mechanical power is fed to the electric grid after electrical conversion. Due to finite tether length, a retraction phase is required where the tether is wound up by changing the flight pattern and pulling the tether using the winch. In this phase less lifting force is generated so that significantly less energy needs to be invested in comparison to what has been gained during the *production phase*. An artist's rendering of the two main phases of a pumping mode AWES is shown in Figure 1.2.

A pumping mode AWES is being developed by the Dutch company Ampyx Power B.V. [3], but also by other companies such as KPS [6], Twingtec [8], Kitemill [5] and e-kite [4].

The presented work is entirely based on the pumping mode AWES designed by Ampyx Power B.V. [3]. The case study relies on the 2nd prototype high lift, rigid wing autonomous aircraft shown in Figure 1.3. The aircraft is a single wing, single fuselage with mass ≈ 36 kg, wing area equal to 3 m^2 and it can perform autonomous flights, as well as launching and landing procedures. Note that the prototype taken into account within this work is deployed for testing and verification purposes only, though the results obtained will be used as a guideline for the next prototype shown in Figure 1.4 and Figure 1.5.

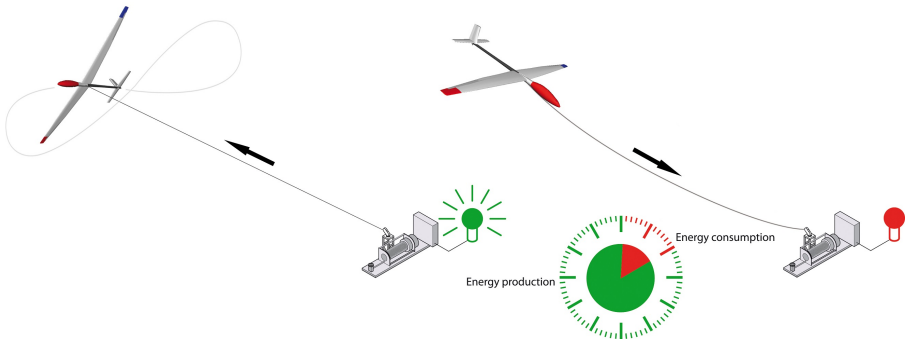


Figure 1.2: Working principles of a lift mode AWES with a production (left) and consumption (right) phase. A lift mode AWES produces power by performing periodical variation of both length and tether tension. Power generation occurs during the so called reel-out phase, where the tether tension is used to rotate a drum, driving an electric generator located on the ground. A reel-in phase is required due to finite tether length. By changing the flight pattern in such a way that less lifting force is produced, the tether can be wound up with a significant lower energy investment than what was gained in the power production phase.



Figure 1.3: The 2nd prototype high lift, rigid wing autonomous aircraft designed by Ampyx Power B.V. [3].



Figure 1.4: The 3rd prototype high lift, rigid wing autonomous aircraft designed by Ampyx Power B.V [3] (side view).

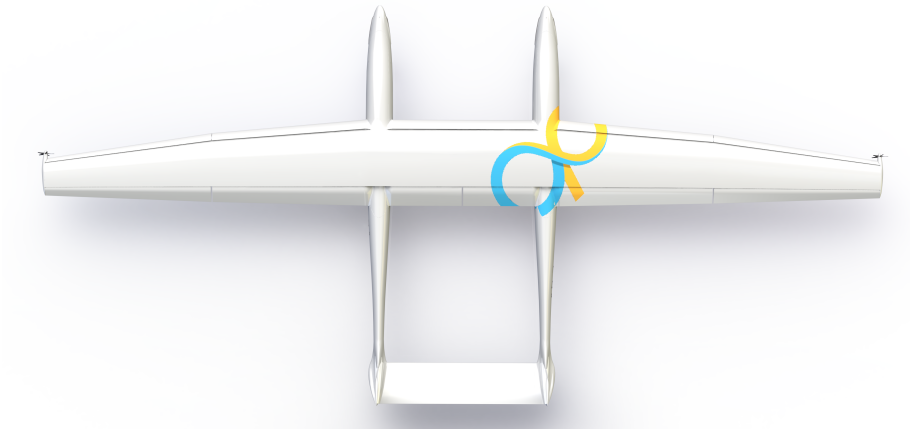


Figure 1.5: The 3rd prototype high lift, rigid wing autonomous aircraft designed by Ampyx Power B.V [3] (top view).

1.2 Contributions of outline of this thesis

The manuscript is organized in three main chapters as follows:

- **Chapter 2** introduces a mathematical formulation of a rigid wing pumping mode AWES suitable for system identification, optimization and control system design. First, an introduction of the reference frames, wind profile and aircraft characteristics are provided. Subsequently, each system component is modeled separately via Newtonian mechanics. The aircraft aerodynamic properties as well as tether dynamics are described together with a discussion of the underlying model assumptions and neglected dynamics. The nomenclature introduced is commonly used in the aerospace field.
- **Chapter 3** provides a comprehensive and self-contained guideline on aerodynamic model identification through flight tests for rigid wing, high lift, autonomous aircraft. More precisely, we focus on the flight test operations procedure, signal input design and parameter estimation algorithm. Additionally, we show how to optimize system identification flight tests by solving a time domain model-based optimum experimental design problem in order to maximize the information content of the experimental data and simultaneously enforcing safety constraints.
- **Chapter 4** presents an Optimal Control Problem (OCP) tailored to assess the system performance of a rigid wing Airborne Wind Energy (AWE) pumping system prior to manufacturing and flight tests. The proposed method is validated against experimental data. Within such analysis, it is shown that a non-optimized closed-loop flight control system can generate power to within 10% of the open-loop optimal flight trajectories. We also show that the system efficiency does not depend on the trajectory topology, though a significant change in terms of trajectory shape is observed for different wind speeds as a result of trajectory constraints. Additionally, we assess whether it is worthwhile to continue flying during low wind conditions using holding patterns compared to difficult launch and landing procedures. Finally, we demonstrate how many decision tasks related to the scaling up of an AWES can be significantly facilitated by means of the optimization methods developed within this work.

1.3 List of publications

The work presented in this book relies on the following publications. Chapter 2 contains the mathematical description of a rigid wind AWE pumping system used in Chapter 3 and Chapter 4.

Chapter 3 is based on:

- G. Licitra, A. Bürger, P. Williams, R. Ruiterkamp, and M. Diehl. *Aerodynamic Model Identification of an Autonomous Aircraft for Airborne Wind Energy*. Journal of Optimal Control Applications and Methods, Wiley (*Submitted*), Jul 2018.
- G. Licitra, A. Bürger, P. Williams, R. Ruiterkamp, and M. Diehl. *Optimal input design for autonomous aircraft*. Journal of Control Engineering Practice, Elsevier, May 2018, doi: doi.org/10.1016/j.conengprac.2018.04.013.
- G. Licitra, A. Bürger, P. Williams, R. Ruiterkamp, M. Diehl. *Optimum experimental design of a rigid wing AWE pumping system*. In IEEE 56th Conference on Decision and Control (CDC), December 2017, doi: [10.1109/CDC.2017.8264250](https://doi.org/10.1109/CDC.2017.8264250).
- G. Licitra, P. Williams, J. Gillis, S. Ghandchi, S. Sieberling, R. Ruiterkamp, and M. Diehl. *Aerodynamic parameter identification for an airborne wind energy pumping system*. IFAC 2017 World Congress, July 2017, doi: [10.1016/j.ifacol.2017.08.1038](https://doi.org/10.1016/j.ifacol.2017.08.1038).

Chapter 4 is based on:

- G. Licitra, J. Koenemann, A. Bürger, P. Williams, R. Ruiterkamp, and M. Diehl. *Performance Assessment of a Rigid Wing Airborne Wind Energy Pumping System*. Journal of Energy, Elsevier (*Submitted*), Aug 2018.
- G. Licitra, J. Koenemann, G. Horn, P. Williams, R. Ruiterkamp, and M. Diehl. *Viability assessment of a rigid wing airborne wind energy pumping system*. In IEEE 21th International Conference on Process Control (PC), Jun 2017, doi: [10.1109/PC.2017.7976256](https://doi.org/10.1109/PC.2017.7976256).
- G. Licitra, S. Sieberling, S. Engelen, P. Williams, R. Ruiterkamp, and M. Diehl. *Optimal control for minimizing power consumption during holding patterns for an airborne wind energy pumping system*. In IEEE European Control Conference (ECC), June 2016, doi [10.1109/ECC.2016.7810515](https://doi.org/10.1109/ECC.2016.7810515).

Chapter 2

Modeling of a Rigid Wing AWES

Model building is an iterative, time consuming but fundamental process for an Airborne Wind Energy System (AWES). Mathematical models based on physical laws often have to undergo considerable refinement in order to fit the data coming from, e. g., wind tunnel tests or real flight experiments. In the vast majority of cases, one aims to obtain a mathematical representation of the plant reasonably accurate for a given target and with known limitations such as parameter uncertainties and neglected dynamics. These inaccuracies may occur for instance because some parameter is not easily identifiable or because some dynamics would deliver a mathematical model that is computationally intractable. Within the AWE domain, reliable mathematical models are crucial to perform, e. g., model simulation, performance and sensitivity analysis.

This chapter introduces a mathematical formulation of a rigid wing AWE pumping system tailored to system identification and Optimal Control Problems (OCPs). The proposed model can also be used for control system design purposes.

Outline

The chapter is organized as follows. First, in Section 2.1 the wind shear is described analytically by a standard power law. Within Section 2.2, the reference frames, aircraft attitude and physical characteristics of the case study are briefly introduced, and each system component is modeled separately via Newtonian mechanics. In Section 2.3 the tether is modeled as a rigid link and

with an approximation of its aerodynamic characteristics. Section 2.4 describes the mechanical dynamics relative to the ground station. Finally, the overall mathematical model of a rigid wing pumping mode AWES is formulated as a set of Differential Algebraic Equation (DAEs) in Section 2.5. Within this Section, both the index reduction procedure and the Baumgarte stabilization are described and implemented for the case study.

2.1 Wind profile modeling

For trajectory optimization of AWES via OCPs, the wind field is normally modeled via a vertical profile of wind speed with no stochastic phenomena such as turbulence fluctuations and low level jets [54]. One of the most common wind profile models approximates the wind speed w as a function of the altitude h by a power law as follows

$$w(h) = w_{h_a} \left(\frac{h}{h_a} \right)^{c_f} \quad (2.1)$$

with h_a the anemometer height at which the wind speed w_{h_a} is measured, where c_f denotes the power law exponent that accounts for the effects of obstacles protruding from the earth's surface. High obstacles involve high values of c_f and vice-versa. Typical values of c_f are listed in Table A.1, though one may also obtain wind shear characteristics from experimental data for a specific location.

For the presented case study, a coefficient of $c_f = 0.15$ is chosen [3]. It is relevant to point out that a wind profile modeled as in (2.1) implicitly assumes *neutral conditions*, i. e., no heat flux occurs from the earth's surface. Furthermore, neutral conditions correspond also to overcast conditions with high wind speeds. For more details about the physics and theory related to the wind profiles refer to [11, 68, 81].

2.2 Tethered aircraft modeling

2.2.1 Reference frames and aircraft attitude

In order to describe any motion or position, one needs one or more reference frames. For an AWES composed by a rigid wing aircraft, it is convenient to adopt reference frame conventions commonly used in the aerospace field. Under the assumption of a flat earth, let us define a non inertial, right handed orthogonal axis system, where the x and y axis point to the northern and eastern axis, respectively, while the z -axis points downward, toward the Earth's

surface. Such frame is known as North-East-Down (NED) frame \mathbf{n} where $\mathbf{p}^{\mathbf{n}} = [p_N, p_E, p_D]^T$ denotes the NED Coordinates relative to the aircraft motion with $\mathbf{v}^{\mathbf{n}} = [v_N, v_E, v_D]^T$ the corresponding velocity vector. Likewise, let us consider a body reference frame \mathbf{b} where \mathbf{e}_x , \mathbf{e}_y , \mathbf{e}_z denote the aircraft longitudinal, transversal and vertical axis. Figure 2.1 visualizes the reference frames above introduced.

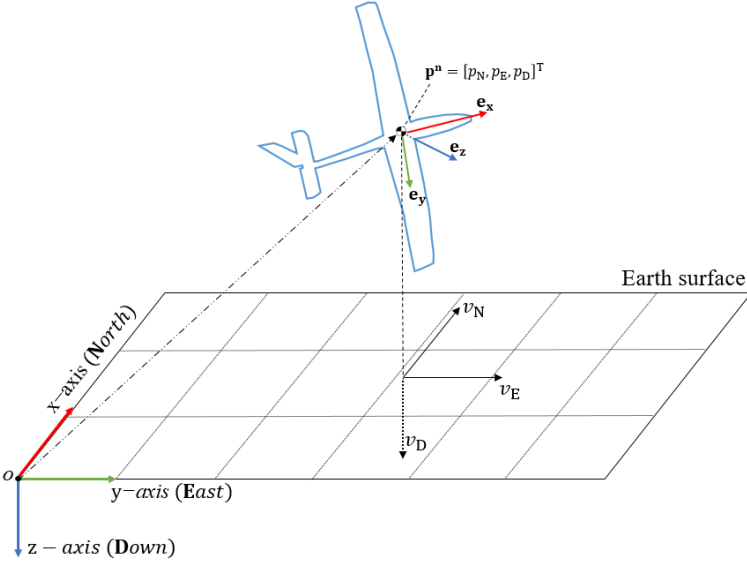


Figure 2.1: Representation of Body and NED Frame.

The need for multiple reference frames arises from the consideration that the definition of a vector might be more meaningful for one frame rather than another one. Any vector can be converted into a specific frame by means of Direction Cosine Matrices (DCMs), known also as rotation matrices. For instance, if one needs to express $\mathbf{v}^{\mathbf{n}}$ in body frame, then such transformation is given by

$$\mathbf{v}^{\mathbf{b}} = \mathbf{R}_{\mathbf{bn}} \cdot \mathbf{v}^{\mathbf{n}} \quad (2.2)$$

with $\mathbf{v}^{\mathbf{b}} = [u, v, w]^T$ the aircraft body velocity and $\mathbf{R}_{\mathbf{bn}} \in \mathbb{R}^{3 \times 3}$ the DCM from NED to body frame.

By definition, the inverse transformation of $\mathbf{R}_{\mathbf{bn}}$, i. e., $\mathbf{R}_{\mathbf{nb}}$ (from body to NED frame) is simply given by

$$\mathbf{R}_{\mathbf{nb}} = \mathbf{R}_{\mathbf{bn}}^{-1} = \mathbf{R}_{\mathbf{bn}}^T \quad (2.3)$$

where the *orthonormality condition* $\Xi_c(\mathbf{R}_{nb})$ given as

$$\Xi_c(\mathbf{R}_{nb}) = \mathbf{R}_{nb} \cdot \mathbf{R}_{nb}^\top - \mathbf{I}_3 \quad (2.4)$$

must always be equal to zero. In flight dynamics, one can define the time evolution of \mathbf{R}_{nb} as [91, 47]

$$\dot{\mathbf{R}}_{nb} = \mathbf{R}_{nb} \cdot \boldsymbol{\Omega} \quad (2.5)$$

where $\boldsymbol{\Omega}$ denotes the skew-symmetric matrix of the aircraft angular body rates $\boldsymbol{\omega}^b = [p, q, r]^\top$ and defined as

$$\boldsymbol{\Omega} = \begin{bmatrix} 0 & -r & q \\ r & 0 & -p \\ -q & p & 0 \end{bmatrix}. \quad (2.6)$$

Note that \mathbf{R}_{nb} embeds the unit vectors which describe the aircraft attitude, i. e.,

$$\mathbf{R}_{nb} = [\mathbf{e}_x \ \mathbf{e}_y \ \mathbf{e}_z]. \quad (2.7)$$

Similarly, one can define the rate of change of \mathbf{p}^n in straightforward way as

$$\dot{\mathbf{p}}^n = \mathbf{v}^n = \mathbf{R}_{nb} \cdot \mathbf{v}^b. \quad (2.8)$$

One has to point out that a DCM formulation is not always convenient, especially for visualization purposes. In this case, it is standard practice to describe the aircraft attitude by a right-handed Euler rotation sequence. More precisely, starting from the NED frame, one can compute the following three rotations:

- right handed rotation w.r.t. the z-axis, i. e., positive yaw ψ ;
- right handed rotation w.r.t. the y-axis, i. e., positive pitch θ ;
- right handed rotation w.r.t. the x-axis, i. e., positive roll ϕ .

As a result, \mathbf{R}_{nb} can also be expressed via Euler angles. In the aerospace field it is practice to use the so called *yaw-pitch-roll* sequence which results in the subsequent matrix:

$$\mathbf{R}_{nb} = \begin{bmatrix} c\theta c\psi & -c\phi s\psi + s\phi s\theta c\psi & s\phi s\psi + c\phi s\theta c\psi \\ c\theta s\psi & c\phi c\psi + s\phi s\theta s\psi & -s\phi c\psi + c\phi s\theta s\psi \\ -s\theta & s\phi c\theta & c\phi c\theta \end{bmatrix}. \quad (2.9)$$

where $c(\cdot)$ and $s(\cdot)$ are the abbreviations of $\cos(\cdot)$ and $\sin(\cdot)$, respectively. In (2.9), one can observe that from the computed DCM shown in (2.5), it is possible

to extract the Euler angles using the ij entries of \mathbf{R}_{nb} by

$$\phi = \arctan(r_{32}, r_{33}) \quad \phi \in (-\pi, \pi] \quad (2.10a)$$

$$\theta = -\arcsin(-r_{31}) \quad \theta \in (-\pi/2, \pi/2) \quad (2.10b)$$

$$\psi = \arctan(r_{21}, r_{11}) \quad \psi \in (-\pi, \pi], \quad (2.10c)$$

and as a result the aircraft attitude can be eventually bounded within an OCP framework via the Euler angles.

Finally, one can relate the Euler angle rates to the aircraft's body angular velocity as follows:

$$\begin{bmatrix} \dot{\phi} \\ \dot{\theta} \\ \dot{\psi} \end{bmatrix} = \begin{bmatrix} 1 & \sin \phi \tan \theta & \cos \phi \tan \theta \\ 0 & \cos \phi & -\sin \phi \\ 0 & \sin \phi / \cos \theta & \cos \phi / \cos \theta \end{bmatrix} \begin{bmatrix} p \\ q \\ r \end{bmatrix}. \quad (2.11)$$

These equations are known as *Euler kinematical equations* that are usually represented in compact form:

$$\dot{\Phi} = \mathbf{H}(\Phi) \cdot \omega^b. \quad (2.12)$$

Note that (2.11) has singularities at $\theta = \pm\pi/2$. Nevertheless, the Euler kinematical equations are widely used in the aerospace field for system identification purposes, stability analysis, simulations as well as control system design.

2.2.2 Airframe and physical characteristics

The presented AWES deploys as airborne component a high lift, rigid wing, single fuselage, autonomous aircraft. The airframe is equipped with aileron δ_a , elevator δ_e and rudder δ_r , entirely actuated via electric servos. The aircraft is also equipped with flaps and a propulsion system, though they are not exploited during crosswind flights.

The airframe geometry, i. e., wing span b , aerodynamic chord \bar{c} , wing area S , aspect ratio AR are collected in Table A.2 as well as the mass m and moments of inertia J_i with $i = x, y, z, xz$ relative to the body axes. Due to symmetry along the longitudinal axis, the aircraft yields a specially structured inertia matrix \mathbf{J} equal to

$$\mathbf{J} = \begin{bmatrix} J_x & 0 & -J_{xz} \\ 0 & J_y & 0 \\ -J_{xz} & 0 & J_z \end{bmatrix}. \quad (2.13)$$

Figure 2.2 graphically summarizes the airframe introduced above.

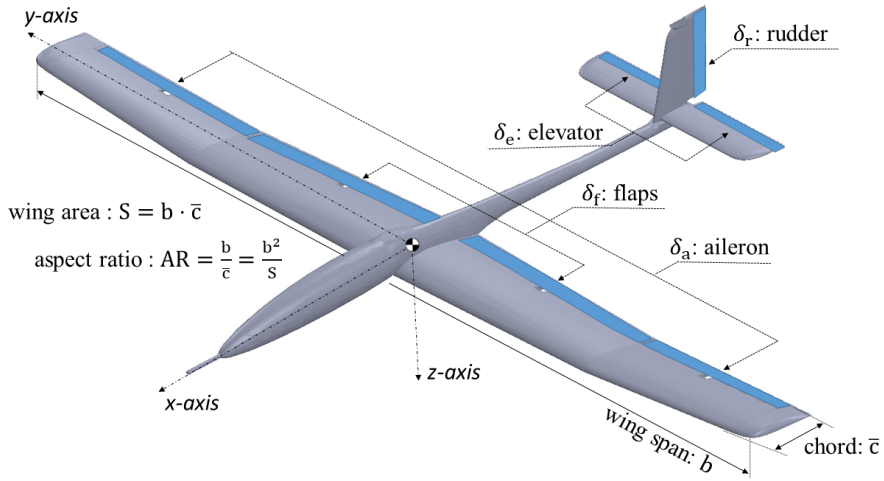


Figure 2.2: Airframe of the case study.

2.2.3 Rigid body equations

The mathematical model of a high lift rigid wing tethered aircraft can be obtained using the six degree of freedom Equations of Motion (EOM) as for modeling a conventional aircraft, i. e.,

$$\mathbf{m} \cdot \dot{\mathbf{v}}^{\mathbf{b}} = \mathbf{f}_t^{\mathbf{b}} + \mathbf{f}_a^{\mathbf{b}} + \mathbf{f}_g^{\mathbf{b}} - m(\boldsymbol{\omega}^{\mathbf{b}} \times \mathbf{v}^{\mathbf{b}}) \quad (2.14a)$$

$$\mathbf{J} \cdot \dot{\boldsymbol{\omega}}^{\mathbf{b}} = \mathbf{m}_a^{\mathbf{b}} - (\boldsymbol{\omega}^{\mathbf{b}} \times \mathbf{J} \cdot \boldsymbol{\omega}^{\mathbf{b}}) \quad (2.14b)$$

where (2.14a) is the translational acceleration and (2.14b) the angular momentum, both expressed in body frame. Assuming the airframe as a rigid body, the aircraft is subject to forces coming from the tether $\mathbf{f}_t^{\mathbf{b}} = [X_t, Y_t, Z_t]^T$, aerodynamic characteristics $\mathbf{f}_a^{\mathbf{b}} = [X, Y, Z]^T$ and gravity $\mathbf{f}_g^{\mathbf{b}}$. Normally, the tether attachment point is located close to the aircraft center of gravity, hence, one can neglect the moments caused by the tether and consider only the aerodynamic contribution $\mathbf{m}_a^{\mathbf{b}} = [l, m, n]^T$. The gravitational force defined in body frame is simply equal to

$$\mathbf{f}_g^{\mathbf{b}} = \mathbf{R}_{\mathbf{bn}} \begin{bmatrix} 0 \\ 0 \\ g_D \end{bmatrix} = mg_D \begin{bmatrix} -\sin \theta \\ \cos \theta \sin \phi \\ \cos \theta \cos \phi \end{bmatrix}. \quad (2.15)$$

with $g_D \approx 9.81 \text{ m/s}^2$. As far as it regards the aerodynamic characteristics $(\mathbf{f}_a^b, \mathbf{m}_a^b)$, they are generated by the aircraft relative motion with respect to the air mass, i. e.,

$$\mathbf{v}_r^b = \mathbf{v}^b - \mathbf{R}_{bn} \mathbf{v}_w^n = \left[v_{rx}^b, v_{ry}^b, v_{rz}^b \right]^\top \quad (2.16)$$

with \mathbf{v}_r^b the relative velocity expressed in body frame and \mathbf{v}_w^n the local wind velocity vector defined in NED frame. Throughout this work, the wind direction points North, i. e.,

$$\mathbf{v}_w^n = [w(h), 0, 0]^\top \quad (2.17)$$

with $w(h)$ shown in (2.1). Additionally, aerodynamic properties depend on the orientation of the aircraft w.r.t. the airflow. Such effect is modeled via the so called *aerodynamic states* which are given by [99]

$$V_T = \|\mathbf{v}_r^b\|_2 \quad (2.18a)$$

$$\beta = \arcsin \left(\frac{v_{ry}^b}{V_T} \right) \quad (2.18b)$$

$$\alpha = \arctan \left(\frac{v_{rz}^b}{v_{rx}^b} \right). \quad (2.18c)$$

with V_T the true airspeed, β the angle of side-slip and α the angle of attack. The nomenclature introduced above is summarized in Figure 2.3.

One can also define the translational acceleration (2.14a) in NED frame simply by

$$m \cdot \dot{\mathbf{v}}^n = \mathbf{R}_{nb} \cdot (\mathbf{f}_t^b + \mathbf{f}_a^b + \mathbf{f}_g^b) \quad (2.19)$$

Finally, for optimal control purposes it is convenient take into account the servo speed which mathematically read as

$$\dot{\delta} = \mathbf{v}_\delta \quad (2.20)$$

with $\delta = [\delta_a, \delta_e, \delta_r]^\top$ the control surface deflections and $\mathbf{v}_\delta = [v_{\delta_a}, v_{\delta_e}, v_{\delta_r}]^\top$ the corresponding actuator speed vector.

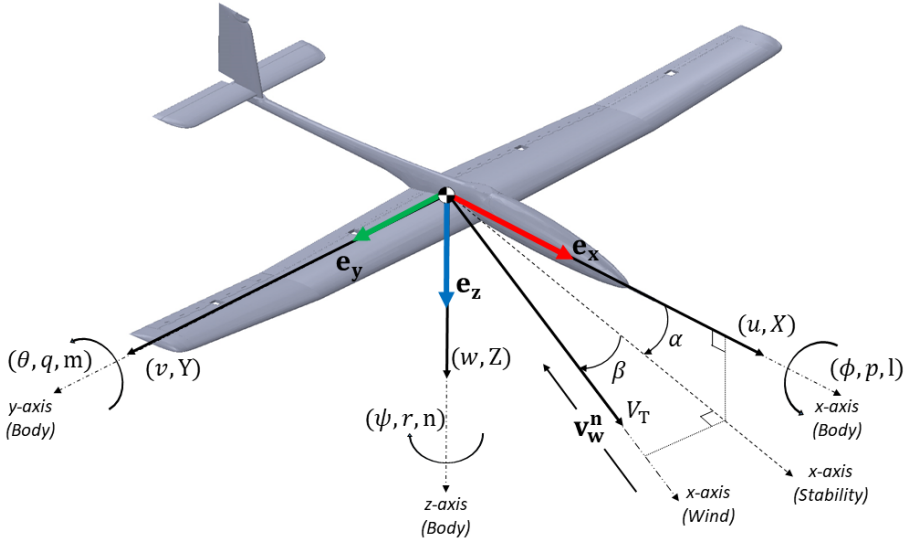


Figure 2.3: Definition of body, stability and wind axes, body angular rates ω^b and velocity \mathbf{v}^b , Euler angles (ϕ, θ, ψ) , aerodynamic states (V_T, β, α) , forces (X, Y, Z) and moments (l, m, n) of an aircraft.

2.2.4 Aerodynamic forces and moments

In the aerospace field, it is common practice to define the aerodynamic properties $(\mathbf{f}_a^b, \mathbf{m}_a^b)$ in the body frame and normalize them with respect to the dynamic pressure $\bar{q} = \frac{1}{2}\rho V_T^2$ with $\rho \approx 1.225 \text{ kg/m}^3$ the free-stream mass density, and a characteristic area of the aircraft body as follows

$$X = \bar{q}S C_X \quad : \quad \text{Axial Force} \quad (2.21a)$$

$$Y = \bar{q}S C_Y \quad : \quad \text{Side Force} \quad (2.21b)$$

$$Z = \bar{q}S C_Z \quad : \quad \text{Vertical Force} \quad (2.21c)$$

$$l = \bar{q}Sb C_l \quad : \quad \text{Rolling Moment} \quad (2.21d)$$

$$m = \bar{q}S\bar{c} C_m \quad : \quad \text{Pitching Moment} \quad (2.21e)$$

$$n = \bar{q}Sb C_n \quad : \quad \text{Yawing Moment} \quad (2.21f)$$

where C_X, C_Y, C_Z and C_l, C_m, C_n are the *non-dimensional body-axes aerodynamic force and moment coefficients*, respectively. In the most general case, these coefficients have multiple dependencies that are related to:

- flow characteristics given by the Mach number M and Reynolds number R_e [99];
- time history t of the aircraft states [91];
- aerodynamic angles (β, α) and their rates of change $(\dot{\beta}, \dot{\alpha})$ [45];
- body angular rates (p, q, r) [99];
- control surface deflections δ , which in this case are aileron δ_a , elevator δ_e and rudder δ_r [99];
- changes in center of mass position x_{CM} e.g. due to fuel consumption [26];
- *aeroelastic effects* which are modeled as a function of the altitude h , dynamic pressure \bar{q} , Mach number M and *load factor* L_f [26];
- the air-vehicle configuration $conf$, which may include asymmetric stores, landing gear (up/down position), engine/propulsion power [26], etc.

As a consequence, the *general functional form* of the non dimensional aerodynamic force and moment coefficients can be represented as

$$C_i = C_i (M, R_e, \alpha, \beta, \dot{\beta}, \dot{\alpha}, \omega^{\mathbf{b}}, \delta_j, x_{CM}, h, L_f, conf, t) \quad (2.22a)$$

$$i = X, Y, Z, l, m, n, \quad j = a, e, r, \quad t \in (-\inf, \tau]. \quad (2.22b)$$

However, for this application most of the dependencies can be neglected, since the aircraft operates in *subsonic flight* [91], no fuel consumption occurs and the air-vehicle configuration is fixed during power generation. Therefore, a reasonable trade-off between complexity and modeling accuracy is given by approximating the aerodynamic coefficients (2.22) by linear terms in their Taylor series expansion as follows

$$C_X = C_{X_\alpha} \alpha + C_{X_q} \hat{q} + C_{X_{\delta_e}} \delta_e + C_{X_0}, \quad (2.23a)$$

$$C_Y = C_{Y_\beta} \beta + C_{Y_p} \hat{p} + C_{Y_r} \hat{r} + C_{Y_{\delta_a}} \delta_a + C_{Y_{\delta_r}} \delta_r, \quad (2.23b)$$

$$C_Z = C_{Z_\alpha} \alpha + C_{Z_q} \hat{q} + C_{Z_{\delta_e}} \delta_e + C_{Z_0}, \quad (2.23c)$$

$$C_l = C_{l_\beta} \beta + C_{l_p} \hat{p} + C_{l_r} \hat{r} + C_{l_{\delta_a}} \delta_a + C_{l_{\delta_r}} \delta_r, \quad (2.23d)$$

$$C_m = C_{m_\alpha} \alpha + C_{m_q} \hat{q} + C_{m_{\delta_e}} \delta_e + C_{m_0}, \quad (2.23e)$$

$$C_n = C_{n_\beta} \beta + C_{n_p} \hat{p} + C_{n_r} \hat{r} + C_{n_{\delta_a}} \delta_a + C_{n_{\delta_r}} \delta_r, \quad (2.23f)$$

which depend on the normalized body rates $\hat{p} = \frac{bp}{2V_T}$, $\hat{q} = \frac{\bar{c}q}{2V_T}$, $\hat{r} = \frac{br}{2V_T}$, angle of attack α and side slip β , as well as the control surface deflections δ . The coefficients C_{i_j} with $i = \{X, Y, Z, l, m, n\}$ and $j = \{\alpha, \beta, p, q, r, \delta_a, \delta_e, \delta_e, 0\}$ denote the *dimensionless aerodynamic derivatives* and for this application they are implicitly functions of the angle of attack α .

Aerodynamic derivatives are usually stored as parameters in the form of 1-D look-up tables as for this application. Figures B.1, B.2, B.3, B.4, B.5, B.6 show the 1-D look-up tables of the case study with their corresponding polynomial interpolation of order up to the second degree, i. e., $p(\alpha) = c_2 \cdot \alpha^2 + c_1 \cdot \alpha + c_0$. Finally, the polynomial coefficients (c_0, c_1, c_2) are collected in Table A.3 and Table A.4.

2.2.5 The Lift-to-Drag ratio

An aircraft deployed for AWE is designed in order to maximize L^3/D^2 [75], where L is the amount of lift generated by its wing, while D denotes the aerodynamic drag. Note that for conventional airplanes it is more common to consider the Lift-to-Drag ratio L/D rather than L^3/D^2 .

In any case, for a given reel-out tether speed and in agreement with the admissible structural stress relative to the airframe, an aircraft with high L^3/D^2 can deliver higher tether tension compared to an aircraft with lower L^3/D^2 . As a consequence, the overall system performance increases as a function of L^3/D^2 .

Lift L and drag D together with the *cross-wind* force C represent the aerodynamic forces expressed in the *wind-axes* system \mathbf{w} , i. e., $\mathbf{f}_a^w = [-D, -C, -L]^T$. It is possible to retrieve \mathbf{f}_a^w from the aerodynamic body forces \mathbf{f}_a^b by means of the rotation matrix from body to wind frame \mathbf{R}_{wb} as follows

$$\mathbf{f}_a^w = \mathbf{R}_{wb} \mathbf{f}_a^b \iff \begin{bmatrix} -D \\ -C \\ -L \end{bmatrix} = \begin{bmatrix} \cos \alpha \cos \beta & \sin \beta & \sin \alpha \cos \beta \\ -\cos \alpha \sin \beta & \cos \beta & -\sin \alpha \sin \beta \\ -\sin \alpha & 0 & \cos \alpha \end{bmatrix} \begin{bmatrix} X \\ Y \\ Z \end{bmatrix}. \quad (2.24)$$

Likewise the aerodynamic properties $(\mathbf{f}_a^b, \mathbf{m}_a^b)$, the aerodynamic forces in wind axes can be normalized by the product of dynamic pressure \bar{q} times the reference area S , i. e.,

$$L = \bar{q}S C_L \quad : \quad \text{Lift Force} \quad (2.25a)$$

$$D = \bar{q}S C_D \quad : \quad \text{Drag Force} \quad (2.25b)$$

$$C = \bar{q}S C_C \quad : \quad \text{Crosswind Force} \quad (2.25c)$$

where the corresponding dimensionless derivative C_L , C_D and C_C represent the ability of an aircraft to generate lift, drag and cross-wind force, respectively.

Therefore, the lift-to-drag ratio can also be expressed via the dimensionless aerodynamic coefficients, i. e., C_L/C_D

Figure 2.4 shows the lift and drag coefficient with the corresponding L/D relative to the case study. The coefficients C_L and C_D are respectively linearly and quadratically interpolated within the range of α where the aircraft is expected to operate. The *stall phenomenon* is expected for $\alpha \geq 18$ deg, whereas the maximum efficiency can be achieved at $\alpha \approx 4$ deg. Note that, the computed L/D takes into account the aircraft aerodynamic drag, only. The tether provides an additional drag contribution, hence, a minor efficiency of the overall system is expected for significant tether drag [72].

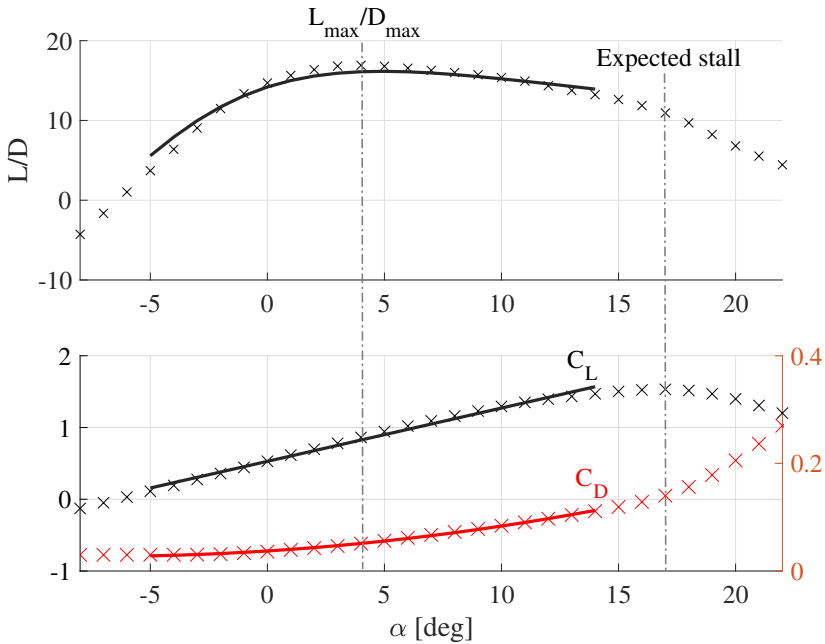


Figure 2.4: Lift and drag coefficient with the corresponding L/D for the proposed case study. The look-up values are shown in 'x', whereas their corresponding polynomial interpolation is shown in solid line.

2.2.6 Wind axes equations for tethered aircraft

For the purposes of linearizing the aircraft dynamics and studying the stability properties, it is convenient to have the velocity equation in terms of wind axes variables, i. e., airspeed V_T , angle of side slip β and angle of attack α . One way of deriving these equations is convert the translational velocity equation (2.14a) from body \mathbf{b} to wind frame \mathbf{w} . After some mathematical steps which can be found in [99] for untethered aircraft, the resulting force equation in wind axis is given by

$$\mathbf{m} \cdot \dot{\mathbf{v}}^{\mathbf{w}} = \mathbf{f}_t^{\mathbf{w}} + \mathbf{f}_a^{\mathbf{w}} + \mathbf{f}_g^{\mathbf{w}} - \mathbf{m} (\boldsymbol{\omega}^{\mathbf{w}} \times \mathbf{v}^{\mathbf{w}}) \quad (2.26)$$

where the acceleration vector and cross-product in wind frame read as

$$\dot{\mathbf{v}}^{\mathbf{w}} = [\dot{V}_T \quad \dot{\beta} V_T \quad \dot{\alpha} V_T \cos \beta]^\top \quad (2.27a)$$

$$(\boldsymbol{\omega}^{\mathbf{w}} \times \mathbf{v}^{\mathbf{w}}) = [0 \quad V_T r \quad -V_T (q \cos \beta - p \sin \beta)]^\top. \quad (2.27b)$$

Each force needs to be converted from body to wind frame by means of the rotation matrix $\mathbf{R}_{\mathbf{wb}}$, which delivers the following relationships

$$\mathbf{f}_t^{\mathbf{w}} = \mathbf{R}_{\mathbf{wb}} \mathbf{f}_t^{\mathbf{b}} = \begin{bmatrix} Y_t s \beta + X_t c \alpha c \beta + Z_t c \beta s \alpha \\ Y_t c \beta - X_t c \alpha s \beta - Z_t s \alpha s \beta \\ Z_t c \alpha - X_t s \alpha \end{bmatrix} \quad (2.28a)$$

$$\mathbf{f}_a^{\mathbf{w}} = \mathbf{R}_{\mathbf{wb}} \mathbf{f}_a^{\mathbf{b}} = \begin{bmatrix} Y s \beta + X c \alpha c \beta + Z c \beta s \alpha \\ Y c \beta - X c \alpha s \beta - Z s \alpha s \beta \\ Z c \alpha - X s \alpha \end{bmatrix} = \begin{bmatrix} -D \\ -C \\ -L \end{bmatrix} \quad (2.28b)$$

$$\mathbf{f}_g^{\mathbf{w}} = \mathbf{R}_{\mathbf{wb}} \mathbf{f}_g^{\mathbf{b}} = \mathbf{m} \begin{bmatrix} g_D (-c \alpha c \beta s \theta + s \beta s \phi s \theta + s \alpha c \beta c \phi c \theta) \\ g_D (c \alpha s \beta s \theta + c \beta s \phi c \theta - s \alpha s \beta c \phi c \theta) \\ g_D (s \alpha s \theta + c \alpha c \phi c \theta) \end{bmatrix} = \mathbf{m} \begin{bmatrix} G_{V_T} \\ G_\beta \\ G_\alpha \end{bmatrix} \quad (2.28c)$$

where the subscript t denotes the body-axis tether forces. Assembling the force contributions derived above, (2.26) read as

$$\mathbf{m} \dot{V}_T = Y_t s \beta + X_t c \alpha c \beta + Z_t c \beta s \alpha - D + \mathbf{m} G_{V_T} \quad (2.29a)$$

$$\mathbf{m} V_T \dot{\beta} = Y_t c \beta - X_t c \alpha s \beta - Z_t s \alpha s \beta - C + \mathbf{m} G_\beta - \mathbf{m} V_T r \quad (2.29b)$$

$$\mathbf{m} \dot{\alpha} V_T \cos \beta = Z_t c \alpha - X_t s \alpha - L + \mathbf{m} G_\alpha + \mathbf{m} V_T (q \cos \beta - p \sin \beta). \quad (2.29c)$$

One can observe a non-trivial coupling between the tether and aircraft dynamics, though, for crosswind tethered flights with $\beta \approx 0$ the tether force occurs mainly on the longitudinal motions. The lift L produced by the wing is converted in tether tension and for rigid airframes a non negligible part is used to compensate the gravity force (see Figure 2.5).

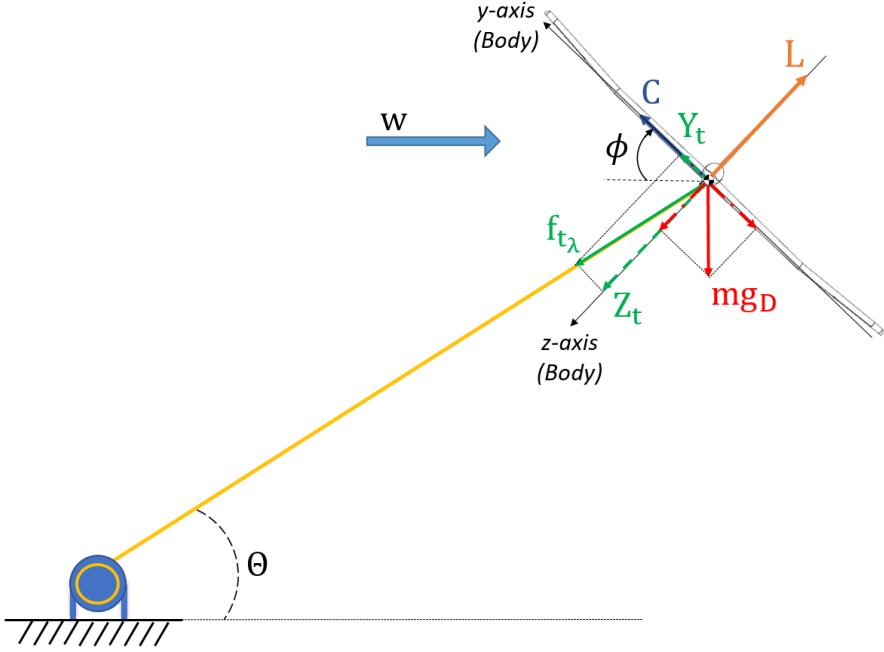


Figure 2.5: Balance of forces of a pumping mode AWES during power generation under the assumption of $\beta \approx 0$. Angles Θ and ϕ denote the elevation and roll angle, respectively, whereas $f_{t\lambda}$ corresponds to the tether tension.

2.3 Tether modeling

The main difference between a conventional aircraft and an aircraft deployed in an AWES is the presence of a tether which induces additional forces, moments (if the tether is not placed at the CG of the aircraft) and weight. An accurate tether modeling that takes into account, e.g., aeroelastic effects and tether sag, would significantly increase the overall model complexity (details in [108, 107, 105]), though, if one models the tether as a rigid link, then it is possible to obtain a mathematical formulation that is computationally attractive as shown in [47, 54, 110, 109].

Within this work, the tether force expressed in body frame \mathbf{f}_t^b is the summation of three contributions, i. e.,

$$\mathbf{f}_t^b = \mathbf{f}_{t_\lambda}^b + \mathbf{f}_{t_g}^b + \mathbf{f}_{t_a}^b \quad (2.30)$$

with $\mathbf{f}_{t_\lambda}^b$, $\mathbf{f}_{t_g}^b$ and $\mathbf{f}_{t_a}^b$ the vectors of tension, weight and aerodynamic forces relative to the tether, respectively. The tension vector $\mathbf{f}_{t_\lambda}^b$ is first obtained in NED frame and subsequently converted to body frame as follows

$$\mathbf{f}_{t_\lambda}^b = \mathbf{R}_{bn} \mathbf{f}_{t_\lambda}^n \quad (2.31)$$

where $\mathbf{f}_{t_\lambda}^n$ is introduced in Section 2.5, whereas $\mathbf{f}_{t_g}^b$ is given by

$$\mathbf{f}_{t_g}^b = \mathbf{R}_{bn} (\hat{\mathbf{e}}_z \rho_t g_D l) \quad (2.32)$$

with $l = \sqrt{p_N^2 + p_E^2 + p_D^2}$ the tether length, ρ_t its linear density, and $\hat{\mathbf{e}}_z = [0, 0, 1]^\top$. As far as it regards $\mathbf{f}_{t_a}^b$, let us first consider the tether aerodynamic forces in *wind* frame \mathbf{w} which read as

$$\mathbf{f}_{t_a}^w = \begin{bmatrix} -D_t \\ -C_t \\ -L_t \end{bmatrix} \quad (2.33)$$

with D_t , C_t and L_t the drag, crosswind and lift force relative to the tether, respectively. Among these three contributions, D_t must be taken into account while C_t is neglected and L_t is 0 since the tether does not produce lift..

In agreement with the assumption of a rigid link, let us approximate the tether velocity V_t as a linear function of both length l and aircraft speed V_T , the latter with direction constantly orthogonal to the tether, i. e.,

$$V_t \approx \frac{s}{l} V_T \quad s \in [0, l] \quad (2.34)$$

where s is a spatial coordinate along the tether. The drag force D_t for an elemental portion ds reads as

$$D_{t_s} = \frac{1}{2} \rho d_t C_{D_t} V_t^2 ds \quad (2.35)$$

with C_{D_t} and d_t the drag coefficient and tether thickness, respectively. As a consequence, the elemental moment provided by D_{t_s} w.r.t. the winch is given by

$$m_{D_{t_s}} = \left(\frac{1}{2} \rho d_t C_{D_t} V_t^2 ds \right) \cdot s. \quad (2.36)$$

Therefore, taking into account (2.34), the overall drag moment m_{D_t} can be computed

$$m_{D_t} = \int_0^l \left[\frac{1}{2} \rho d_t C_{D_t} \left(\frac{s}{l} V_T \right)^2 s \right] ds = \frac{1}{8} \rho V_T^2 C_{D_t} l^2 \quad (2.37)$$

with equivalent drag force on the aircraft [13, 55, 14]

$$D_t = \left(\frac{d_t C_{D_t}}{4} \right) \bar{q} l. \quad (2.38)$$

Equation (2.38) shows that D_t increases proportionally depending on both dynamic pressure \bar{q} and tether length l . Figure 2.6 graphically summarizes the tether drag components. Note that such approximation implicitly assumes low wind conditions, hence, the model prediction with the underlying assumption shown in (2.38) will predict an underestimation of the tether drag for high wind conditions [72, 71].

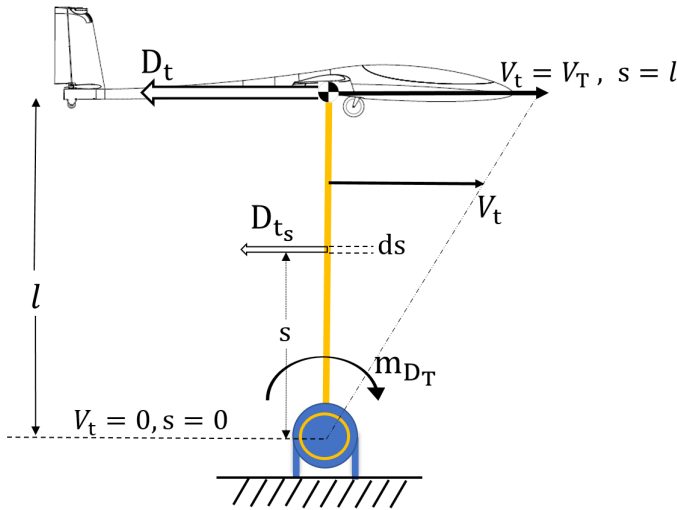


Figure 2.6: Graphical representation of the tether drag components. The tether is modeled as a rigid link and its velocity V_t is approximated as a function of both tether length l and aircraft speed V_T .

Subsequently, the tether aerodynamic force vector $\mathbf{f}_{t_a}^w$ (2.33) is converted into body frame via

$$\mathbf{f}_{t_a}^b = \mathbf{R}_{bw} \mathbf{f}_{t_a}^w \quad (2.39)$$

with $\mathbf{R}_{bw} = \mathbf{R}_{wb}^\top$, and for small side slip angles β , (2.39) can be simplified as

$$\mathbf{f}_{t_a}^b \approx -D_t \begin{bmatrix} \cos \alpha \\ 0 \\ \sin \alpha \end{bmatrix}. \quad (2.40)$$

Finally, the tether characteristics relative to the case study are collected in Table A.5.

2.4 Ground station modeling

The ground station is basically composed by a winch mechanism connected to an electric motor as shown in Figure 2.7. The mechanical components can be modeled via the energy variation \dot{E} , i.e.,

$$\dot{E} = f_{t\lambda} \omega_d r_d \quad (2.41)$$

with r_d the drum radius, and ω_d the winch rotational speed. Note that, \dot{E} is equivalent to the mechanical instantaneous power P_m .



Figure 2.7: The ground station converts the mechanical energy from tether tension into electrical power and feeds it to the grid.

As already mentioned, during the power generation (reel-out) phase the tether tension is used to rotate the drum so as to generate electricity. Subsequently, a reset (reel-in) phase is required in order to wind the tether up to its initial condition. As a consequence, the working principles of a lift mode AWES is characterized by periodical variations of the tether length that can be modeled

as

$$\dot{l} = v_l \quad (2.42a)$$

$$\dot{v}_l = a_l \quad (2.42b)$$

where $v_l = \omega_d r_d$ denotes the tether speed and a_l the corresponding acceleration.

The amount of electrical power P_e provided to the electrical grid depends on both motor efficiency $\eta(\cdot)$ and mechanical power P_m , i. e.,

$$P_e = \eta(m_\lambda, \omega_d) \cdot P_m, \quad 0 < \eta(\cdot) < 1. \quad (2.43)$$

In general, the motor efficiency $\eta(\cdot)$ is mainly a function of the motor torque $m_\lambda = f_{t_\lambda} \cdot r_d$, $\omega_d = \frac{v_l}{r_d}$ as well as the operation mode, i. e., depending if the system is in reel-in phase (motor mode) or reel-out phase (generator mode). In [100], it is shown that P_e can be reasonably modeled as a linear combination of both the motor torque and ω_d as follows

$$P_e = p_0 + p_{\omega_d} \cdot \omega_d^2 + p_{m_\lambda} \cdot m_\lambda^2 + p_{\omega_d m_\lambda} \cdot \omega_d m_\lambda \quad (2.44)$$

where p_0 , p_{ω_d} , p_{m_λ} , $p_{\omega_d m_\lambda}$ are coefficients obtained via an extensive test bench with subsequent estimation techniques. Within this work, only the mechanical power P_m is taken into account since experimental data coming from the flight tests do not include measurements of P_e .

2.5 Modeling of AWES via DAEs

In summary, a rigid wing pumping mode AWES is characterized by a high lift rigid wing autonomous aircraft connected to a winch located on the ground via a tether. As mentioned in Section 2.3, the tether is assumed as a rigid link with mass and drag. As a consequence, the corresponding tether force $\mathbf{f}_{t_\lambda}^n$ in NED frame and tether tension f_{t_λ} can be simply defined as a function of a scalar variable $\lambda \in \mathbb{R}$ as follows

$$\mathbf{f}_{t_\lambda}^n = -\lambda \mathbf{p}^n \quad (2.45a)$$

$$f_{t_\lambda} = \lambda \|\mathbf{p}^n\|_2 = \lambda l. \quad (2.45b)$$

If the ground station is located at the origin of a right-handed Cartesian coordinate system as shown in Figure 2.8, then λ must be chosen such that the aircraft dynamics evolve in the manifold described by the *consistency* condition equal to [47]

$$c(\mathbf{p}^n, l) = \mathbf{p}^{n\top} \mathbf{p}^n - l^2 = 0. \quad (2.46)$$

Therefore, an AWES can be described by a set ODEs which are subject to the consistency conditions (2.46). Additionally, if the aircraft attitude is described via the time evolution of \mathbf{R}_{nb} as in (2.5), then the orthonormality condition $\Xi_c(\mathbf{R}_{nb})$ (2.4) must be considered.

In [47, 54], it is shown that the mathematical model of a pumping mode AWES suitable for optimal control purposes takes into account a set of ODEs equal to

$$\dot{\mathbf{p}}^n = \mathbf{v}^n \quad (2.47a)$$

$$m \cdot \dot{\mathbf{v}}^n = \mathbf{R}_{nb} \cdot \left(\mathbf{f}_{t_\lambda}^b + \mathbf{f}_{t_g}^b + \mathbf{f}_{t_a}^b + \mathbf{f}_a^b + \mathbf{f}_g^b \right) \quad (2.47b)$$

$$\dot{\mathbf{R}}_{nb} = \mathbf{R}_{nb} \cdot \boldsymbol{\Omega} \quad (2.47c)$$

$$\mathbf{J} \cdot \dot{\boldsymbol{\omega}}^b = \mathbf{m}_a^b - (\boldsymbol{\omega}^b \times \mathbf{J} \cdot \boldsymbol{\omega}^b) \quad (2.47d)$$

$$\dot{\delta} = \mathbf{v}_\delta \quad (2.47e)$$

$$\dot{l} = v_l \quad (2.47f)$$

$$\dot{v}_l = a_l \quad (2.47g)$$

$$\dot{E} = f_{t_\lambda} r_d \omega_d \quad (2.47h)$$

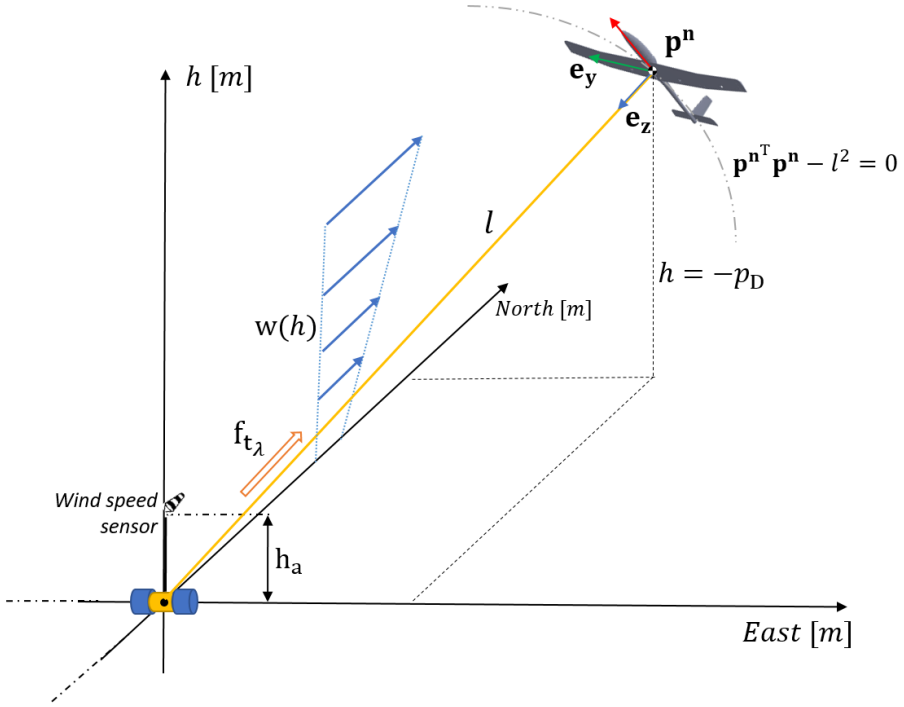


Figure 2.8: Graphical representation of a rigid wing pumping mode AWES. The ground station is located at the origin of a right-handed Cartesian coordinate system. Within this work the wind direction points North.

and a set of algebraic equations that are

$$0 = \mathbf{R}_{\text{nb}} \cdot \mathbf{R}_{\text{nb}}^\top - \mathbf{I}_3 \quad (2.48a)$$

$$0 = \mathbf{p}^{\text{n}\top} \mathbf{p}^{\text{n}} - l^2 \quad (2.48b)$$

with differential states $\mathbf{x} = [\mathbf{p}^{\text{n}}, \mathbf{v}^{\text{n}}, \mathbf{R}_{\text{nb}}, \omega^{\text{b}}, \delta, l, v_l, E]^\top \in \mathbf{R}^{24}$, control inputs, $\mathbf{u} = [v_{\delta_a}, v_{\delta_e}, v_{\delta_e}, a_l]^\top \in \mathbf{R}^4$ and algebraic variable $\mathbf{z} = \lambda \in \mathbf{R}$. The model implicitly takes into account the physical characteristics of each subsystem as well as the aerodynamic properties described in Section 2.2.4. Due to the algebraic equations, the system dynamics is therefore described by a set of Differential Algebraic Equations (DAEs).

In short, DAEs are similar to ODEs in the sense that they contain differential equations but additionally their solution $\mathbf{x}(t)$ must fulfill some algebraic

constraints. The system dynamics (2.47) and (2.48) is presented in the form of *semi-explicit* DAEs, which is formally:

$$\dot{\mathbf{x}} = \mathbf{F}(\mathbf{x}, \mathbf{z}, \mathbf{u}) \quad (2.49a)$$

$$0 = \mathbf{G}(\mathbf{x}) \quad (2.49b)$$

with $\mathbf{x} \in \mathbb{R}^{n_x}$, $\mathbf{z} \in \mathbb{R}^{n_z}$, $\mathbf{u} \in \mathbb{R}^{n_u}$, \mathbf{F} the set of differential and \mathbf{G} algebraic equations. One can also arrange (2.49) as a set of *fully-implicit* DAEs, i. e.,

$$\bar{\mathbf{F}}(\dot{\mathbf{x}}, \mathbf{x}, \mathbf{z}, \mathbf{u}) = 0. \quad (2.50)$$

In any case, one can transform (2.49) to the form of (2.50) as follows

$$\bar{\mathbf{F}}(\dot{\mathbf{x}}, \mathbf{x}, \mathbf{z}, \mathbf{u}) = 0 \Leftrightarrow \begin{bmatrix} \dot{\mathbf{x}} - \mathbf{F}(\mathbf{x}, \mathbf{z}, \mathbf{u}) \\ \mathbf{G}(\mathbf{x}) \end{bmatrix} = 0. \quad (2.51)$$

On the one hand, the obtained DAE (2.47) yields a very reasonable symbolic complexity compared to ODEs formulated via spherical coordinates as in [106]. On the other hand, they are generally more challenging in terms of formulation and numerical implementation w.r.t. standard OCPs based on ODEs.

2.5.1 Index reduction

In Section 2.5, it is shown that for this application a multi-body modeling based on Euler's equations produces a set of DAEs. According to the *implicit function theorem* [15], a DAE can be handled by classical numerical methods if the matrix

$$\mathbf{R} = \begin{bmatrix} \frac{\partial \bar{\mathbf{F}}}{\partial \dot{\mathbf{x}}} & \frac{\partial \bar{\mathbf{F}}}{\partial \mathbf{z}} \end{bmatrix} \quad (2.52)$$

is full rank, where $\bar{\mathbf{F}}$ refers to the fully-implicit formulation (2.50). Likewise, a semi-explicit DAE (2.49) can be treated with standard numerical solvers if the matrix

$$\tilde{\mathbf{R}} = \begin{bmatrix} \frac{\partial \bar{\mathbf{F}}}{\partial \dot{\mathbf{x}}} & \frac{\partial \bar{\mathbf{F}}}{\partial \mathbf{z}} \\ \mathbf{0} & \frac{\partial \mathbf{G}}{\partial \mathbf{z}} \end{bmatrix} = \begin{bmatrix} \mathbf{I} & \frac{\partial \bar{\mathbf{F}}}{\partial \mathbf{z}} \\ \mathbf{0} & \frac{\partial \mathbf{G}}{\partial \mathbf{z}} \end{bmatrix} \quad (2.53)$$

holds $\frac{\partial \mathbf{G}}{\partial \mathbf{z}}$ full rank [46], with $\tilde{\mathbf{F}}$ equal to

$$\tilde{\mathbf{F}} = \begin{bmatrix} \dot{\mathbf{x}} - \mathbf{F}(\mathbf{x}, \mathbf{z}, \mathbf{u}) \\ \mathbf{G}(\mathbf{x}) \end{bmatrix}. \quad (2.54)$$

It turns out that the mathematical model (2.49) does not result in a matrix $\tilde{\mathbf{R}}$ which has full rank due to the purely position-dependent constraint shown in (2.46) [47].

Since a DAE involves a mixture of differentiations and integrations, one may apply analytical differentiations, repeatedly if necessary, until the system yields an explicit ODE. Such procedure is known as *differential index reduction* [15], and for a semi-explicit DAE (2.49), the minimum differential index is i , such that

$$\dot{\mathbf{x}} = \mathbf{F}(\mathbf{x}, \mathbf{z}, \mathbf{u}) \quad (2.55a)$$

$$0 = \frac{d^i}{dt^i} \mathbf{G}(\mathbf{x}, \mathbf{z}, \mathbf{u}) \quad (2.55b)$$

is an explicit ODE [46]. It can be shown that a pumping mode AWES formulated as (2.47) and (2.48) delivers an index-3 DAE. However, according to [15] an OCP based on index-3 DAE is intrinsically difficult to treat from a numerical point of view. A common practice to deal with an index-3 DAE is to decrease the index via *index reduction* procedures so as to obtain an index-1 DAE where classical integration tools can be implemented within an OCP framework [46].

The first order time derivative $\dot{c}(\mathbf{x}(t))$ is equal to

$$\dot{c}(\mathbf{x}(t)) = \mathbf{p}^{\mathbf{n}\top} \dot{\mathbf{p}}^{\mathbf{n}} - l \dot{l} \quad (2.56a)$$

$$\dot{c}(\mathbf{x}(t)) = \mathbf{p}^{\mathbf{n}\top} \mathbf{v}^{\mathbf{n}} - l v_l \quad (2.56b)$$

whereas the second order time derivative $\ddot{c}(\mathbf{x}(t))$ is given by

$$\ddot{c}(\mathbf{x}(t)) = \dot{\mathbf{p}}^{\mathbf{n}\top} \dot{\mathbf{p}}^{\mathbf{n}} + \mathbf{p}^{\mathbf{n}\top} \ddot{\mathbf{p}}^{\mathbf{n}} - \dot{l}^2 - l \ddot{l} \quad (2.57a)$$

$$\ddot{c}(\mathbf{x}(t)) = \mathbf{v}^{\mathbf{n}\top} \mathbf{v}^{\mathbf{n}} + \mathbf{p}^{\mathbf{n}\top} \dot{\mathbf{v}}^{\mathbf{n}} - v_l^2 - l a_l \quad (2.57b)$$

One can make λ explicit by substituting $\dot{\mathbf{v}}^{\mathbf{n}}$ shown in (2.19) into $\ddot{c}(\mathbf{x}(t)) = 0$ which result in the following relationship:

$$0 = \mathbf{v}^{\mathbf{n}\top} \mathbf{v}^{\mathbf{n}} + \mathbf{p}^{\mathbf{n}\top} \mathbf{R}_{\mathbf{nb}} \left[-\frac{\lambda}{m} \mathbf{p}^{\mathbf{n}} + \frac{1}{m} \left(\mathbf{f}_{\mathbf{t}_g}^{\mathbf{b}} + \mathbf{f}_{\mathbf{t}_a}^{\mathbf{b}} + \mathbf{f}_{\mathbf{a}}^{\mathbf{b}} + \mathbf{f}_{\mathbf{g}}^{\mathbf{b}} \right) \right] - v_l^2 - l a_l \quad (2.58)$$

or equivalently

$$\lambda = \frac{1}{\mathbf{p}^{\mathbf{n}\top} \mathbf{R}_{\mathbf{nb}} \mathbf{p}^{\mathbf{n}}} \left[\mathbf{p}^{\mathbf{n}\top} \mathbf{R}_{\mathbf{nb}} \left(\mathbf{f}_{\mathbf{t}_g}^{\mathbf{b}} + \mathbf{f}_{\mathbf{t}_a}^{\mathbf{b}} + \mathbf{f}_{\mathbf{a}}^{\mathbf{b}} + \mathbf{f}_{\mathbf{g}}^{\mathbf{b}} \right) + m \left(\mathbf{v}^{\mathbf{n}\top} \mathbf{v}^{\mathbf{n}} - v_l^2 - l a_l \right) \right]. \quad (2.59)$$

If one considers λ as algebraic state, then the mathematical model of a pumping mode AWES would be formulated as an index-1 DAE. In contrast, if one eliminates λ , then a pure ODE would be obtained.

In summary, the consistency condition (2.46) is replaced with (2.57) in (2.48) and as a result, the index-3 DAE is converted into an index-1 DAE shown in compact form below

$$\Lambda(\mathbf{x}(t)) \begin{bmatrix} \dot{\mathbf{x}}(t) \\ \mathbf{z}(t) \end{bmatrix} - \mathbf{b}(\mathbf{x}(t), \mathbf{u}(t)) = 0 \quad (2.60)$$

where $\mathbf{x}(t)$, $\mathbf{z}(t)$, $\mathbf{u}(t)$ have already been introduced in Section 2.5, while the matrices $\Lambda(\cdot)$ and $\mathbf{b}(\cdot)$ are equal to

$$\Lambda(\mathbf{x}(t)) = \begin{bmatrix} \mathbf{I}_3 & * & * & * & * & * & * & * & * \\ * & m\mathbf{I}_3 & * & * & * & * & * & * & \mathbf{p}^n \\ * & * & \mathbf{I}_3 & * & * & * & * & * & * \\ * & * & * & \mathbf{J} & * & * & * & * & * \\ * & * & * & * & \mathbf{I}_3 & * & * & * & * \\ * & * & * & * & * & 1 & * & * & * \\ * & * & * & * & * & * & 1 & * & * \\ * & * & * & * & * & * & * & 1 & -l r_d \omega_d \\ * & \mathbf{p}^{n\top} & * & * & * & * & * & * & * \end{bmatrix} \quad (2.61)$$

$$\mathbf{b}(\mathbf{x}(t), \mathbf{u}(t)) = \begin{bmatrix} \mathbf{R}_{nb} \cdot \mathbf{v}^b \\ \mathbf{R}_{nb} \cdot (\mathbf{f}_{t_\lambda}^b + \mathbf{f}_{t_g}^b + \mathbf{f}_{t_a}^b + \mathbf{f}_a^b + \mathbf{f}_g^b) \\ \mathbf{R}_{nb} \cdot \boldsymbol{\Omega} \\ m_a^b - (\boldsymbol{\omega}^b \times \mathbf{J} \cdot \boldsymbol{\omega}^b) \\ \mathbf{v}_\delta \\ v_l \\ a_l \\ * \\ -\mathbf{v}^{n\top} \mathbf{v}^n + v_l^2 + l a_l \end{bmatrix} \quad (2.62)$$

where $*$ denotes zeros of suitable dimensions. Finally, in order to obtain a meaningful solution, (2.60) must fulfill the consistency conditions (2.46) (2.56), and (2.4) for $t_0 = 0$ [47, 46, 15],

2.5.2 Baumgarte stabilization

In order to carry out flight trajectories for a pumping mode AWES using an optimal control approach, an index-1 DAE formulation was derived in Section 4.1.3. As a consequence, the consistency conditions (2.46) (2.56), and (2.4) need to be fulfilled for $t_0 = 0$ to ensure that the system dynamics evolve within the prescribed manifold [15]. In principle, this holds true if numerical inaccuracies introduced by integration methods would not occur [97]. In practice,

the system dynamics are prone to drift away from the manifold, especially for long simulation times [47]. One way to address such numerical drifts is by the *Baumgarte stabilization* [17], and for an index-1 DAE, the key idea is to replace $\ddot{c}(x(t))$ shown in (2.57) with the following equation

$$0 = \ddot{c}(x(t)) + \kappa_1 \dot{c}(x(t)) + \kappa_2 c(x(t)) \quad (2.63)$$

with $\kappa_1, \kappa_2 > 0$, such that the numerical drift is bounded. In this case, one needs to replace (2.57) in (2.60) with

$$0 = \left(\mathbf{v}^{\mathbf{n}\top} \mathbf{v}^{\mathbf{n}} + \mathbf{p}^{\mathbf{n}\top} \dot{\mathbf{v}}^{\mathbf{n}} - v_l^2 - l a_l \right) + k \left(\mathbf{p}^{\mathbf{n}\top} \mathbf{v}^{\mathbf{n}} - l v_l \right) + k \left(\mathbf{p}^{\mathbf{n}\top} \mathbf{p}^{\mathbf{n}} - l^2 \right). \quad (2.64)$$

One has to point out that numerical drift issues are not DAE-specific, but also arise in other situations, e. g., when the system dynamics are represented by non-minimal coordinates, in other words, when the degrees of freedom of the plant are less than the number of differential states used to describe its dynamics. It turns out that the mathematical model (2.47) is described by non-minimal coordinates since the time evolution of the DCM (2.5) describes the aircraft attitude (roll, pitch and yaw) by nine rather than three differential states. Therefore, in order to bound the numerical drift relative to the orthonormality condition (2.4) one needs to modify the time evolution of the DCM (2.5) with

$$\dot{\mathbf{R}}_{\mathbf{nb}} = \mathbf{R}_{\mathbf{nb}} \cdot (\boldsymbol{\Omega} + \boldsymbol{\Pi}), \quad \boldsymbol{\Pi} = \frac{\kappa_3}{2} \left[(\mathbf{R}_{\mathbf{bn}} \mathbf{R}_{\mathbf{nb}})^{-1} - \mathbf{I}_3 \right] \quad (2.65)$$

such that the orthonormality condition is stabilized for $\kappa_3 > 0$ [49].

Chapter 3

Aerodynamic Model Identification

An important task for the development of an AWES is the mathematical modeling of the aircraft dynamics. Such models of aircraft dynamics regularly contain quantities called *aerodynamic derivatives* (or simply *derivatives*), which in general depend on the flight condition and the aircraft geometry.

In the aerospace field, it is the current practice to retrieve the aerodynamic derivatives by a combination of wind tunnel testing, CFD [9] analysis, and empirical methods such as DATCOM [53]. For standard aircraft configurations, such methods for obtaining aerodynamic characteristics are generally in agreement with those obtained via flight tests. However, empirical methods, which can provide the quickest results, tend to be less accurate and more difficult to apply to unconventional designs. CFD is much more accurate, but requires a fine mesh to capture the flow dynamics accurately, and as a consequence it involves significant computational resources to obtain a complete aerodynamic database. Wind tunnel experiments generally provide the most accurate results with a suitably sized model that matches the Reynold's numbers of the real system. However, for unconventional systems such an approach can also be expensive. In any case, an intensive flight test campaign must be ultimately set in order to gain additional insight about the aerodynamic properties and to validate parameters on the full scale system.

A successful flight test campaign depends on many factors, such as selection of instrumentation, signal conditioning, flight test operations procedure, parameter estimation algorithm and signal input design. This chapter provides a comprehensive description of the flight test campaigns that aim towards the

identification of aerodynamic models for rigid wing, high lift, autonomous aircraft deployed for AWE. In particular, we focus on the flight test procedures, signal input design, and how to formulate and efficiently solve a parameter estimation problem. Furthermore, we show how to design optimized experiments which implicitly take into account the flight envelope constraints and help to reduce the number of expensive system identification flight tests required to achieve a certain degree of estimation accuracy.

Outline

The chapter is organized as follows. Section 3.1 describes the flight test operations procedure and safety requirements, underlying theoretical and practical aspects. In Section 3.2, a suitable model structure is selected for both signal input design and estimation of aerodynamic properties augmented with model assumptions as well as neglected dynamics. Section 3.3 focuses on the design of an input signal widely used in the aerospace field. In Section 3.4 it is shown how to obtain optimized maneuvers by solving a time domain model-based Optimum Experimental Design (OED) problem which aims to obtain more accurate parameter estimates, and simultaneously enforcing safety constraints. The optimized experiments are analyzed and compared w.r.t. conventional maneuvers using the Cramer-Rao Lower Bound (CRLB). Subsequently, real flight test campaigns are carried out using both conventional and optimized maneuvers, and for multiple flight conditions. In Section 3.5, estimation of the aerodynamic characteristics are carried out via an efficient multiple experiment Model-Based Parameter Estimation (MBPE) algorithm suitable for dynamic systems and based on *direct methods*. The data fitting is applied throughout the aircraft longitudinal dynamics using a non-linear model structure. Both estimates and model structure are assessed against a validation data set. Finally, the prediction capability of the identified model is assessed via the Theil Inequality Coefficient (TIC), a standard criterion widely used within the aerospace field.

3.1 Experimental design set-up

This section focuses on the flight test procedure for autonomous aircraft. Further, safety, practical and theoretical aspects are discussed for the case study.

3.1.1 Flight test procedure and the rationale behind

In Section 2.2.3, it has been shown that high lift rigid wing tethered aircraft relies ultimately on the rigid body equations of motion, known also as *Euler's equations* and they are equal to

$$\mathbf{m} \cdot \dot{\mathbf{v}}^{\mathbf{b}} = \mathbf{f}_{\mathbf{t}}^{\mathbf{b}} + \mathbf{f}_{\mathbf{a}}^{\mathbf{b}} + \mathbf{f}_{\mathbf{g}}^{\mathbf{b}} - m(\boldsymbol{\omega}^{\mathbf{b}} \times \mathbf{v}^{\mathbf{b}}) \quad (3.1a)$$

$$\mathbf{J} \cdot \dot{\boldsymbol{\omega}}^{\mathbf{b}} = \mathbf{m}_{\mathbf{a}}^{\mathbf{b}} - (\boldsymbol{\omega}^{\mathbf{b}} \times \mathbf{J} \cdot \boldsymbol{\omega}^{\mathbf{b}}) \quad (3.1b)$$

with external forces and moments coming from the **tether**, **aerodynamic** characteristics and **gravity**. In order to identify the aerodynamic forces $\mathbf{f}_{\mathbf{a}}^{\mathbf{b}}$ and moments $\mathbf{m}_{\mathbf{a}}^{\mathbf{b}}$ from measurements, one has to either discard or have good models of the other contributions, or ensure that their influence is very small.

On the one hand, the gravity component expressed in body frame $\mathbf{f}_{\mathbf{g}}^{\mathbf{b}}$ can be easily computed using the Euler angles multiplied by the gravity acceleration (see Equation (2.15)). On the other hand, it is rather difficult to obtain an accurate measurement of the tether forces $\mathbf{f}_{\mathbf{t}}^{\mathbf{b}}$. As a consequence, the incorporation of the tether contribution during the system identification flight test would significantly deteriorate the quality of the aircraft aerodynamic model that need to be identified. Even though it would be possible to measure the tether effect with a high degree of accuracy, from a system identification point of view it would act as a disturbance source due to possible vibrations that might occur during the excitation of the system dynamics. For these reasons, for the identification of aerodynamic models via flight tests, it is best to perform untethered flight to both simplify the overall system modeling and to avoid disturbances caused by eventual tether vibrations.

Normally, the flight test procedure is divided into three parts: take-off, execution of the experiments and landing. The take-off and landing phase are generally performed manually by the pilot via remote control. After the manual stabilization of the aircraft dynamics, the autonomous mode is enabled and the vehicle flies into a predefined race track pattern by means of a propulsion system. From a safety point of view, flight tests for autonomous aircraft are limited to *line-of-sight* range in order to both avoid communication dropout and to guarantee that the pilot can regain manual control of the aircraft at any time [35].

The case study is equipped with a propulsion system (battery powered) characterized by two electric motors that drive two propellers mounted on top of the fuselage, allowing ≈ 15 min of flying time on a single charge. Also in this case, it is rather difficult to achieve high accuracy on propeller dynamics. Furthermore, the rotation of the blades introduces additional noise for each angular rate and acceleration channel. As a consequence, propellers are switched off whenever an excitation signal occurs in order to decouple the uncertainty in thrust effects on the aerodynamic parameter estimation.

Typically, experiments are repeated on each axis to both obtain a rich data set and reduce the effect of sensor biases as well as colored noise (atmospheric turbulence) on the estimation results [73]. To prevent biases due to correlation between the measurement noise and the inputs, it is best to perform open-loop experiments [98] which are also beneficial for systems equipped with sensors that are susceptible to high levels of measurement noise [35]. Additionally, system identification flight tests are performed at *steady wing-level flight* condition [35].

An aircraft is formally in steady wing-level flight condition when its body angular rates (p, q, r) and roll angle ϕ are equal to zero and it flies with constant airspeed V_{T_e} [99]. Fulfillment of this steady condition allows decoupling of the aircraft motion in *longitudinal* and *lateral* dynamics, hence one can focus only on a subset of the entire aircraft dynamics which is mainly excited from a given maneuver. For instance, if a signal excitation is performed along the longitudinal axis via elevator deflection (with propellers switched-off), the remaining control surfaces (aileron and rudder deflection) are used to stabilize the lateral dynamics throughout the entire experiment. Consequently, the parameter estimation is performed only on the excited dynamics. Note that for the presented case study the cross-product of inertia J_{xz} is only $\approx 2\%$ w.r.t. the smallest moment of inertia, i. e., J_x , hence negligible cross-coupling effects are expected.

Figure 3.1 depicts the flight test procedure described above and adopted within this work. One can observe how after the excitation of the longitudinal dynamics, the propellers are switched on and the aircraft operates fully in closed-loop to recover a steady regime. Note that, for this specific aircraft the propellers provide non-negligible pitch moment contribution since they are located on top of the fuselage.

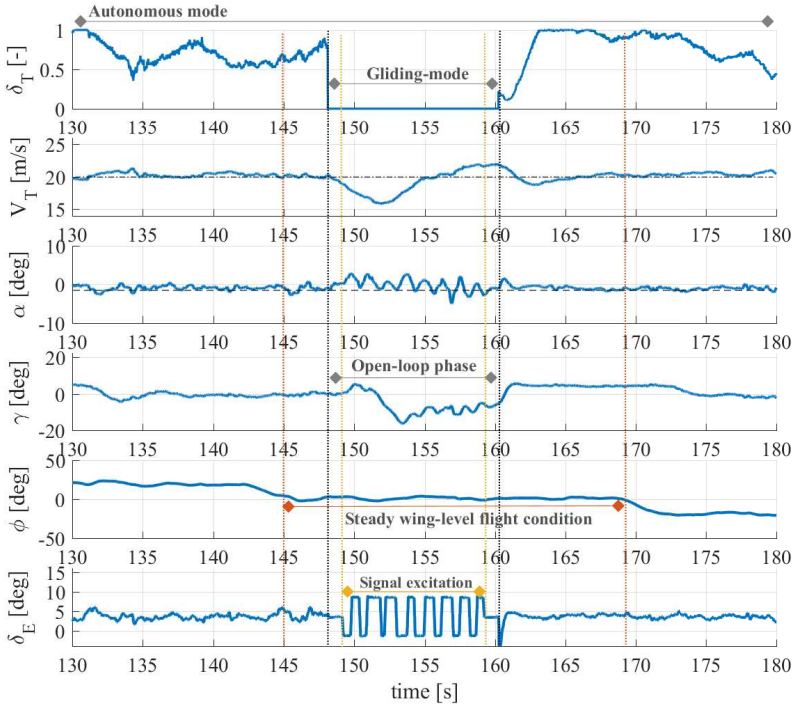


Figure 3.1: **[Experimental data]** Example of a flight test procedure for a high lift, autonomous aircraft. After a coordinated turn [99], the aircraft performs a straight flight (roll angle $\phi \approx 0$ deg) with constant airspeed $V_{T_e} \approx 20$ m/s and corresponding constant angle of attack $\alpha_e \approx -2$ deg held by elevator deflection angle $\delta_{e_e} \approx 3.5$ deg. The flight path angle γ is approximately zero prior to the gliding mode. Throughout the excitation of the longitudinal motion performed in gliding mode, the aircraft slightly descends as also shown by γ , though, the angle of attack response remain within a neighborhood of α_e . The data set is collected during the open-loop phase and despite a significant excitation of the longitudinal dynamics, the lateral motion is barely perturbed thanks to both the steady wing level flight condition and the motion stabilization via aileron δ_a and rudder δ_r deflection.

3.1.2 Flight envelope limit detection

Historically, aerodynamic model identifications have been performed using a pilot to provide input sequences. A system identification flight test carried out in autonomous mode implies no action of the pilot during the experiment unless system failures are detected. As a consequence, reliable simulators play an important role for the design of maneuvers and minimization of flight envelope violation. Nonetheless, it may happen that during the real flight test the aircraft violates the flight envelope e.g. due to significant inaccuracies of the a priori models or unexpected gust that occurs within the open loop-phase. For this reason, *flight envelope limit detection* algorithms should be programmed in the Flight Control Computer (FCC) in order to avoid damages or complete destruction of the vehicle. Figure 3.2 shows an example of how the flight envelope limit detection reacts right after the pitch angle θ violates its safety limit.

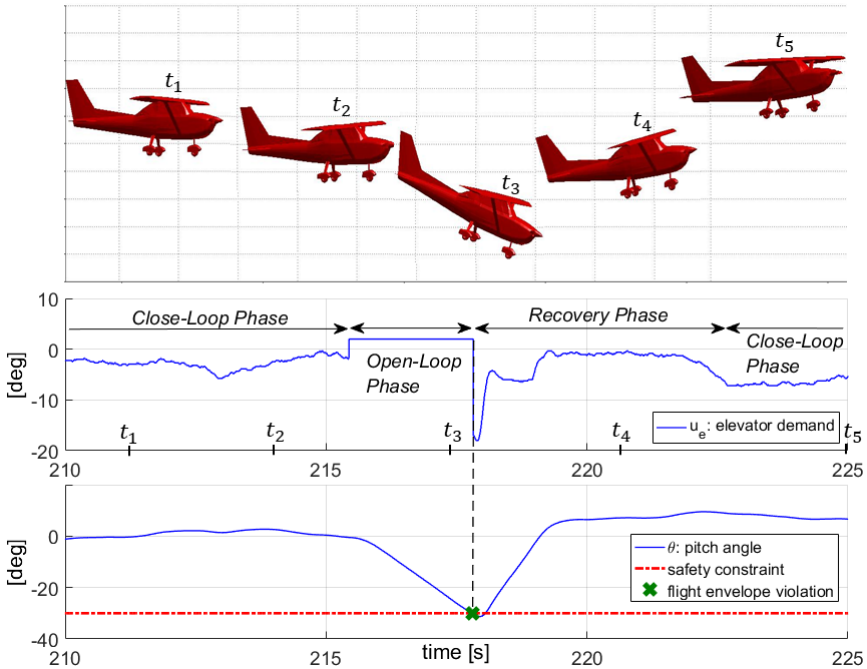


Figure 3.2: [Simulation data] Example of flight envelope limit detection. A badly designed maneuver is performed along the longitudinal axis via elevator deflection. The detection of flight envelope violation involves the stop of the open-loop phase, with recovery of the previous trim condition.

3.1.3 Flight test instrumentation

The proposed aircraft is instrumented with an Inertial Measurement Unit (IMU) which provides measurements of body angular rates and translational accelerations. The aerodynamic states are estimated by means of a *five hole pitot tube*, which is mounted at the nose of the fuselage. All measurements are suitably low-pass filtered using zero-lag filtering in order to focus only on the rigid-body modes. The sensor noise of each component is expressed in terms of its standard deviation σ_y and they are shown in Table A.6.

The actuator commands are delivered by an on-board flight computer at 100 Hz (see Figure 3.3), and data are recorded at the same rate. The control surface inputs are measured via feedback sensors on the aircraft, which allows the estimation to proceed without requiring knowledge of the actuator dynamics.

Finally, the control surface deflection measurements have no discernible noise, though quantization errors equal to 0.25 deg are present and compensated.



Figure 3.3: Five hole pitot tube and FCC mounted at the nose and inside the fuselage, respectively.

3.2 Grey-box model selection

In this section, a comprehensive dynamical representation of the aircraft for aerodynamic model identification is presented, underlying model assumptions and neglected dynamics. Further, a brief overview about the a priori aerodynamic model is provided.

3.2.1 Model structure selection

The choice of an appropriate model structure is crucial for any successful identification application. Within this work, the model structure is a non-linear and physically parametrized ODE in state-space representation, though, for the design of maneuvers the corresponding linear representation is taken into account. The advantage of using a non-linear representation is that such model should be valid for large range of flight conditions. Moreover, system identification flight tests are less constrained w.r.t. the amplitudes of angle of attack α and airspeed V_T excursions [90].

For system identification purposes, the mathematical model embeds the velocity equation in wind-axes (2.29), the Euler kinematic equations (2.11) and the angular momentum (2.14b). Expanding the equations and discarding the tether dynamics, the proposed model structure read as [99]

$$\dot{V}_T = \frac{Y \sin \beta + X \cos \alpha \cos \beta + Z \cos \beta \sin \alpha}{m} + G_{V_T}, \quad (3.2a)$$

$$\dot{\beta} = \frac{Y \cos \beta - X \cos \alpha \sin \beta - Z \sin \alpha \sin \beta}{m V_T} + \frac{G_\beta}{V_T} - r \cos \alpha + p \sin \alpha, \quad (3.2b)$$

$$\dot{\alpha} = \frac{Z \cos \alpha - X \sin \alpha}{m V_T \cos \beta} + \frac{G_\alpha}{V_T \cos \beta} + \frac{q \cos \beta - (p \cos \alpha + r \sin \alpha) \sin \beta}{\cos \beta}, \quad (3.2c)$$

$$\dot{\phi} = p + r \cos \phi \tan \theta + q \sin \phi \tan \theta, \quad (3.2d)$$

$$\dot{\theta} = q \cos \phi - r \sin \phi, \quad (3.2e)$$

$$\dot{\psi} = \frac{q \sin \phi + r \cos \phi}{\cos \theta}, \quad (3.2f)$$

$$\dot{p} = \frac{J_{xz}}{J_x} \dot{r} - qr \frac{(J_z - J_y)}{J_x} + qp \frac{J_{xz}}{J_x} + \frac{L}{J_x}, \quad (3.2g)$$

$$\dot{q} = -pr \frac{J_x - J_z}{J_y} - (p^2 - r^2) \frac{J_{xz}}{J_y} + \frac{M}{J_y}, \quad (3.2h)$$

$$\dot{r} = \frac{J_{xz}}{J_z} \dot{p} - pq \frac{J_y - J_x}{J_z} - qr \frac{J_{xz}}{J_z} + \frac{N}{J_z}, \quad (3.2i)$$

where G_{V_T} , G_β , G_α are the gravity components expressed in wind frame shown in (2.28c). The aerodynamic body forces (X, Y, Z) and moments (L, M, N) shown in (2.21) are characterized by a linear structure as in (2.23) and they embed the dimensionless aerodynamic derivatives C_{i_j} that need to be identified within the flight test campaign.

Ultimately, the aircraft dynamical representation augmented with the sensors modeling can be expressed in compact form as follows

$$\dot{\mathbf{x}}(t) = \mathbf{f}(\mathbf{x}(t), \mathbf{u}(t), \mathbf{p}), \quad \mathbf{x}(0) = \mathbf{x}_0, \quad t \in [0, T], \quad (3.3a)$$

$$\mathbf{y}(t) = \mathbf{h}(\mathbf{x}(t), \mathbf{u}(t), \mathbf{p}), \quad (3.3b)$$

$$\mathbf{y}_m(i) = \mathbf{y}(i) + \epsilon(i), \quad i = 1, \dots, N \quad (3.3c)$$

with differential states $\mathbf{x} \in \mathbb{R}^{n_x}$, noise-free control inputs $\mathbf{u} \in \mathbb{R}^{n_u}$, and parameters $\mathbf{p} \in \mathbb{R}^{n_p}$ equal to

$$\mathbf{x} = [V_T \quad \beta \quad \alpha \quad \phi \quad \theta \quad \psi \quad p \quad q \quad r]^\top \quad (3.4a)$$

$$\mathbf{u} = [\delta_a \quad \delta_e \quad \delta_r]^\top \quad (3.4b)$$

$$\mathbf{p} = \begin{bmatrix} C_{X_\alpha} & C_{X_q} & C_{X_{\delta_e}} & C_{X_0} & C_{Y_\beta} & C_{Y_p} & C_{Y_r} & C_{Y_{\delta_a}} & C_{Y_{\delta_r}} \\ C_{Z_\alpha} & C_{Z_q} & C_{Z_{\delta_e}} & C_{Z_0} & C_{l_\beta} & C_{l_p} & C_{l_r} & C_{l_{\delta_a}} & C_{l_{\delta_r}} \\ C_{m_\alpha} & C_{m_q} & C_{m_{\delta_e}} & C_{m_0} & C_{n_\beta} & C_{n_p} & C_{n_r} & C_{n_{\delta_a}} & C_{n_{\delta_r}} \end{bmatrix}^\top \quad (3.4c)$$

with $n_x = 9$, $n_u = 3$ and $n_p = \mathbb{R}^{27}$. The instrumentation introduced in Section 3.1.3 together with the mathematical formulation greatly simplify the output function \mathbf{h} which in this case is equal to $\mathbf{y}(t) = \mathbf{x}(t)$ where $\mathbf{y} \in \mathbb{R}^{n_y}$ denotes formally the output states. Furthermore, the output \mathbf{y}_m is sampled in N measurements along a time horizon T and it is polluted by additive, zero-mean Gaussian noise $\epsilon \approx \eta(0, \Sigma_y)$ with $\Sigma_y \in \mathbb{R}^{n_y \times n_y}$ the measurements noise covariance matrix.

3.2.2 Model assumptions and neglected dynamics

In flight dynamics, different methods of aerodynamic derivatives modeling exist. A highly accurate approach can be provided by the *indicial response method* in conjunction with the *superposition principle* [37, 102] which is formally equal to

$$\mathbf{c} = \int_0^t \mathbf{A}_h(t - \tau) \dot{\mathbf{h}} \, d\tau \quad (3.5)$$

where $\mathbf{c} = [C_X, C_Y, C_Z, C_l, C_m, C_n]^T$ is the combined vector of the total aerodynamic body force and moment coefficients, whereas \mathbf{A}_h is a matrix of indicial response functions for stepwise variation of the parameters $\mathbf{h} = [\alpha, \beta, p, q, r, \delta_a, \delta_e, \delta_r]^T$. Despite the unquestionable efficiency of this formulation, it is rather difficult to combine such functional representation with the equations of an aircraft motion which are expressed as a set of ODEs. Such an approach

can also be extended to a nonlinear case corresponding to the separated flow conditions [102], though, the overall description becomes significantly complicated.

For this reason, within the aerospace field it is common practice to approximate the aerodynamic characteristics by linear terms in their Taylor series expansion. On the one hand, such approximation yield sufficient accuracy for attached flows [37]. On the other hand, this aerodynamic modeling cannot be used in the region of α where separated flow occurs [45]. Within this work, since the aircraft dynamics and its aerodynamic characteristics are described by (3.2), (2.28c), (2.21) and (2.23), one has to implicitly account for the model mismatches summarized below:

- The aerodynamic model (2.21) and (2.23) neglects the influence of parameter variation through time [91]. One can account for such a model mismatch either by introducing a first-order differential equation involving the angle of attack rate $\dot{\alpha}$ [45], or by designing flight trajectories customized for energy production that allow the aircraft to perform mild maneuvers [72, 71].
- The mathematical model (3.2) relies on Euler's equations which describe the motion of rigid bodies only, hence flexible modes are implicitly neglected. However, a rigid wing aircraft for AWE is usually characterized by a high-strength wing with relatively high stiffness, as also expected for the next prototype shown in Figure 1.4 and Figure 1.5. Eventual structural-coupling issues caused by flexible modes must be addressed during the control architecture design [99].
- The aerodynamic derivatives in (2.23) are implicitly a function of α . Nevertheless, system identification performed via flight tests are typically valid only for small neighborhood of α with respect to its trim value α_e . Because aircraft deployed for AWES are intended to fly over a wide range of flight conditions, flight test maneuvers and parameter identification need to be performed at multiple trimmed airspeed V_{T_e} .
- Estimates of aerodynamic derivatives are computed assuming that the aircraft inertias are known a priori. However, fully accurate inertial estimates are difficult to obtain. Inertia estimates can be computed from Computer Aided Design (CAD) models or swing tests with varying degrees of accuracy [30, 78]. Errors in $J_{\{x,y,z,xz\}}$ leads to errors in the absolute estimates of the aerodynamic coefficients. Nevertheless, this will not undermine the predictive capability of the derived model, as long as the estimated derivatives are kept consistent with the assumed value of $J_{\{x,y,z,xz\}}$ used to estimate them [73].

In order further mitigate the model inaccuracies above mentioned, it is current practice to design a complex hierarchical control system with high margin of robustness and to fly patterns with specific boundary conditions (for further details refer to [95]).

3.2.3 A priori aerodynamic model

Experimental design aimed towards the identification of aerodynamic characteristics requires an *a priori model* with reasonable accuracy in order to obtain sufficient information content on the measurements data without violate the predefined flight envelope. A priori models are also useful to provide an insight into the general characteristics of the aircraft behavior. Various methods can be applied to obtain a priori models. If the airframe is similar to an existing aircraft, its model can be scaled. For instance, the Digital DATCOM [53] is a purely empirical guide to estimating aerodynamic derivatives based on aircraft configuration and the experience of engineers. If the airfoils and aircraft configuration are new, one can perform analysis via the lifting line method [103], CFD [9], wind-tunnel tests or flight tests. An example of CFD analysis is shown in Figure 3.4 for the 3rd prototype high lift, rigid wing autonomous aircraft designed by Ampyx Power B.V. [3].

Depending on the available resources, combinations of these methods can be used. Within this work, the a priori aerodynamics models shown Section B are retrieved from both the lifting line method and previous flight test campaigns.

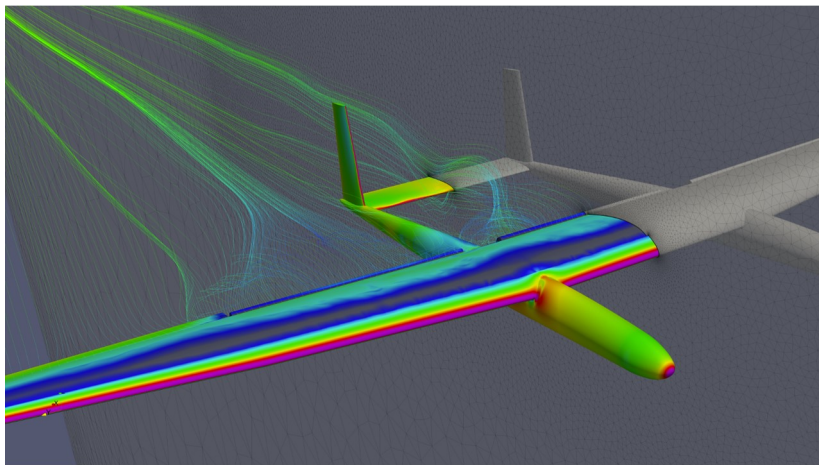


Figure 3.4: CFD of the 3rd prototype high lift, rigid wing autonomous aircraft designed by Ampyx Power B.V. [3].

3.3 Design of conventional experiments

In this section, the steady wing-level flight condition with the corresponding decoupled linear approximation of the aircraft dynamics is described. Subsequently, a widely used conventional maneuver is introduced and its features analyzed in frequency domain. Finally, the experimental data obtained from a conventional flight test campaign are shown.

3.3.1 Steady condition and decoupling of dynamics

For conventional aircraft parameter estimation experiments, a linear perturbation model structure is usually taken into account [86]. As a consequence, the flight test inputs are perturbations with respect to the steady condition. More precisely, assuming the model structure presented in section 3.2.1, the steady wing-level flight condition is held for

$$\dot{\mathbf{x}} = [\dot{V}_T, \dot{\beta}, \dot{\alpha}, \dot{\phi}, \dot{\theta}, \dot{\psi}, \dot{p}, \dot{q}, \dot{r}]^T = 0 \quad (3.6a)$$

$$\phi = p = q = r = 0 \quad (3.6b)$$

$$\delta_a = \delta_r = 0, \delta_e = \delta_{e_e}, \delta_T = \text{constant} \quad (3.6c)$$

$$V_T = V_{T_e}, \alpha = \alpha_e, \theta = \theta_e \quad (3.6d)$$

$$\gamma = \theta - \alpha = 0 \quad (3.6e)$$

where δ_T is the thrust percentage and the subscript e denotes the corresponding value at the steady regime (equilibrium point). One can numerically retrieve the steady regime for a given trimmed airspeed V_{T_e} by means of a routine based on the following optimization problem:

$$\begin{aligned} & \underset{\mathbf{x}, \mathbf{u}}{\text{minimize}} && \|\dot{\mathbf{x}}\|_2^2 \\ & \text{subject to} && \dot{\mathbf{x}} = \mathbf{f}(\mathbf{x}, \mathbf{u}, \mathbf{p}), \\ & && V_T = V_{T_e}, \\ & && \phi = 0, \\ & && \gamma = 0. \end{aligned} \quad (3.7)$$

For each equilibrium point, a linear approximation of (3.2) can be computed in the state-space form and equal to

$$\dot{\mathbf{x}} = \mathbf{A}\mathbf{x} + \mathbf{B}\mathbf{u} \quad (3.8a)$$

$$\mathbf{y} = \mathbf{C}\mathbf{x} + \mathbf{D}\mathbf{u} \quad (3.8b)$$

where the matrices \mathbf{A} , \mathbf{B} , \mathbf{C} , \mathbf{D} read as

$$\mathbf{A} = \frac{\partial \dot{\mathbf{x}}}{\partial \mathbf{x}} \quad \mathbf{B} = \frac{\partial \dot{\mathbf{x}}}{\partial \mathbf{u}} \quad \mathbf{C} = \frac{\partial \mathbf{y}}{\partial \mathbf{x}} \quad \mathbf{D} = \frac{\partial \mathbf{y}}{\partial \mathbf{u}} \quad (3.9)$$

As already mentioned in Section 3.1.1, fulfillment of the steady wing-level flight condition allows decoupling of the aircraft motion in longitudinal and lateral dynamics. The longitudinal dynamics are described via LTI state-space form by the states $\mathbf{x}_{\text{lon}} = [V_T \ \alpha \ \theta \ q]^T$, which correspond to (3.2a), (3.2c), (3.2e) and (3.2h). The aerodynamic body forces X , Z and the moment M are assumed to be linear functions of V_T , α , q and the elevator deflection δ_e , resulting in the following matrices

$$\mathbf{A}_{\text{lon}} = \begin{bmatrix} X_V & X_\alpha & -g_D \cos \theta_e & X_q \\ Z_V & \frac{Z_\alpha}{V_{T_e}} & -g_D \sin \theta_e & Z_q \\ 0 & 0 & 0 & 1 \\ M_V & M_\alpha & 0 & M_q \end{bmatrix} \quad \mathbf{B}_{\text{lon}} = \begin{bmatrix} X_{\delta_e} \\ \frac{Z_{\delta_e}}{V_{T_e}} \\ 0 \\ M_{\delta_e} \end{bmatrix} \quad (3.10)$$

where the non-zero elements are known as *dimensional aerodynamic derivatives* while θ_e is the steady-state pitch angle. The dimensional derivatives can be converted into dimensionless derivatives shown in (2.23) via the geometrical configuration of the aircraft, i.e., S , b , \bar{c} (for details see [99, 91]). The longitudinal dynamics can be further decoupled into the *Phugoid* and *Short-period* mode. The Phugoid mode is normally rather slow, slightly dampened, and dominates the response in V_T and θ , while the Short-period mode is typically fast, moderately dampened, and dominates the response in α and q . For control applications, accurate knowledge of the Phugoid mode is usually not required due to the low frequency of oscillation which is compensated via feedback control, whereas the Short-period mode is crucial for stability and performance characteristics [29].

The lateral dynamics are described analogously by the states $\mathbf{x}_{\text{lat}} = [\beta \ \phi \ p \ r]^T$, which correspond to equations (3.2b), (3.2d), (3.2g) and (3.2i). The aerodynamic body force Y and moments L and N are described by linear functions of β , p , r and inputs $\mathbf{u}_{\text{lat}} = [\delta_a \ \delta_r]^T$. The resulting matrices are given by

$$\mathbf{A}_{\text{lat}} = \begin{bmatrix} \frac{Y_\beta}{V_{T_e}} & g_D \cos \theta_e & Y_p & Y_r - V_{T_e} \\ 0 & 0 & 1 & \tan \theta_e \\ L'_\beta & 0 & L'_p & L'_r \\ N'_\beta & 0 & N'_p & N'_r \end{bmatrix} \quad \mathbf{B}_{\text{lat}} = \begin{bmatrix} \frac{Y_{\delta_a}}{V_{T_e}} & \frac{Y_{\delta_r}}{V_{T_e}} \\ 0 & 0 \\ L'_{\delta_a} & L'_{\delta_r} \\ N'_{\delta_a} & N'_{\delta_r} \end{bmatrix}, \quad (3.11)$$

and their derivatives are defined in [82]. Unlike the longitudinal dynamics, the lateral motion cannot be decoupled into independent modes. They are governed by a slow *Spiral* mode, a fast lightly damped *Dutch roll* mode, and an even faster *Roll Subsidence* mode (for details see [99]).

3.3.2 Modal analysis

As mentioned in Section 3.2.3, a priori models are useful to provide an insight into the general characteristics of the aircraft behavior. Ultimately, one analyzes the longitudinal and lateral modes described in Section 3.3.1. Each mode is characterized by a natural frequency ω_n , damping ratio δ , constant time τ , overshoot $S\%$ and period of oscillation P_O .

Table A.7 and Table A.8 collect the a priori dimensional aerodynamic derivatives for the steady wing-level flight condition with $V_{T_e} = 20$ m/s. The corresponding aircraft modes are shown in Table 3.1.

Table 3.1: Aircraft modal analysis for steady wing-level flight at $V_{T_e} = 20$ m/s

Mode	ω_n [rad/s]	δ [-]	τ [s]	$S\%$ [%]	P_O [s]
Phugoid	0.52	0.09	1.94	74.06	12.23
Short-period	3.72	0.84	0.27	0.83	3.08
Spiral	--	-1.0	11.74	--	--
Dutch roll	2.09	0.21	0.48	50.55	3.08
Roll Subsidence	--	1.0	0.09	--	--

The modal analysis suggests to design for the longitudinal motions experiments with durations longer than the Phugoid period of oscillation ($P_O = 12.23$). As far as it regards the lateral dynamics, the Spiral mode is lightly unstable which involve a significant probability to violate the flight envelope during the open-loop phase.

3.3.3 Design of conventional maneuvers

A type of maneuver which is widely used in the aerospace field due to its easy implementation and good estimation performance comes from an optimization procedure of a sequence of step functions, developed by Koehler [61]. The input signal has a bang-bang behavior with a duration $7\Delta T$ with switching times at $t = 3\Delta T$, $t = 5\Delta T$, and $t = 6\Delta T$ and amplitude A . For this reason, such an input signal is called a *3-2-1-1 maneuver* (see Figure 3.5).

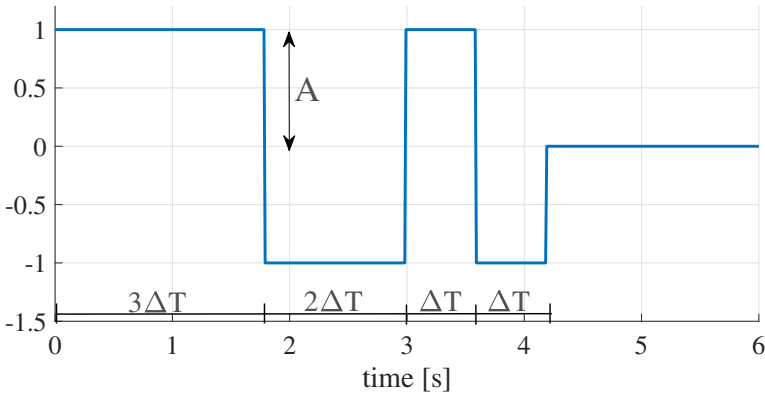


Figure 3.5: Example of a 3-2-1-1 maneuver with $A = 1$ and $\Delta T = 0.6$.

In [90], it is shown that the 3-2-1-1 maneuver provides the best estimation accuracy for both aircraft longitudinal and lateral dynamics among *Doublets*, *Mehra*, *Schulz* and *DUT* input signals. Yet, only *Doublets* and 3-2-1-1 input signals provide sufficient system excitation for identification of system responses with frequencies above 1 Hz, though the 3-2-1-1 maneuver embraces much higher frequencies compared to *Doublets*.

3.3.4 Features of the 3-2-1-1 maneuver

In general, system identification flight tests are rather time-consuming and costly, hence, it is worthwhile to design maneuvers thoughtfully in order to obtain experimental data that are sufficiently informative. 3-2-1-1 maneuvers are normally designed through both a qualitative consideration in the frequency domain [80] and a *trial-and-error* approach in order to ensure that the system response evolves within the flight envelope.

In this subsection, some features of the 3-2-1-1 signal input are shown to provide a tuning guideline for conventional maneuver.

Energy and power analysis

The parameter uncertainty is typically inversely proportional to the input power [74]. Within a time domain framework, the energy E_s and power P_s contained in a signal $x(t)$ with duration T is always bounded and equal to

$$E_s = \int_{-\infty}^{\infty} |x(t)|^2 dt \leq \infty, \quad P_s = \frac{1}{T} \int_{-\infty}^{\infty} |x(t)|^2 dt.$$

Thus, the corresponding energy and power of the 3-2-1-1 signal can be easily carried out as follows

$$E_s = A^2 \left[\int_0^{3\Delta T} dt + \int_{3\Delta T}^{5\Delta T} dt + \int_{5\Delta T}^{6\Delta T} dt + \int_{6\Delta T}^{7\Delta T} dt \right] = 7\Delta T \cdot A^2,$$

$$P_s = \frac{E_s}{7\Delta T} = A^2.$$

One can observe that the injected power of a 3-2-1-1 signal to a dynamic system increases quadratically w.r.t. the amplitude A , whereas the corresponding energy increases also proportionally as function of ΔT . Note that, high values of A and ΔT may lead the aircraft to exceed the limits of the permissible flight envelope.

Frequency content analysis

The 3-2-1-1 maneuvers are tuned in a manner that the power is concentrated within the expected bandwidth of the aircraft dynamics. In order to perform a frequency analysis, let us first define the Fourier transform for a continuous time aperiodic signal [77]:

$$X_\omega = \int_{-\infty}^{\infty} x(t) e^{-j\omega t} dt, \quad \omega = 2\pi f$$

where f denotes the frequency and $j = \sqrt{-1}$. The frequency content of a 3-2-1-1 signal is then given by

$$\begin{aligned} X_\omega &= A \left[\int_0^{3\Delta T} e^{-j\omega t} dt - \int_{3\Delta T}^{5\Delta T} e^{-j\omega t} dt + \int_{5\Delta T}^{6\Delta T} e^{-j\omega t} dt - \int_{6\Delta T}^{7\Delta T} e^{-j\omega t} dt \right] = \\ &= \frac{A}{j\omega} [1 - 2e^{-j\omega 3\Delta T} + 2e^{-j\omega 5\Delta T} - 2e^{-j\omega 6\Delta T} + e^{-j\omega 7\Delta T}]. \end{aligned}$$

The magnitude of X_ω is given by the square root of its real plus the imaginary part divided by the square of the angular velocity ω [77], i. e.,

$$|X_\omega| = \frac{\sqrt{\Re(X_\omega) + \Im(X_\omega)}}{\omega^2}$$

where the real part is equal to

$$\Re(X_\omega) = A^2 \cdot (1 - 2c(3\omega\Delta T) + 2c(5\omega\Delta T) - 2c(6\omega\Delta T) + c(7\omega\Delta T))^2$$

while the imaginary part read as

$$\Im(X_\omega) = A^2 \cdot (2s(3\omega\Delta T) - 2s(5\omega\Delta T) + 2s(6\omega\Delta T) - s(7\omega\Delta T))^2$$

with c and s the shortening of $\cos(\cdot)$ and $\sin(\cdot)$, respectively. One can then compare $|X_\omega|$ w.r.t. the cut-off frequency $f_c = 3\text{dB}$ in order to obtain an insight about the excited frequencies. As a matter of example, Figure 3.6 shows the frequency content of a 3-2-1-1 signal with $A = 5$ and $\Delta T = 0.8\text{ s}$ overlapped with the a priori aircraft modes collected in Table 3.1. In this case, the parameters relative to the Phugoid and Dutch roll mode are likely to be more accurate w.r.t. the parameters corresponding to the Spiral and Short-period mode. Note that, parametric uncertainty depends also on other factors, e.g., when the parameters that need to be estimated are physically insignificant with respect to the measured system response and/or it exists some correlation between them [98, 101].

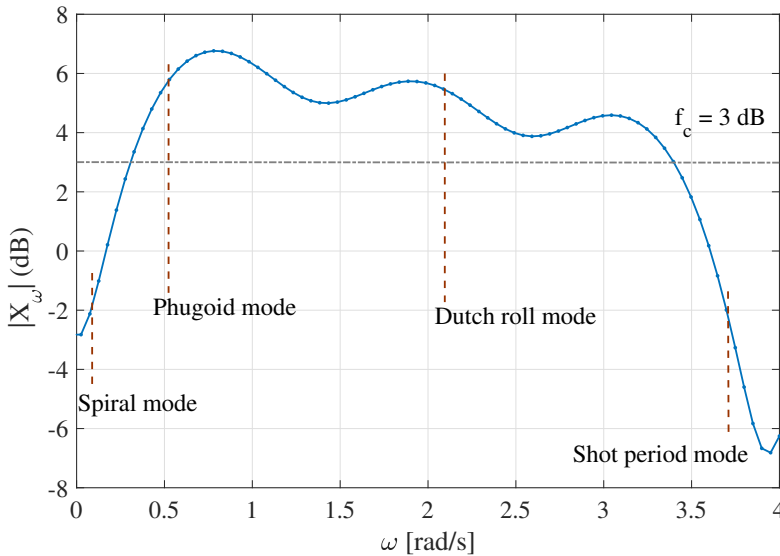


Figure 3.6: Frequency content of a 3-2-1 maneuver with $A = 5$ and $\Delta T = 0.8$ s and analysis of the a priori aircraft modes.

3.3.5 Experimental data

A total of three experimental data sets are collected with trimmed airspeed $V_{T_e} = 20$ m/s within one single flight campaign and with an average (estimated) wind speed ≈ 7 m/s. The experiments are performed with conventional maneuvers 3-2-1-1 and they are shown in Figure 3.7. One can observe the decoupling between the Phugoid mode which dominates the airspeed V_T and pitch θ responses, and the fast changes on the angle of attack α and pitch rate q coming from the Short-period mode. As mentioned in Section 3.1.1, during the excitation of the longitudinal dynamics, the lateral motion is stabilized by aileron δ_a and rudder δ_r deflection. Figure 3.8 shows the lateral dynamics relative to the three experiments.

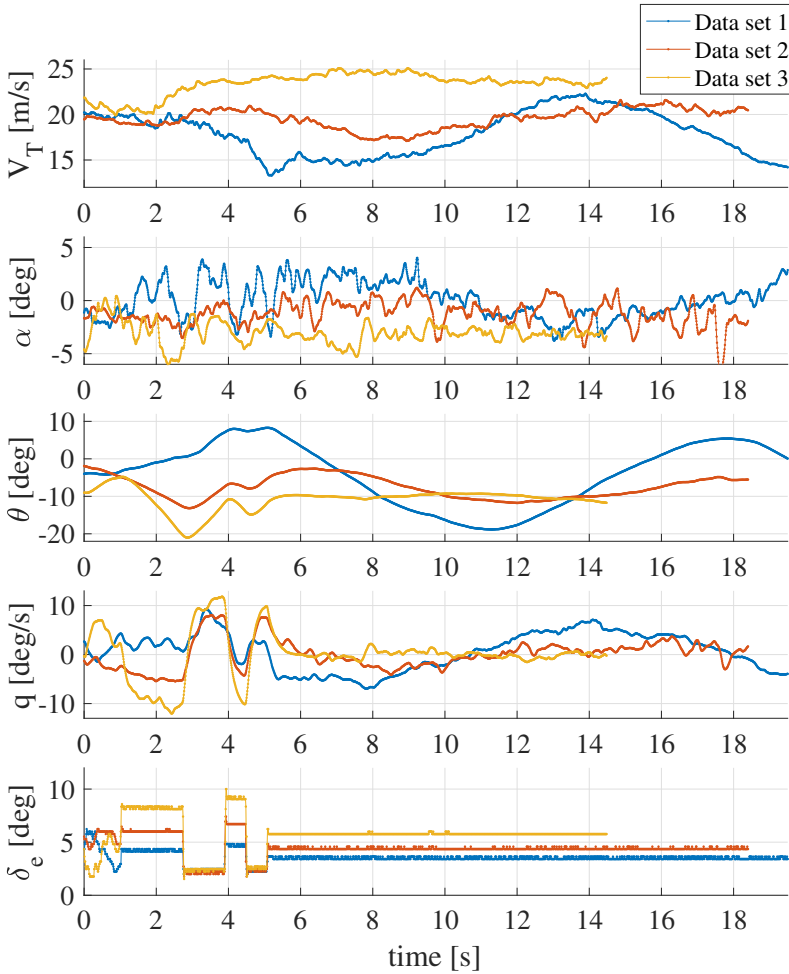


Figure 3.7: **[Experimental data]** Three experimental data sets obtained through conventional maneuvers ($V_{T_e} = 20$ m/s). Average wind speed ≈ 7 m/s.

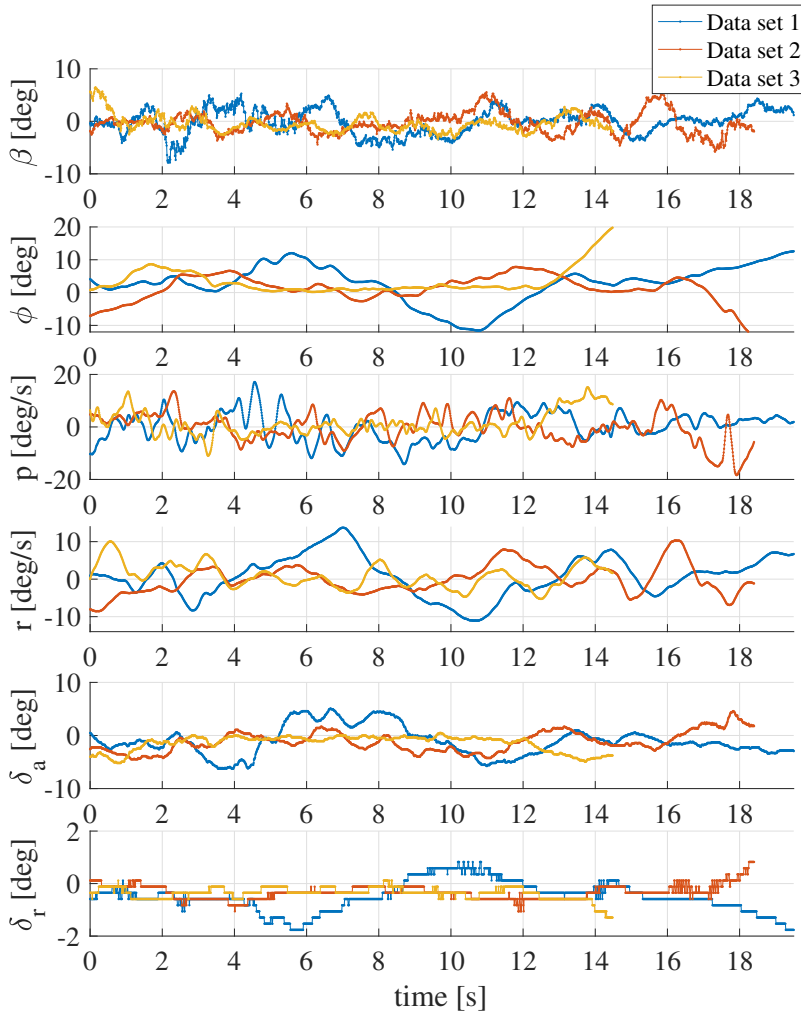


Figure 3.8: **[Experimental data]** Stabilization of lateral dynamics by δ_a and δ_r during excitation signal along the longitudinal dynamics via conventional maneuvers ($V_{T_e} = 20$ m/s). Average wind speed ≈ 7 m/s. Note that, roll rate p and roll angle ϕ appear sensitive to the turbulence, which involves a major control effort from the aileron deflection δ_a in order to both stabilize this axis and prevent flight envelope violation.

3.4 Design of optimal experiments

In this section, an introduction to optimal input design for aircraft parameter estimation is given and the formulation of an Optimum Experimental Design (OED) problem is provided. The optimal maneuvers are carried out for the longitudinal and lateral dynamics and their performance assessed with their respective initial maneuvers via the Cramer-Rao Lower Bound (CRLB). Afterwards, the optimized inputs are first validated via reliable flight simulator and subsequently experimental data coming from a real flight test campaign are shown.

3.4.1 Historical background and motivation

In the estimation of aerodynamic derivatives from flight tests, the design of the signal input provided for the system during experimental data collection is crucial for the accuracy of the subsequent parameter estimation. If a signal is not suitable for sufficient excitation of the relevant system dynamics, the data obtained during an experiment might not contain enough information on the desired parameters to allow for good estimation results. This creates the need for a systematic design of optimal input signals for flight test maneuvers.

In the aerospace field, the importance of choosing appropriate control inputs for extraction of the aerodynamic derivatives from flight test data was first noticed by Gerlach [43]. He proposed a qualitative method for the determination of optimal frequencies in scalar input signal to linear second order systems [42]. Important contribution to the theory and practice of the calculation of optimal aircraft input signals have been made subsequently by Mehra [83, 84, 85]. Based on the work of Kiefer, Wolfowitz [60] and Kiefer [59], Mehra proposed algorithms for the design of scalar and multi-dimensional input signals in the frequency domain as well as in time domain. An efficient method was implemented by Morelli where dynamics programming techniques were used to determine the optimal switching time of a input signal [87]. The resulting input signals were of the *bang-bang* type. Morelli's approach was afterwards applied by Cobleigh [27] and the resulting input signals were implemented by Noderer [94] for validation using real flight test data from an X-31 drop model. Nowadays optimal inputs are mainly designed for [70, 86]:

- reducing the number of expensive system identification flight tests,
- minimizing the length of flight test maneuver necessary to reach a specified level of accuracy of the aerodynamic derivatives,

- refinement and validation of the aerodynamic derivatives for control system analysis and design purposes and
- aircraft acceptance testing.

A fundamental problem in the design of input signals for parameter estimation is that the optimized design itself depends on the actual values of the unknown system parameters. As a consequence, these values would need to be known before the actual flight tests are made in order to optimize the experimental setup. However, if the parameters were already known, an estimation would obviously no longer be necessary. This problem is known as *circularity problem* [90]. Due to that, the optimal input design combined with parameter identification are used in practice in an iterative fashion, starting from a sufficient initial guess on the parameter values until a desired level of accuracy for the estimated values is met, as also shown in Figure 3.9.

3.4.2 Optimum experimental design formulation

The main idea of OED is to use an information function $\Psi(\cdot)$ of the Fisher information matrix \mathbf{F} as the objective of an optimization problem. The Fisher information matrix can then be expressed as

$$\mathbf{F} = \sum_{i=1}^N \left[\left(\frac{\partial \mathbf{y}(i)}{\partial \mathbf{p}} \right)^T \boldsymbol{\Sigma}_{\mathbf{y}}^{-1} \left(\frac{\partial \mathbf{y}(i)}{\partial \mathbf{p}} \right) \right] \quad (3.13)$$

where the inverse of the Fisher information matrix \mathbf{F}^{-1} , which corresponds to the covariance matrix of the estimated parameters $\boldsymbol{\Sigma}_{\mathbf{p}} \in \mathbb{R}^{n_{\mathbf{p}}} \times n_{\mathbf{p}}$, yields an universal lower bound on parameter estimation accuracies known as the CRLB. Basically, the CRLB allows the optimization of the input signal regardless of the type of estimation algorithm implemented [87].

Different information functions can be used in the optimization problem with different features [50, 92, 93]. However, within this work the *A-criterion* is chosen as information function in the OED problem [83]. The resulting input signals are called *A-optimal* and they are obtained by minimizing the summation of the diagonal element of the CRLB, i. e.,

$$\Psi_{\mathbf{A}}(\boldsymbol{\Sigma}_{\mathbf{p}}) = \frac{1}{n_{\mathbf{p}}} \cdot \text{trace}(\boldsymbol{\Sigma}_{\mathbf{p}}) = \frac{1}{n_{\mathbf{p}}} \sum_{i=1}^{n_{\mathbf{p}}} \boldsymbol{\Sigma}_{\mathbf{p}(i,i)} = \frac{1}{n_{\mathbf{p}}} \sum_{i=1}^{n_{\mathbf{p}}} \text{Var}(\mathbf{p}_{(i)}), \quad (3.14)$$

so that using $\Psi_{\mathbf{A}}(\cdot)$, one optimize the experimental setup in terms of minimizing the sum of the variances of the unknown parameters.

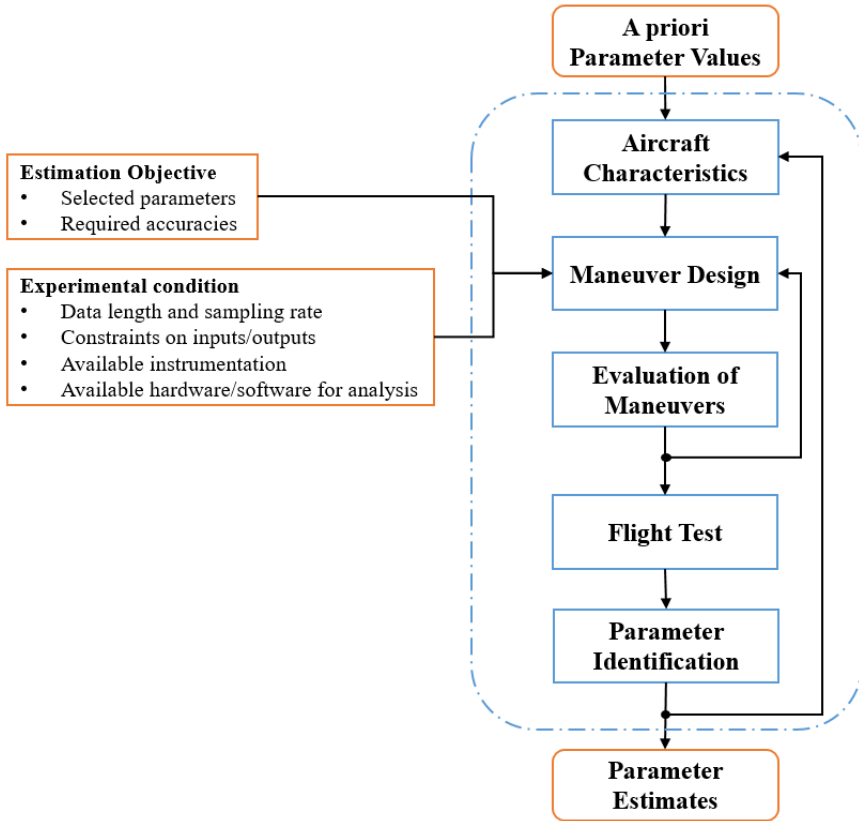


Figure 3.9: Optimal input design within identification procedure [90].

Ultimately, a general model-based OED problem which considers input and output constraints can be formulated in continuous time as follows

$$\underset{\mathbf{x}(\cdot), \mathbf{u}(\cdot)}{\text{minimize}} \quad \Psi(\Sigma_{\mathbf{p}}[\mathbf{x}(\cdot), \mathbf{u}(\cdot), \mathbf{p}]) \quad (3.15a)$$

$$\text{subject to:} \quad \dot{\mathbf{x}}(t) = \mathbf{f}(\mathbf{x}(t), \mathbf{u}(t), \mathbf{p}), \quad t \in [0, T], \quad (3.15b)$$

$$\mathbf{x}(0) = \mathbf{x}_0, \quad (3.15c)$$

$$\mathbf{u}_{\min} \leq \mathbf{u}(t) \leq \mathbf{u}_{\max}, \quad t \in [0, T], \quad (3.15d)$$

$$\mathbf{x}_{\min} \leq \mathbf{x}(t) \leq \mathbf{x}_{\max}, \quad t \in [0, T]. \quad (3.15e)$$

Finally, note that the A-criterion allows the prioritization of the estimation errors of some parameters by selecting the trace of the product matrix obtained by multiplying $\Sigma_{\mathbf{p}}$ with a weighting matrix [90].

3.4.3 Algorithm implementation

Within this work, the optimum experimental designs are computed using CASIOPEIA, an open-source tool for PE and OED [23] based on CASADI [10]. CASIOPEIA computes the covariance matrix $\Sigma_{\mathbf{p}}$ from the inverse of the KKT Matrix of the underlying parameter estimation problem using a Schur complement approach. Details on method and implementation can be found in [24].

Provided the system dynamics (3.15b), a discretization time grid, bound specifications for variables as in (3.15d) and (3.15e) and an initial guess for the parameter values \mathbf{p}_{init} and for the input signal \mathbf{u}_{init} , the continuous-time optimization problem is discretized and formulated as a NLP automatically by CASIOPEIA using direct collocation [20] with Lagrange polynomials. The resulting NLP is solved using IPOPT [104] with linear solver MA86 [56] to obtain improved input signals \mathbf{u}_{opt} .

If for the initial values \mathbf{p}_{init} of the parameters used within OED it holds for two parameters $p_i, p_j \in \mathbf{p}$ with $i \neq j$ that $\mathbf{p}_{\text{init},i} > \mathbf{p}_{\text{init},j}$, it is likely that $\text{Var}(p_i) > \text{Var}(p_j)$. Due to the higher contribution of $\text{Var}(p_i)$ to (3.15a), the optimizer then might overly increase certainty of p_i while disregarding to increase or even decreasing certainty of p_j . Due to that, \mathbf{p} is within the OED problem formulations of this work not introduced by the values of \mathbf{p}_{init} , but as a vector of entries with unit values scaled by the corresponding entries of \mathbf{p}_{init} to reduce the effects of the numerical values of \mathbf{p}_{init} on the OED result.

3.4.4 Constraints selection

In practice, it is hardly possible to apply input signals which correspond to full deflection of the control surfaces without exceeding the limits of the permissible flight envelope. On the one hand, one must scale down the input signal amplitude in order to restrict the aircraft response within a region for which the model structure assumed in (3.2) is valid. On the other hand, if input signals are scaled up, then the estimation accuracy is enhanced due to a higher SNR. Therefore, constraints in (3.15d) and (3.15e) should be enforced in order to ensure the system response close to a specific steady wing-level flight condition without any flight envelope violation and at the same time guarantee an acceptable SNR. In this work, constraints for the OED problem 3.15 have been chosen as follows:

- control surface deflections ($\delta_a, \delta_e, \delta_r$), angle of attack α as well as the airspeed V_T were constrained in order to keep the aircraft within the region where the linear model should still be applicable;
- After a state augmentation of the longitudinal and lateral LTI representation shown in (3.10) and (3.11), the rate of control surface deflections ($\dot{\delta}_a, \dot{\delta}_e, \dot{\delta}_r$) are constrained in agreement with the maximum speed of the installed servos;
- the body angular rates (p, q, r) and Euler angles (ϕ, θ, ψ) are bounded with respect to the flight envelope limits since any violation of the flight envelope would result in abortion of the system identification test. To account for model mismatch and inaccuracies of the a priori model, these bounds were enforced with a safety margin of 20% w.r.t. the flight envelope limits.

Table A.9 collects the flight envelope, input and state constraints taken into account during the system identification flight test performed with optimized maneuvers.

3.4.5 Control input initialization

The optimization problem 3.15 needs to be initialized with a suitable, initial input signal \mathbf{u}_{init} . Within this work, the 3-2-1-1 maneuvers are chosen through both a qualitative consideration in the frequency domain described in Section 3.3.4 and a *trial-and-error* approach in order to ensure that the system response is within the prescribed constraints [80].

3.4.6 Flight tests optimization

Three OED problems 3.15 are computed, one for the longitudinal dynamics (3.10) and two for the lateral dynamics (3.11). Since only one single axis can be excited at a time, when the aileron is chosen as input, the rudder is assumed zero along the entire experiment. As a consequence, the aerodynamic derivatives relative to the rudder ($Y_{\delta_r}, L'_{\delta_r}, N'_{\delta_r}$) will be *structurally unidentifiable* with \mathbf{F} not of full rank. In this case, one has to discard the corresponding unidentifiable parameters to prevent rank deficiency of \mathbf{F} [90]. Same considerations are valid in the case when the rudder is used as input and the aileron is kept zero. Note that in practice, when the roll axis is excited by aileron deflection, the rudder stabilizes the yaw axis (and the elevator the pitch axis) during the entire system identification experiment. Hence, the rudder control surface will slightly differ from zero. For the sake of comparability, the amplitude of \mathbf{u}_{init} and \mathbf{u}_{opt} are set equal. The optimized experiment lengths are set to 10 s to ensure the full sequence is completed in the available flight test area taking into account variations in the wind conditions on the flight test day(s). As a consequence, dynamics at frequencies below 0.1 Hz cannot be identified accurately, in this case the Phugoid and Spiral mode. Nevertheless, for control applications accurate knowledge of low frequency modes are not crucial and they are easily compensated via feedback control [29].

The responses of the a priori LTI systems for the optimized inputs obtained from the solution of the OED problem are shown in Figures 3.10, 3.11, 3.12 with the corresponding responses to the 3-2-1-1 maneuvers used as initialization.

It turns out that the OED problem based on the A-criterion leads to a *bang-bang* type input signal. Such outcome is in agreement with analytic results [25] and previous flight test evaluations which demonstrate that square wave type inputs are superior to sinusoidal type inputs for parameter estimation experiments, largely due to their wider frequency spectrum [89]. More precisely, the signal inputs resemble modulated square waves with a finite slope due to the rate of deflection constraints.

Likewise for the experimental data obtained with conventional 3-2-1-1 maneuvers and shown in Figure 3.7, one can observe Figure 3.10 the decoupling between the Phugoid mode which dominates the airspeed V_T and pitch θ responses, with the fast changes on the angle of attack α and pitch rate q coming from the Short-period mode.

In Figure 3.11, the optimal lateral response caused by the aileron deflection shows a good excitation on the roll rate p . The cross-coupling involves a modest excitation on the yaw rate r and side-slip angle β whereas the roll angle ϕ drifts slowly towards the edge of the admissible range due to the unstable *Spiral* mode.

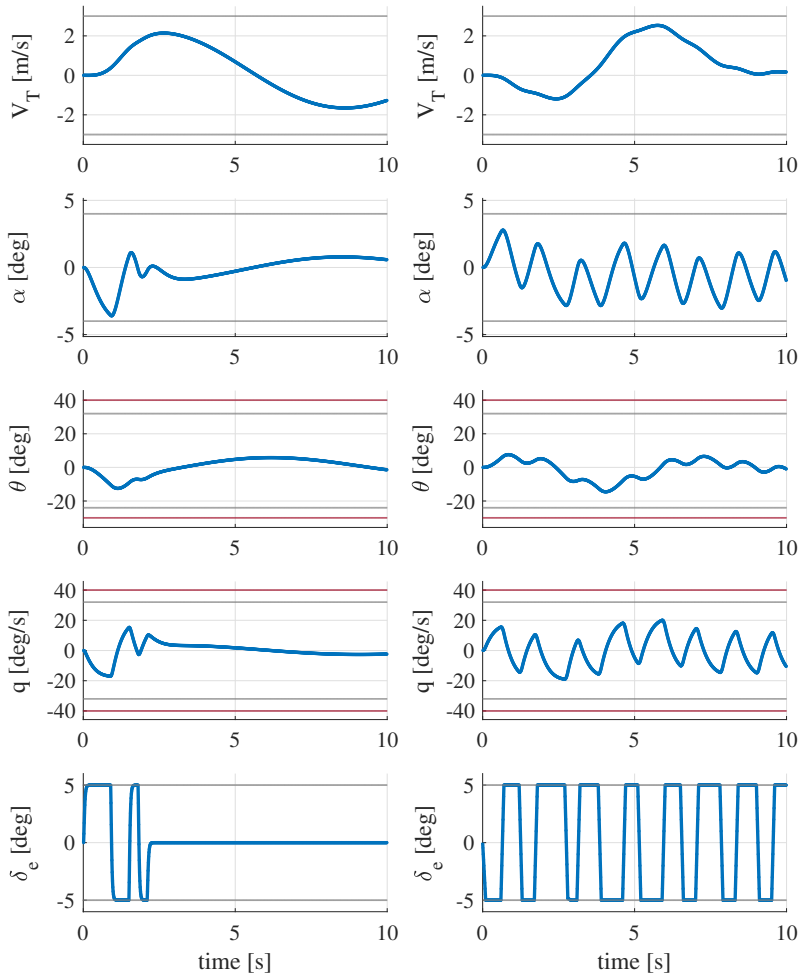


Figure 3.10: **[Simulation data]** Initial longitudinal response using the 3-2-1-1 maneuver (left column) and optimal response (right column). In grey line the OED constraints whereas in dark red line the flight envelope.

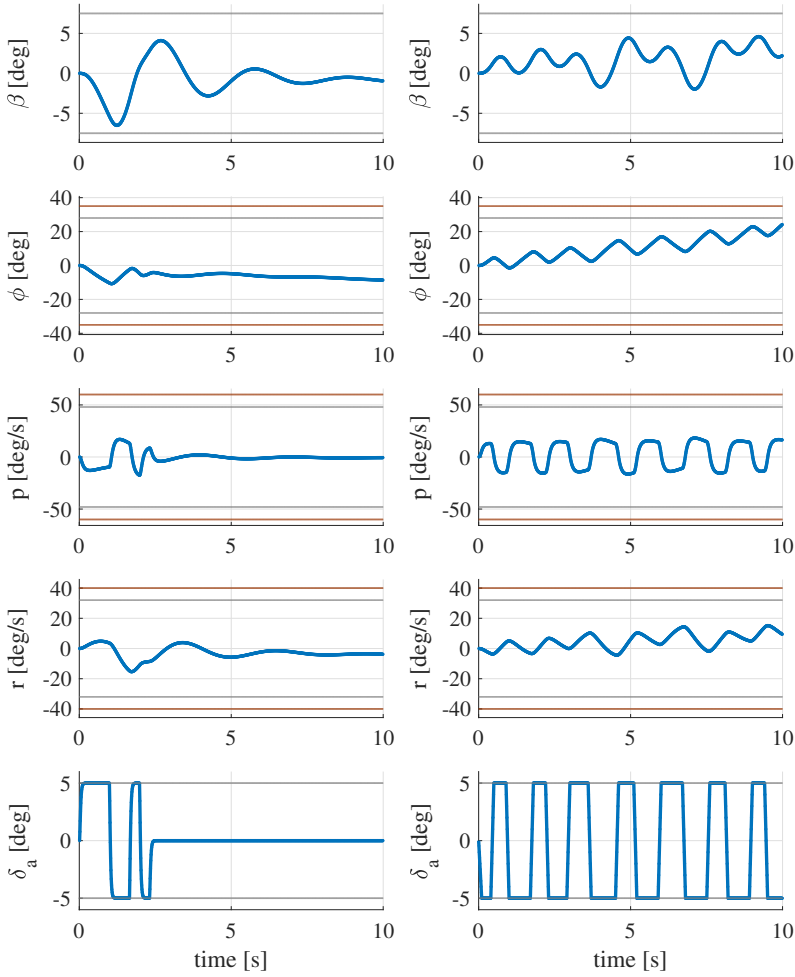


Figure 3.11: **[Simulation data]** Initial lateral response via aileron deflection using the 3-2-1 maneuver (left column) and optimal response (right column). In grey line the OED constraints whereas in dark red line the flight envelope.

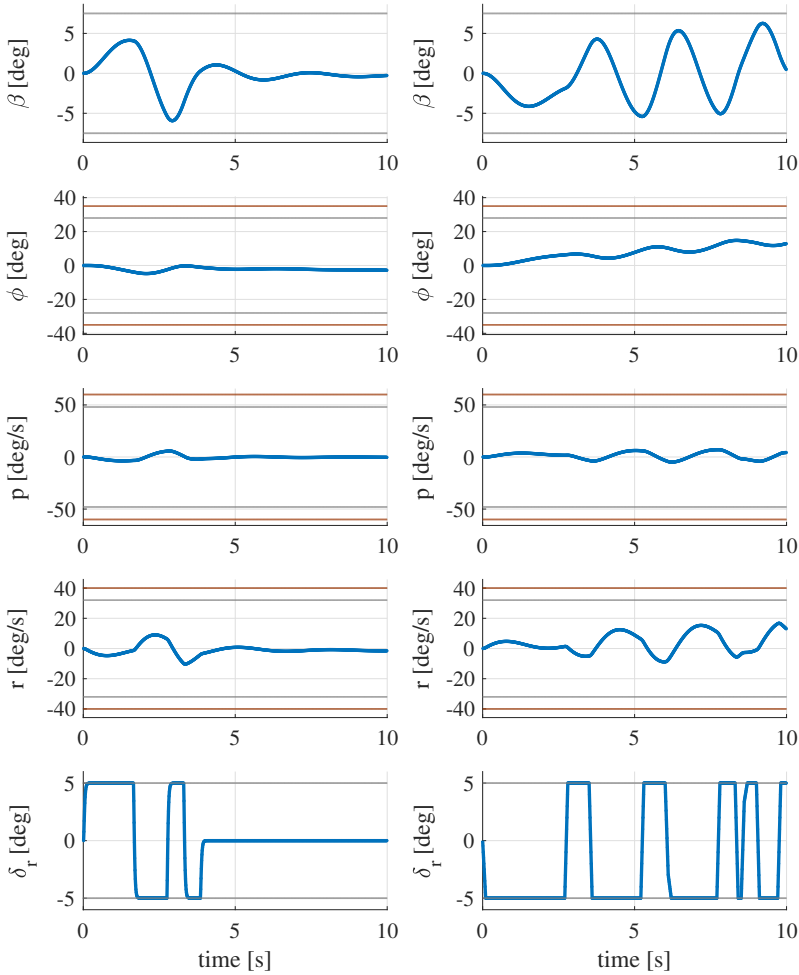


Figure 3.12: [Simulation data] Initial lateral response via rudder deflection using the 3-2-1-1 maneuver (left column) and optimal response (right column). In grey line the OED constraints whereas in dark red line the flight envelope.

Regarding the yaw excitation via rudder deflection depicted in Figure 3.12, an optimal response would be provided by setting the rudder at the maximum allowable deflection for approximately 3s such that an oscillatory motion with a gradual increment on amplitude on the side slip angle β as well as the roll rate r is triggered. Subsequently, a bang-bang behavior is carried out so as to avoid constraint violations. The roll rate p is barely excited due to cross-coupling though, roll angle ϕ slowly diverges as in the previous case.

3.4.7 Performance assessments

In this section, optimal maneuvers are assessed by the CRLB which is the theoretical lower limits for parameter standard errors using an efficient and asymptotically unbiased estimator, such as maximum likelihood [87]. The CRLB depends on the diagonal entries of the Fisher information matrix \mathbf{F} (3.13) and formally the following inequality is held [98, 101]

$$\sigma_i \geq \text{CRLB}_i = \frac{1}{\sqrt{\mathbf{F}_{ii}}}. \quad (3.16)$$

A performance analysis of signal inputs computed via the CRLB isolates the merits of the input design from the merits of the parameter estimation algorithm used to extract the aerodynamic derivatives from the flight data [86]. Yet, the relation between the parametric uncertainty and CRLB allows to form a comprehensive uncertain aircraft model.

Several factor can cause high CRLB values, e. g.:

- from a optimization point of view, large values for CRLB_i denote a low curvature in the cost function, i. e., a high insensitivity with respect to the i^{th} parameter [101];
- from a system identification point of view, high CRLB values indicate either that the i^{th} parameter is physically insignificant with respect to the measured aircraft response or that there exists a correlation between parameters, i. e., these parameters can vary together, making their individual values difficult to determine [98].

Tables 3.2, 3.3, 3.4 show the CRLB values for the optimal system responses (CRLB_{opt}) with the corresponding initial responses ($\text{CRLB}_{\text{init}}$) whereas $\Delta\text{CRLB}_{\%}$ indicates the percent deviation between CRLB_{opt} and $\text{CRLB}_{\text{init}}$. A negative value for $\Delta\text{CRLB}_{\%}$ indicates an improvement in terms of estimation accuracy for the i^{th} parameter, and vice versa for positive values.

The optimal signal input for the longitudinal dynamics (Table 3.2, Figure 3.10) provides an overall increment of $\approx 40\%$ in terms of estimation accuracy.

Table 3.2: Dimensional aerodynamic derivatives longitudinal dynamics

Derivatives	Value	CRLB _{init}	CRLB _{opt}	ΔCRLB%
X_V	-0.147	0.1978	0.1147	-42.0
X_α	7.920	14.0706	8.6891	-38.2
X_q	-0.163	2.9936	1.5916	-46.8
X_{δ_e}	-0.232	3.4318	1.9859	-42.1
Z_V	-0.060	0.0007	0.0004	-42.0
Z_α/V_{T_e}	-4.400	0.0491	0.0303	-38.2
Z_q	0.896	0.0104	0.0056	-46.8
Z_{δ_e}/V_{T_e}	-0.283	0.0120	0.0069	-42.1
M_α	-7.688	0.0098	0.0061	-38.2
M_q	-1.963	0.0021	0.0011	-46.8
M_{δ_e}	-10.668	0.0024	0.0014	-42.1

Table 3.3: Dimensional aerodynamic derivatives lateral dynamics: aileron input

Derivatives	Value	CRLB _{init}	CRLB _{opt}	ΔCRLB%
Y_β/V_{T_e}	-0.167	0.8907	1.1087	24.5
Y_r	-0.976	0.3825	0.3526	-7.8
Y_{δ_a}/V_{T_e}	-0.046	1.7305	0.5869	-66.1
L'_β	-8.201	0.8907	1.1087	24.5
L'_p	-11.292	0.6856	0.1504	-78.1
L'_r	3.853	0.3825	0.3526	-7.8
L'_{δ_a}	-32.600	1.7305	0.5869	-66.1
N'_β	3.214	0.8907	1.1087	24.5
N'_p	-0.750	0.6856	0.1504	-78.1
N'_r	-0.457	0.3825	0.3526	-7.8
N'_{δ_a}	0.716	1.7305	0.5869	-66.1

Though, as expected, the parameters determined by the Phugoid mode, i. e., X_V , X_α , X_q and X_{δ_e} , are still subject to high uncertainty due to the time window of the experiment set to 10 s. Yet, the 3-2-1-1 maneuver used as initial signal input provides more than the acceptable accuracy for Z_V , Z_α , Z_q , Z_{δ_e} , M_α , M_q and M_{δ_e} which are derivatives related to the Short-period mode.

The optimal lateral response via aileron deflection (Table 3.3, Figure 3.11), reduce mainly the uncertainty on the approximation of the aileron to roll rate transfer function which is $\frac{p(s)}{\delta_a(s)} = \frac{L'_{\delta_a}}{s-L'_p}$ [99]. The contribution of Y_{δ_a} with respect to the overall aircraft response appears negligible for this steady configuration, hence its uncertainty will be high in the optimal case, too. On the other hand, significant increment in terms of accuracy is shown in N'_p

Table 3.4: Dimensional aerodynamic derivatives lateral dynamics: rudder input

Derivatives	Value	CRLB _{init}	CRLB _{opt}	ΔCRLB%
Y_β/V_{T_e}	-0.167	10.0229	3.0396	-69.7
Y_r	-0.976	3.3870	0.9643	-71.5
Y_{δ_r}/V_{T_e}	0.093	1.3518	0.5674	-58.0
L'_β	-8.201	10.0229	3.0396	-69.6
L'_p	-11.292	12.2297	3.7003	-69.7
L'_r	3.853	3.3870	0.9643	-71.5
L'_{δ_r}	0.524	1.3518	0.5674	-58.0
N'_β	3.214	10.0229	3.0396	-69.6
N'_p	-0.750	12.2297	3.7003	-69.7
N'_r	-0.457	3.3870	0.9643	-71.5
N'_{δ_r}	-2.370	1.3518	0.5674	-58.0

and N'_{δ_a} which are parameters relative to the yaw moment due to the roll rate p and aileron deflection δ_a , respectively. One can observe that remain derivatives are either poorly improved (Y_r, L'_r, N'_r) or they experience a loss of accuracy ($Y_\beta, L'_\beta, N'_\beta$). This is not surprising since these derivatives are all related to the yaw dynamics which is barely excited during aileron deflection.

Finally, Table 3.4 shows that the optimal rudder deflection in Figure 3.12 provides a meaningful improvement mainly on parameters relative to the yaw dynamics.

3.4.8 Effects of parameter uncertainties on the a priori model

In section 3.4.6, the optimized maneuvers are obtained via an optimization problem which depends on a priori model with unknown system parameters. A priori models are prone to parametric uncertainty, therefore, one may wonder what is the impact of a certain degree of uncertainty on the a priori model within an OED framework. For this reason, let us consider three hypothetical cases that may occur on a flight test campaign:

- a case during the preliminary phase of the flight test campaign where aerodynamic derivatives may come exclusively from analytical tools, hence high inaccuracies might be present;
- a case during an intermediate stage of the flight test campaign where aerodynamic derivatives rely on both simulation and previous (conventional) flight tests, hence reasonable estimates are expected;

- a case after an extensive flight test campaign where aerodynamic derivatives are likely to have high accuracy.

Let us further assume that the a priori parameters \mathbf{p}_{init} deviate in percentage w.r.t. the "true" parameters \mathbf{p} by $\Delta\mathbf{p}_{\%} = 100\%$, $\Delta\mathbf{p}_{\%} = 20\%$ and $\Delta\mathbf{p}_{\%} = 5\%$, respectively. For each case, an OED problem which takes into account the longitudinal dynamics is initialized and solved using 3-2-1-1 maneuvers designed in agreement with the a priori models subject to parametric uncertainty (see Figure 3.13). For the sake of comparability, the maneuvers are injected into the "true model" in order to verify the impact of the 3-2-1-1 maneuvers based on inaccurate models.

Figure 3.14 shows the optimal responses for the cases taken into account. Similarly to the nominal case in Section 3.4.6, the OED problem leads to a three *bang-bang* type input signals. Furthermore, the angle of attack α , pitch angle θ and pitch rate q approach to a sinusoidal response while the airspeed V_T increases in agreement with the prescribed constraints. Finally, note that even for the worst case taken into account ($\Delta\mathbf{p}_{\%} = 100\%$), there is no significant constraints violation.

One can graphically get an insight about the estimation accuracy improvement by means of the $1\text{-}\sigma$ confidence ellipsoids obtained by the inverse of \mathbf{F} , i.e., the covariance matrix $\Sigma_{\mathbf{p}}$. As a matter of example, in Figure 3.15 it is shown the comparison between the initial and optimal $1\text{-}\sigma$ confidence ellipsoids for the pair of estimates (M_q, M_{α}) . In all cases, the optimized maneuvers provide better estimation accuracy w.r.t. 3-2-1-1 maneuvers, though, the correlation between parameters is unchanged. This is not surprising since the A-criterion implemented within the OED problem takes only into account the diagonal entries of $\Sigma_{\mathbf{p}}$.

Likewise in Section 3.4.7, the optimal maneuvers can be assessed by the CRLB. 3.5 shows the deviation in percentage of the CRLB between the initial and optimized maneuvers relative to the three scenarios considered within this subsection. As before, a negative value means an improvement in terms of estimation accuracy and vice versa for positive values.

One can observe that more reliable a priori models facilitate higher information content of the optimized experiments w.r.t the conventional one. However, for high parameter inaccuracies an overall loss of estimation performance is shown. In summary, it is advisable to apply conventional signal inputs such as 3-2-1-1 maneuver during the preliminary stage of a flight test campaign when high inaccuracies are expected, and subsequently refine the estimates via optimal maneuvers.

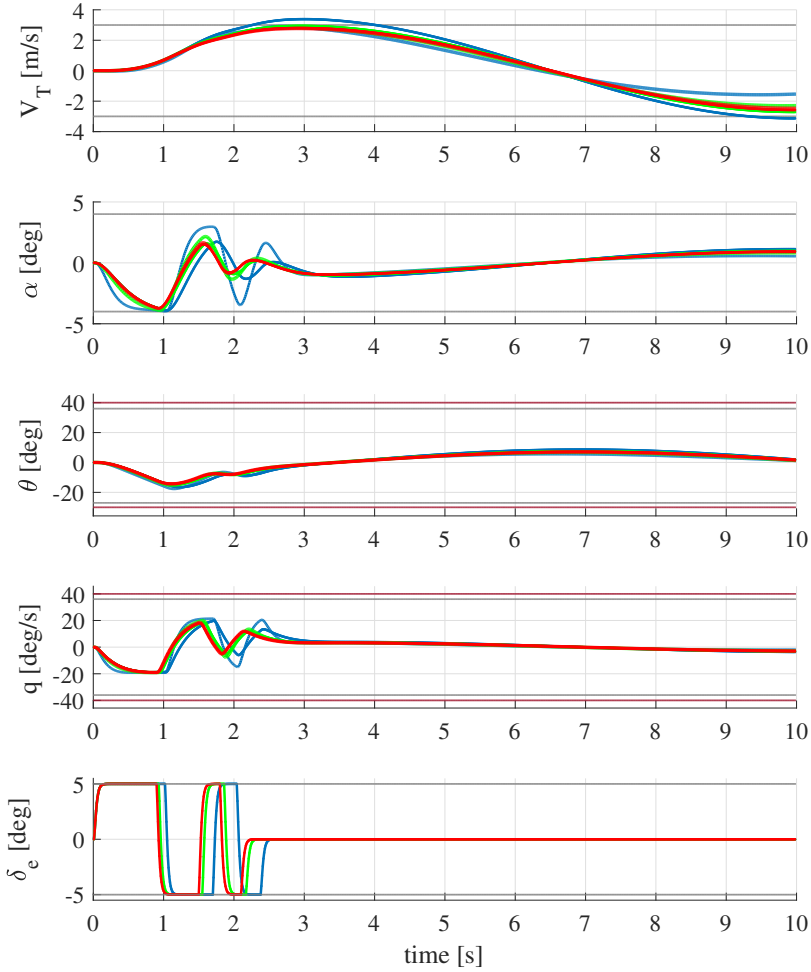


Figure 3.13: **[Simulation data]** Output response using 3-2-1-1 maneuvers. The a priori model responses are in dot line while the "true" model responses are in solid line. The output responses are in blue line for the case $\Delta p\% = 100\%$, green line for the case $\Delta p\% = 20\%$, red line for the case $\Delta p\% = 5\%$. Flight envelope limits in dark red dash-dot line while the enforced constraints are in grey dash line.

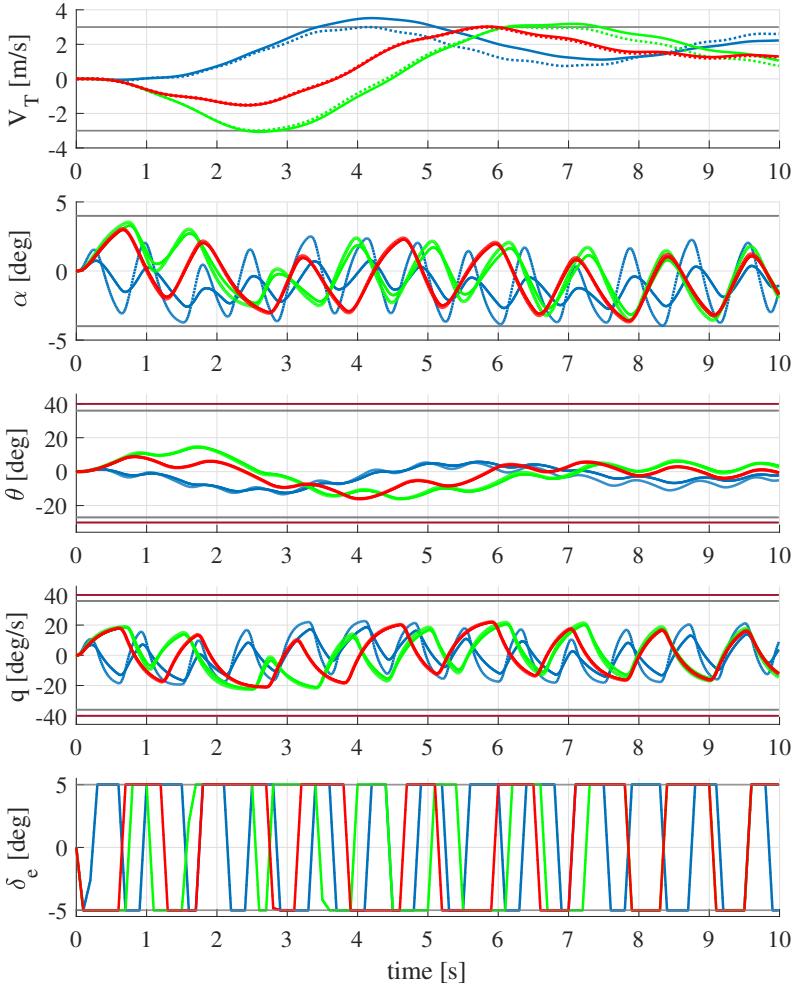


Figure 3.14: **[Simulation data]** Output response using optimized maneuvers. The a priori model responses are in dot line while the "true" model responses are in solid line. The output responses are in blue line for the case $\Delta \mathbf{p}_{\%} = 100\%$, green line for the case $\Delta \mathbf{p}_{\%} = 20\%$, red line for the case $\Delta \mathbf{p}_{\%} = 5\%$. Flight envelope limits in dark red dash-dot line while the constraints are in grey dash line.

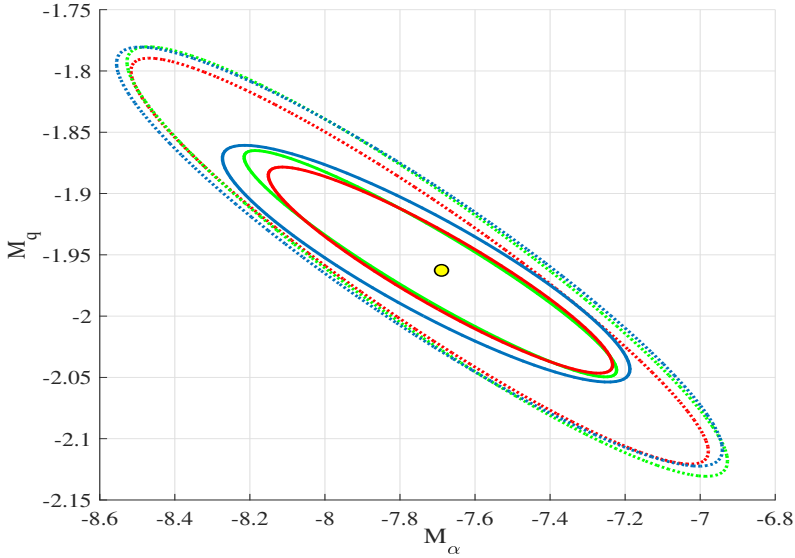


Figure 3.15: [Simulation data] Comparison between initial (dot lines) and optimal (solid lines) 1- σ confidence ellipsoids for the pair of estimates (M_q, M_α) . Blue line denotes the case $\Delta p\% = 100\%$, green line the case $\Delta p\% = 20\%$ and red line the case $\Delta p\% = 5\%$.

Table 3.5: CRLB reduction in percentage relative to the longitudinal derivatives.

Derivatives	$\Delta \text{CRLB}\%$		
	$\Delta p\% = 100\%$	$\Delta p\% = 20\%$	$\Delta p\% = 5\%$
X_V	+28.85%	-36.24%	-38.22%
X_α	+24.75%	-36.33%	-37.81%
X_q	+20.79%	-36.62%	-39.50%
X_{δ_e}	-19.0%	-36.92%	-39.94%
Z_V	-2.47%	-26.98%	-31.58%
Z_α/V_{T_e}	-16.13%	-37.01%	-37.84%
Z_q	-28.82%	-44.96%	-45.20%
Z_{δ_e}/V_{T_e}	-36.63%	-36.48%	-41.17%
M_α	-19.21%	-30.52%	-36.71%
M_q	-35.0%	-41.24%	-44.81%
M_{δ_e}	-41.29%	-36.61%	-40.59%

3.4.9 Signal inputs set-up and safety assessments

As already mentioned, the case study is an autonomous system hence, a flight plan must be set. The FCC of the case study allows to define control surfaces demands as steps with tunable amplitude and time length only. Therefore, the steps transition shown in Figures 3.10, 3.11, 3.12 are approximated as tight step functions as in Figure 3.5. Before that any real system identification flight test can be performed, each signal input need to be validated via reliable flight simulator for different wind conditions as well as degree of parameter uncertainty so as to get a better confidence relative to the safety of the flight test.

The results obtained from the high fidelity simulator designed by Ampyx Power B.V. [3] show that the aircraft is able to complete successfully the system identification flight test with optimal elevator deflection and rudder without any flight envelope violation, providing good excitation of the longitudinal and yaw dynamics, respectively. As far as it regards the excitation of the lateral dynamics via aileron deflection, it turns out that the vehicle is prone to loss of the flight path due to cross-coupling effects and unstable Spiral mode (see Figure 3.16 and Figure 3.17).

Therefore, for safety reasons part of the optimal aileron sequence is discarded and propulsion system are not turned off in order to avoid significant deviation from the steady condition. Note that, the thrust effect provides negligible model mismatch on the roll axis. Alternatively, one could superimpose the pilot command with the actual optimal signal input so as to prevent loss of track, though degradation of the estimation accuracy might occurs [35].

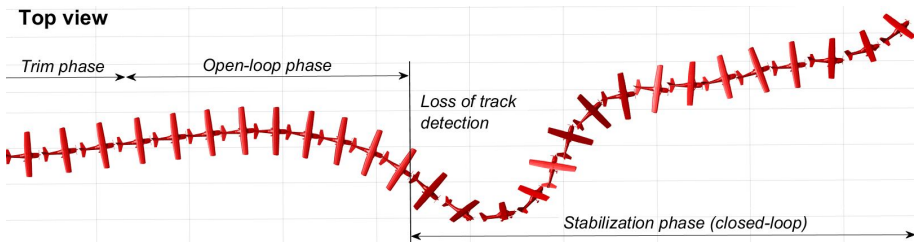


Figure 3.16: [Simulation data] Top view of the aircraft during loss of track caused by the optimized aileron sequence.

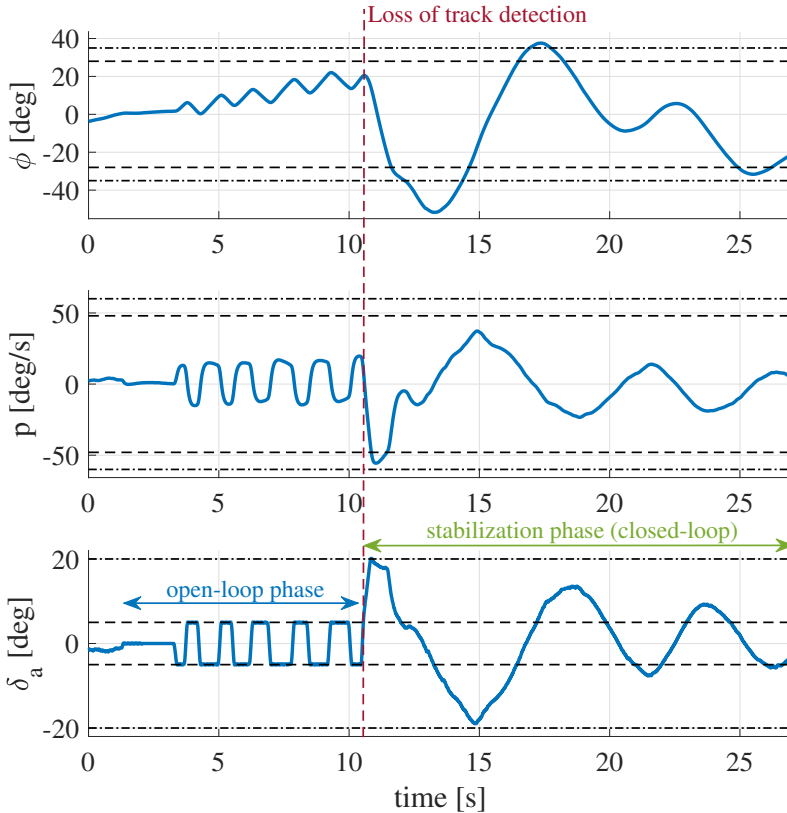


Figure 3.17: **[Simulation data]** Simulated flight test during roll excitation via optimal aileron deflection. The sequence start setting the aircraft at steady state wing-level trim condition; afterwards, the optimal signal input is performed along the roll axis via δ_a . The roll angle ϕ oscillates and move far form the trim condition which causes a deviation from the flight path. At ≈ 11 [s] flight envelope protection triggers and the open-loop sequence stops, recovering the aircraft attitude via feedback controls. In dash lines the OED constraints whereas dash-dot line the flight envelope for ϕ, p and limiters from δ_a .

3.4.10 Experimental data

A real flight test campaign is conducted using the optimized inputs obtained in Section 3.4.6 with trimmed airspeed $V_{T_e} = 20$ m/s. During the experiments, the estimated wind speed was ≈ 2 m/s hence, low process noise caused by turbulences is expected. Each signal input is performed multiple times so has to obtain a trend of the aircraft responses. The data obtained with the experiments are shown in Figures 3.18, 3.19, 3.20 in comparison to the corresponding simulated optimal responses. The control surfaces deflection are omitted since they are already shown in Section 3.4.6. A video that documents the system identification flight test is available at [1]. Because of the difficulties to obtain accurate estimations of the a priori Phugoid mode, the airspeed response exceed the OED constraints of ≈ 3 m/s while the remaining responses in Figure 3.18 are bounded. In Figure 3.19, it is shown that within two of three experiments the roll angle ϕ oscillates and moves towards the flight envelope limits whereas the yaw dynamics, i. e., β and r , are barely excited. Opposite situations occur when the optimal sequence on the rudder control surface is performed, see Figure 3.20. In this case, the roll angle is maintained close to its trim position along the entire open-loop sequence, showing less cross-coupling than predicted. Finally, the sinusoidal motion of the side slip β does not increase in terms of amplitude as observed in simulation. In both lateral excitations the constraints were thoroughly fulfilled.

In Figure 3.21 are collected ten optimal longitudinal response obtained using the same procedure described within this section but for different trimmed airspeed, i. e., $V_{T_e} = 18$ m/s and $V_{T_e} = 25$ m/s. Note that, two experiments relative to the $V_{T_e} = 25$ m/s were aborted due to airspeed limit violation.

In summary, experimental data have shown that optimized maneuvers obtained with the proposed method are able to significantly excite the aircraft dynamics for a relatively long time window without violation of the flight envelope.

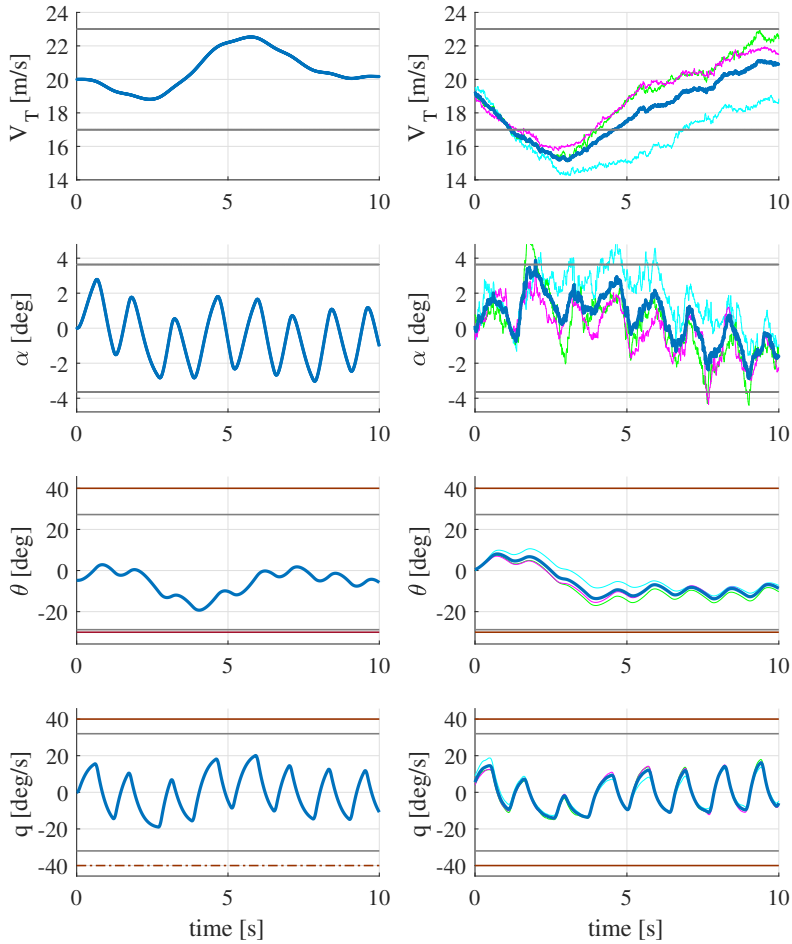


Figure 3.18: Simulated optimal longitudinal response of the a priori model (left column) versus three real experiments (right column). The real experiments are in green, magenta and cyan thin solid lines whereas their average is in thick blue solid line. In grey dash line the OED constraints while dark red dash-dot line the flight envelope.

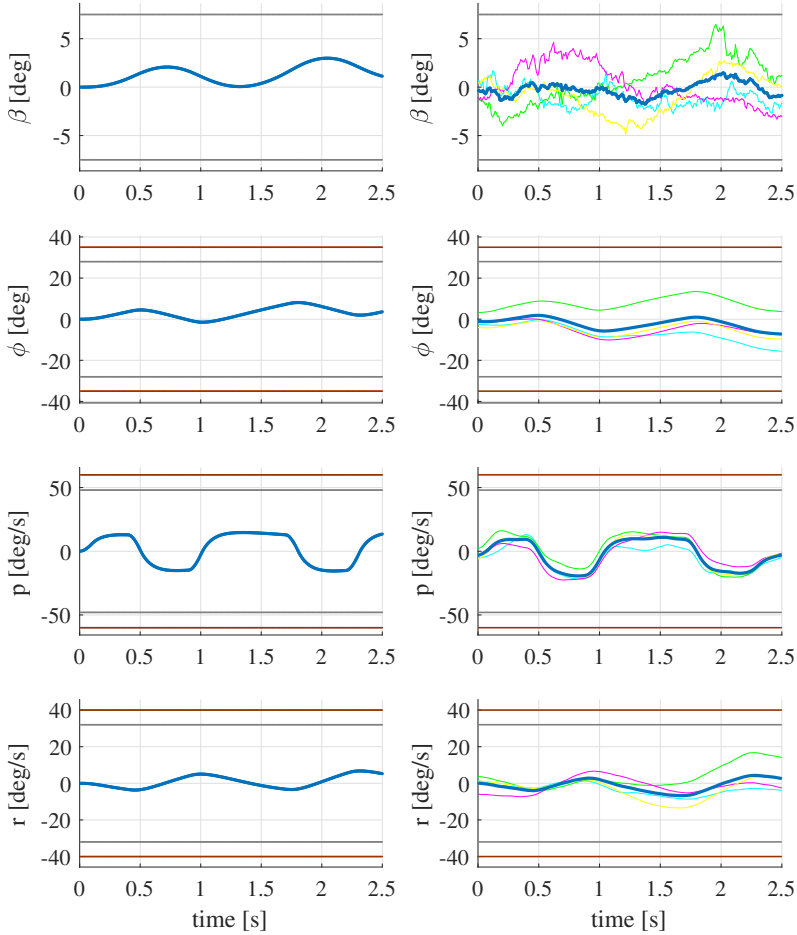


Figure 3.19: Simulated lateral response of the a priori model using optimal aileron deflection (left column) versus three real experiments (right column). The real experiments are in green, magenta and cyan thin solid lines whereas their average is in thick blue solid line. In grey dash line the OED constraints while dark red dash-dot line the flight envelope.

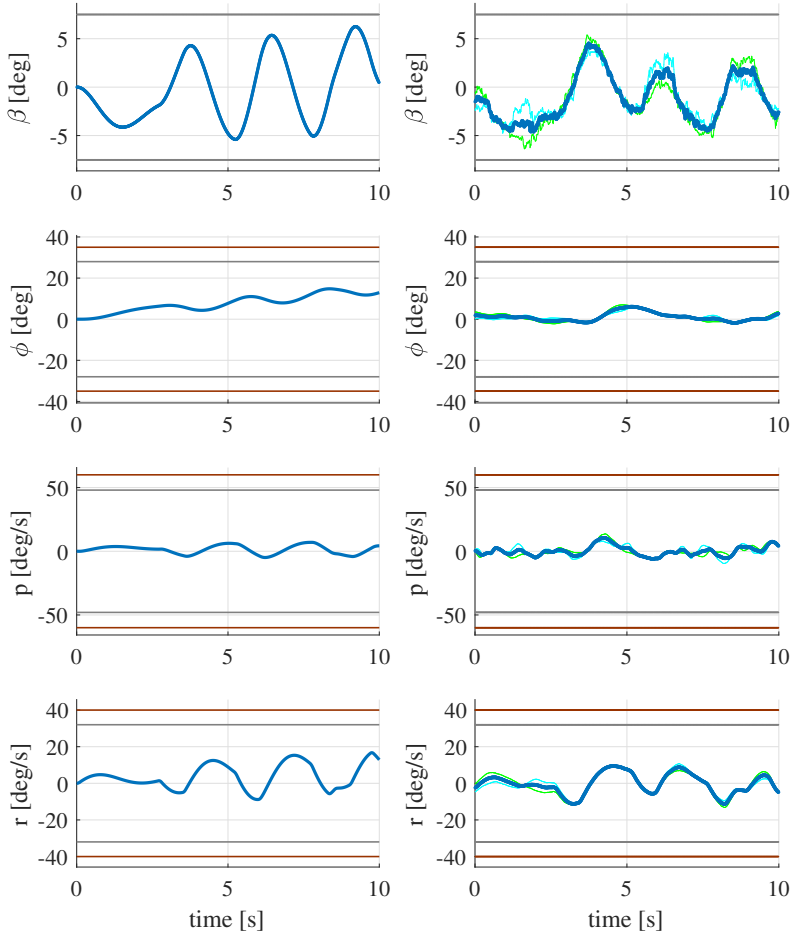


Figure 3.20: Simulated lateral response of the a priori model using optimal rudder deflection (left column) versus two real experiments (right column). The real experiments are in green and cyan thin solid lines whereas their average is in thick blue solid line. In grey dash line the OED constraints while dark red dash-dot line the flight envelope.

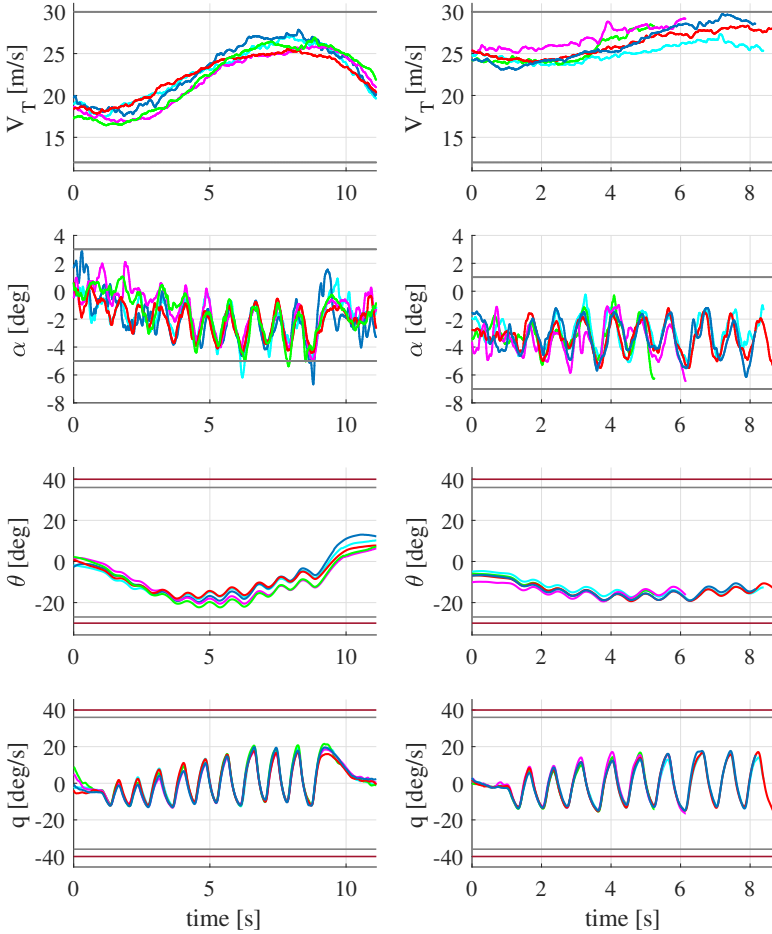


Figure 3.21: **[Experimental data]** Five real optimal longitudinal response for the steady state wing-level flight condition with $V_{T_e} = 18$ m/s (left column) and for $V_{T_e} = 25$ m/s. In grey dash line the OED constraints while dark red dash-dot line the flight envelope.

3.5 Aerodynamic parameter estimation

Once experimental data are available, the aerodynamic derivatives can be extracted using an estimation algorithm. In this section, the longitudinal dynamics is identified via a multiple experiments Model-Based parameter estimation (MBPE) algorithm. First, a guess about the expected parameter's accuracy is obtained from the combined conventional and optimal experiments shown in the previous section. Afterwards, the longitudinal aerodynamic coefficient are extracted from the flight data and estimation results are assessed via a time domain model validation.

3.5.1 Preliminary estimation accuracy analysis

In Section 3.4, the estimation accuracy provided by both the 3-2-1-1 and optimal maneuvers were assessed using the CRLB via the formula in (3.16). Though, experience has shown that a factor of 2 can be introduced in order to obtain an approximation of the parameter standard error [101], resulting in

$$\sigma_i \approx 2 \cdot \text{CRLB}_i = \frac{2}{\sqrt{\mathbf{F}_{ii}}}. \quad (3.17)$$

Therefore, by means of (3.17) one can compute the i^{th} a priori parameter standard error σ_i for a set of experimental data. Table 3.6 gathers the 2CRLB values in percentage for the lumped system responses obtained by the conventional and optimal inputs.

Table 3.6: Dimensional aerodynamic longitudinal derivatives with corresponding expected estimation accuracy via 2CRLB.

Derivatives	Value	2CRLB%
X_V	-0.147	25.27
X_α	7.920	34.88
X_q	-0.163	336.67
X_{δ_e}	-0.232	291.62
Z_V	-0.060	1.07
Z_α/V_{T_e}	-4.400	1.06
Z_q	0.896	1.08
Z_{δ_e}/V_{T_e}	-0.283	4.18
M_α	-7.688	0.14
M_q	-1.963	0.10
M_{δ_e}	-10.668	0.02

The results indicate that the dimensional aerodynamic derivatives relative to the Phugoid mode, i. e., X_q, X_{δ_e} which correspond to the dimensionless one $C_{X_q}, C_{X_{\delta_e}}$ are subject to high uncertainty, despite the conventional experiments were designed sufficiently long. Note that, high values of CRLB indicate that either the i^{th} parameter is physically insignificant with respect to the measured aircraft response or there is a correlation between parameters, i. e., these parameters can vary together, making their individual values difficult to determine [98]. In this case, it turns out that X_V provides a negligible contribution to the aircraft response whereas correlation occurs between X_α, X_q and X_{δ_e} .

To overcome this issue, one might fix the parameters associated to the Phugoid mode with their a priori values, though, errors in the form of a low-frequency model mismatch could arise in the identified model [35]. On the other hand, high estimation accuracy is expected for the Short-period mode which is given by $Z_V, Z_\alpha, Z_q, Z_{\delta_e}, M_\alpha, M_q$ and M_{δ_e} .

3.5.2 Formulation of estimation algorithm

Whenever parameter estimation is intended for identification of aircraft dynamics, multiple experiments are usually required to deal with the following issues [88]:

- Multiple experiments reduce the effects of sensor biases as well as atmospheric turbulence on estimation results;
- individual maneuvers usually have good information content only for a subset of parameters, while multiple maneuvers combined can provide better information w.r.t the complete set of parameters;
- the flight test area and operating safety case restricts the flight paths that can be flown, limiting the available duration of any particular maneuver.

A standard approach is to retrieve the estimated parameters via data fitting for each independent experiment and subsequently weight them w.r.t. their inverse (estimated) parameter covariance matrix $\Sigma_{\mathbf{p}}$ [74]. However, such method might lead to wrong results whenever computed values of $\Sigma_{\mathbf{p}}$ are not reliable [73].

Furthermore, in equation (3.2) one can observe that angular acceleration measurements as well as rate of changes in the airspeed, Euler and aerodynamic angles are required in order to estimate aerodynamic properties. Often, these quantities are not measured, though, they can be retrieved by numerical differentiation methods, which are rather noisy [88]. Consequently, signal distortion may arise, degrading the overall estimation performance. Within this

scenario, multiple experiments MBPE algorithms appear a reasonable choice for estimation of aerodynamic derivatives.

In agreement with the mathematical model defined as in (3.3), a multiple experiments MBPE problem can be first stated using an OCP perspective in continuous time as follows [73]

$$\underset{\mathbf{p}, \mathbf{x}(\cdot)}{\text{minimize}} \quad \sum_{i=1}^{N_e} \int_0^{T^i} \|\hat{\mathbf{y}}^i(t) - \mathbf{h}(\mathbf{x}^i(t), \hat{\mathbf{u}}^i(t), \mathbf{p})\|_{\Sigma_{\mathbf{y}}^{-1}}^2 dt \quad (3.18a)$$

$$\text{subject to} \quad \dot{\mathbf{x}}^i(t) = \mathbf{f}(\mathbf{x}^i(t), \hat{\mathbf{u}}^i(t), \mathbf{p}) \quad t \in [0, T^i], \quad (3.18b)$$

$$t \in [0, T^i], \quad i \in \mathbb{Z}_1^{N_e} \quad (3.18c)$$

with N_e number of experiments, $\hat{\mathbf{u}}^i(t)$ and $\hat{\mathbf{y}}^i(t)$ the input and output measurements respectively, for the i^{th} experiment running for a duration T^i . Using *direct methods* [32], the optimization problem (3.18) can be transformed into a finite dimensional NLP which can then be solved by numerical optimization methods. In this work, a *multiple shooting* approach is chosen due to its stability w.r.t. the initial guess compared to a *single shooting* strategy [22].

In order to implement a multiple shooting algorithm, let us define an equidistant grid over the experiment consisting of the collection of time points t_k , where $t_{k+1} - t_k = \frac{T^i}{N_m^i} := T_s, \forall i = 0, \dots, N_e$ with N_m^i the number of measurements for the i^{th} data set, assuming implicitly that the measurements are collected with a fixed sample time T_s . Additionally, we consider a piecewise constant control parametrization $\mathbf{u}(\tau) = \mathbf{u}_k$ for $\tau \in [t_k, t_{k+1})$. A function $\mathbf{\Pi}(\cdot)$ over each shooting interval is given, which represents a numerical approximation for the solution x_{k+1} of the following IVP

$$\dot{\mathbf{x}}(\tau) = \mathbf{f}(\mathbf{x}(\tau), \mathbf{u}_k, \mathbf{p}, \tau), \quad \tau \in [t_k, t_{k+1}]. \quad (3.19)$$

Within this work, for $\mathbf{\Pi}(\cdot)$ a Runge-Kutta integrator of order 4 (RK4) is implemented. Therefore, the OCP (3.18) can be translated into the following NLP

$$\underset{\mathbf{p}, \mathbf{X}}{\text{minimize}} \quad \sum_{i=1}^{N_e} \sum_{k=0}^{N_m^i} \|\hat{\mathbf{y}}_k^i - \mathbf{h}(\mathbf{x}_k^i, \hat{\mathbf{u}}_k^i, \mathbf{p})\|_{\Sigma_{\mathbf{y}}^{-1}}^2 \quad (3.20a)$$

$$\text{subject to} \quad \mathbf{x}_{k+1}^i - \mathbf{\Pi}(\mathbf{x}_k^i, \hat{\mathbf{u}}_k^i, \mathbf{p}) = 0 \quad (3.20b)$$

$$k = 0, 1, \dots, N_m^i - 1, \quad i \in \mathbb{Z}_1^{N_e} \quad (3.20c)$$

where $\mathbf{X} \in \mathbb{R}^{n_{\mathbf{X}}}$ with $n_{\mathbf{X}} = \sum_{i=1}^{N_e} n_x \cdot N_m^i$ and sorted as

$$\mathbf{X} = [x_0^1, \dots, x_{N_m^1}^1, \dots, x_0^{N_e}, \dots, x_{N_m^{N_e}}^{N_e}]^T \quad (3.21)$$

in order to create a block diagonal structure on the NLP formulation and especially in the equality constraints (3.20b). Notice that in (3.21) the number of measurements N_m are assumed different for each i^{th} experiment.

Finally, the NLP initialization can be chosen from, e.g., previous estimates of \mathbf{p} while \mathbf{X} can be initialized using the measurements $\hat{\mathbf{y}}$ and/or estimates of the state \mathbf{x} . For further details refer to [32, 21].

3.5.3 Data fitting

Within this work, the MBPE algorithm is implemented using CASADi [10] in MATLAB environment. The system dynamics taken into account are the non-linear longitudinal motions expressed in (3.2a), (3.2c), (3.2e), (3.2h) with differential states

$$\mathbf{x}(t) = [V_T(t) \ \alpha(t) \ \theta(t) \ q(t)]^T, \quad (3.22)$$

assuming steady wing-level flight condition, i.e., $\beta = \phi = p = r = 0$. The unknown parameters are

$$\mathbf{p} = \begin{pmatrix} C_{X_0} & C_{X_\alpha} & C_{X_q} & C_{X_{\delta_e}} \\ C_{Z_0} & C_{Z_\alpha} & C_{Z_q} & C_{Z_{\delta_e}} \\ C_{m_0} & C_{m_\alpha} & C_{m_q} & C_{m_{\delta_e}} \end{pmatrix} \in \mathbb{R}^{3 \times 4} \quad (3.23)$$

and control input equal to

$$\mathbf{u}(t) = \delta_e(t), \quad (3.24)$$

whereas the output states are simply given by

$$\mathbf{y}(t) = \mathbf{x}(t) + \epsilon(t). \quad (3.25)$$

The continuous-time optimization problem (3.18) is subsequently discretized and formulated as a NLP using direct multiple shooting. The resulting NLP is solved via IPOPT [104] with linear solver MA27 [56]. Finally, the optimization problem (3.20) is initialized using the baseline model described in Section 3.2.3 for \mathbf{p} and \mathbf{X} with the real output measurements $\hat{\mathbf{y}}^i, i \in \mathbb{Z}_1^{N_e}$.

The data fitting is carried out simultaneously for all experimental data set shown in Section 3.3.5 and Section 3.4.10 with total number of optimization variables

$$n_{\text{opt}} = n_{\mathbf{p}} + n_{\mathbf{X}} = 12 + 35564 = 35576. \quad (3.26)$$

CASADi discovers the structure and computes the full sparse Jacobian and Hessian with a minimum of algorithmic differentiation sweeps (see Figure 3.22).

CASADI's for-loop equivalents are used to efficiently build up the large number of shooting constraints (3.20b). Furthermore, since this application requires a large number of control intervals, the CASADI `map` functionality was used to achieve a memory-lean computational graph. Using this proposed implementation, the NLP is solved within 28 iterations of IPOPT. Figures 3.23, 3.24, 3.25 and 3.26

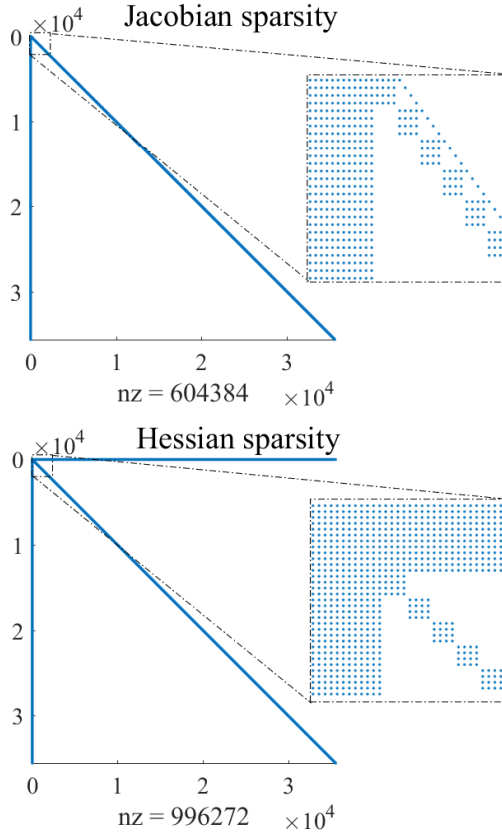


Figure 3.22: Jacobian and Hessian Sparsity of the NLP.

show the data fitting for the airspeed V_T , angle of attack α , pitch angle θ and pitch rate q , respectively.

The overall data fitting is satisfactory except for the airspeed V_T , where biases arise mainly in the conventional experiments.

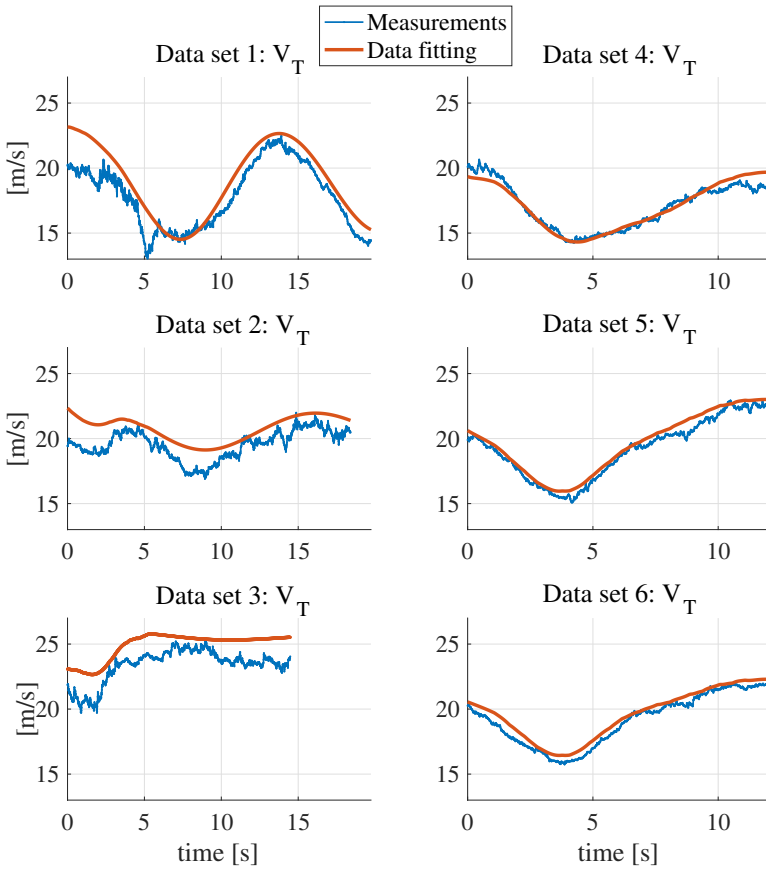


Figure 3.23: [Experimental data] Data fitting for multiple experiments along the longitudinal dynamics for $V_{T_e} = 20\text{m/s}$: airspeed V_T .

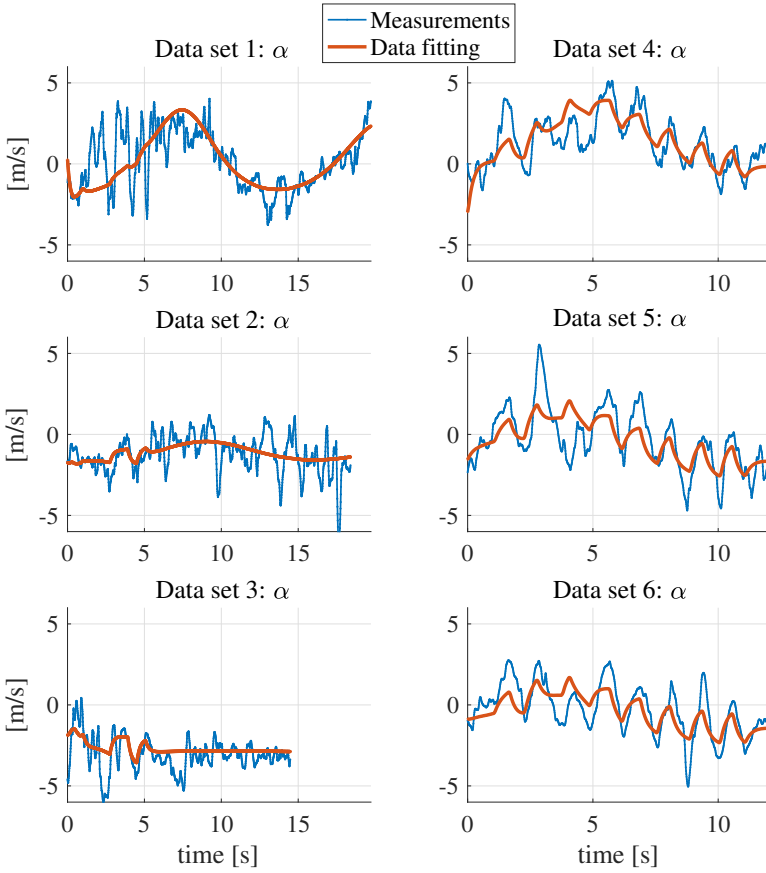


Figure 3.24: **[Experimental data]** Data fitting for multiple experiments along the longitudinal dynamics for $V_{T_e} = 20\text{m/s}$: angle of attack α .

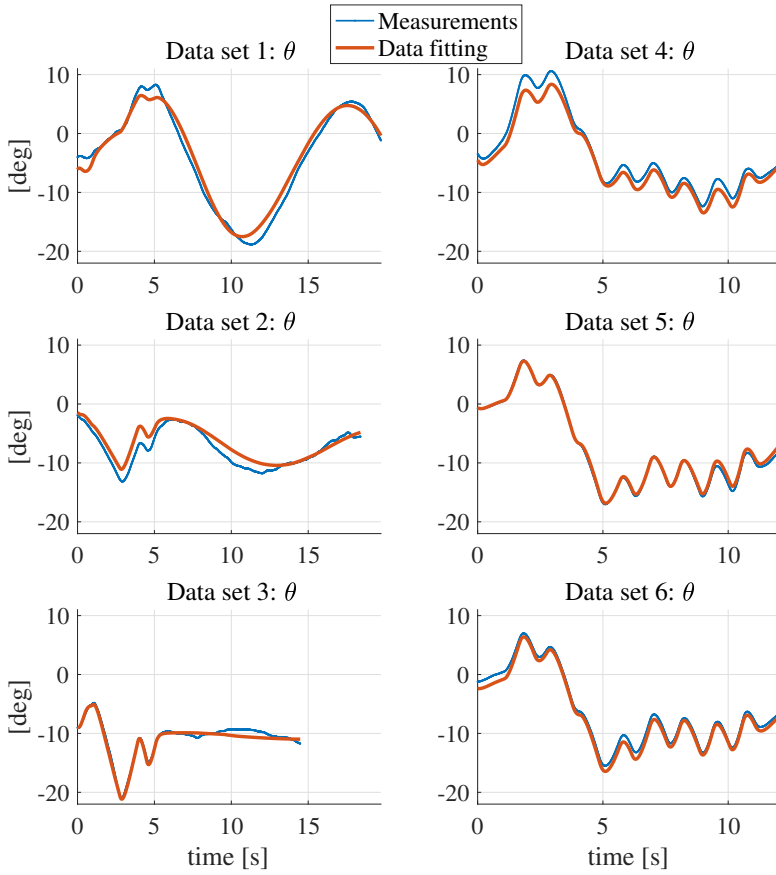


Figure 3.25: **[Experimental data]** Data fitting for multiple experiments along the longitudinal dynamics for $V_{T_e} = 20\text{m/s}$: pitch angle θ .

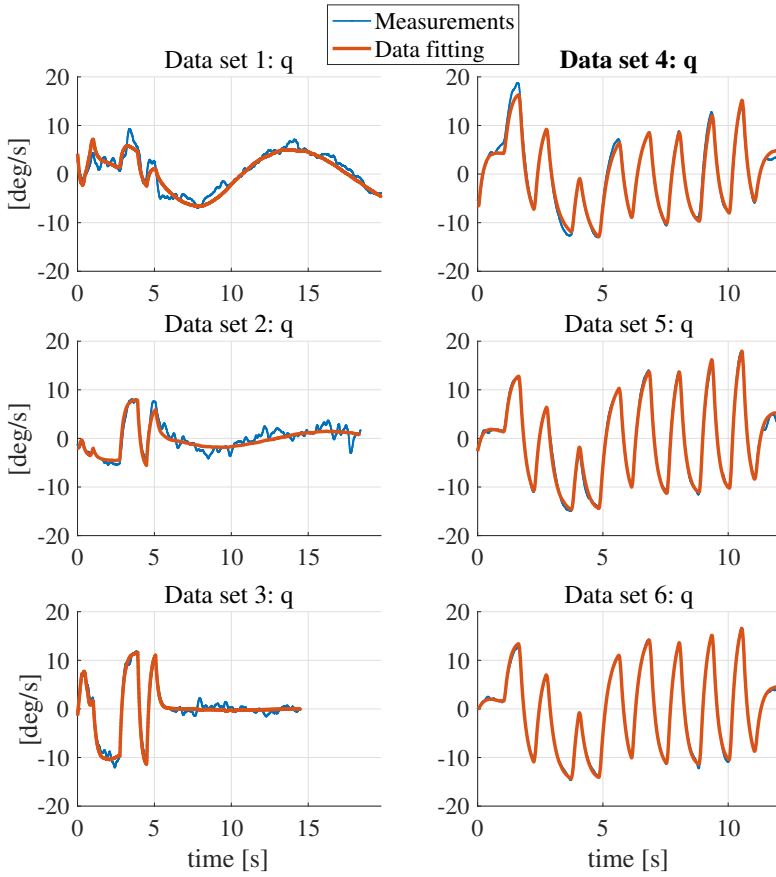


Figure 3.26: **[Experimental data]** Data fitting for multiple experiments along the longitudinal dynamics for $V_{T_e} = 20\text{m/s}$: pitch rate q .

Finally, Table 3.7 collects the estimated dimensionless aerodynamic longitudinal derivatives \mathbf{p}^* for different trimmed airspeeds V_{T_e} . In particular, the remaining derivatives are carried out using five experimental data sets for each flight condition (see Figure 3.21) and using the same methodology described within this work, though, the latter are not shown for the sake of brevity.

Table 3.7: Dimensionless aerodynamic longitudinal derivatives estimates carried out for different trimmed airspeed V_{T_e} .

V_{T_e}	18 m/s	20 m/s	25 m/s
C_{X_0}	-0.060	0.007	-0.168
C_{X_α}	-1.501	-0.705	-0.475
C_{X_q}	-30.202	-20.799	-4.852
$C_{X_{\delta_e}}$	-0.396	-0.952	0.804
C_{Z_0}	-0.478	-0.483	-0.494
C_{Z_α}	-6.728	-5.575	-5.871
C_{Z_q}	-49.209	-55.256	-37.787
$C_{Z_{\delta_e}}$	-1.668	-0.823	-1.145
C_{m_0}	0.060	0.059	0.047
C_{m_α}	-0.737	-0.764	-0.786
C_{m_q}	-18.504	-20.335	-15.911
$C_{m_{\delta_e}}$	-0.966	-0.971	-0.865

3.5.4 Model validation

Because a significant inaccuracy on some derivatives relative to the Phugoid mode are expected (see Section 3.5.1) and biases on the airspeed data fittings are observed in Section 3.5.3, the estimates C_{X_q} , $C_{X_{\delta_e}}$ are set to their a priori values. In this way low frequency errors might arise in the identified model, though, standard feedback controls can easily handle such model mismatch [35].

Furthermore, it turns out that the estimated derivative C_{Z_q} , i.e., the force variation along the Z-axis, has no reasonable physical meaning and for this reason its value is fixed to the a priori estimate, too. However, uncertainties on C_{Z_q} do not significantly deteriorate the predictive capability of the derived model [91].

Table 3.8 collects the a priori \mathbf{p}_{init} and estimated \mathbf{p}^* dimensionless aerodynamic longitudinal derivatives augmented with the set of parameters \mathbf{p}_v which are used for model validation, while Table 3.9 shows the corresponding identified Phugoid and Short-period mode. Also in this case, a discrepancy is observed between

the estimated Phugoid period ($P_o \approx 11$ s) and the observed one ($P_o \approx 13$ s) in the airspeed responses shown in Figure 3.27.

Table 3.8: Collection of the a priori \mathbf{p}_{init} and estimated \mathbf{p}^* dimensionless aerodynamic longitudinal derivatives. \mathbf{p}_v is the set of parameters chosen for model validation.

\mathbf{P}	\mathbf{P}_{init}	\mathbf{P}^*	\mathbf{P}_v
C_{X_0}	-0.033	0.007	0.007
C_{X_α}	0.409	-0.705	-0.705
C_{X_q}	-0.603	-20.799	-0.603
$C_{X_{\delta_e}}$	-0.011	-0.952	-0.011
C_{Z_0}	-0.528	-0.483	-0.483
C_{Z_α}	-4.225	-5.575	-5.575
C_{Z_q}	-7.500	-55.256	-7.500
$C_{Z_{\delta_e}}$	-0.310	-0.823	-0.823
C_{m_0}	-0.031	0.059	0.059
C_{m_α}	-0.607	-0.764	-0.764
C_{m_q}	-11.300	-20.335	-20.335
$C_{m_{\delta_e}}$	-1.420	-0.971	-0.971

Table 3.9: Identified longitudinal modes.

Mode	Short-period	Phugoid	Unit
ω_n	5.548	0.587	rad/s
τ	0.180	1.704	s
δ	0.843	0.036	—
$S\%$	0.721	89.210	%
P_O	2.108	10.712	s

The accuracy of an identified model is ultimately assessed via its capability to predict time responses [35]. For validation purpose, the identified model is simulated using a further flight test experiment shown in Figure 3.28. One can observe that the identified model provides a better fitting compared to the a priori one despite inaccuracies on the Phugoid mode. Figure 3.29 shows the corresponding residual distributions ϵ defined as

$$\epsilon_k = \hat{\mathbf{y}}_k - \mathbf{h}(\mathbf{x}_k, \hat{\mathbf{u}}_k, \mathbf{p}_v), k = 1, \dots, N_v \quad (3.27)$$

with N_v the number of samples related to the validation data set. Practically speaking, the residual is the part of the data that the model is not able to reproduce; the aim is to achieve a residual resembling a white noise signal.

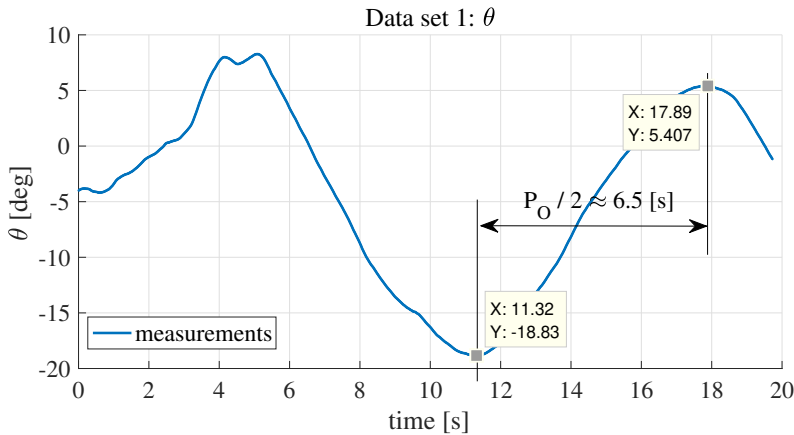


Figure 3.27: **[Experimental data]** Observed Phugoid period of oscillation P_O .

However, it is well-known that the residuals will not be white noise if the real system has significant process noise (atmospheric turbulence) [73].

Finally, estimation results are assessed via the so called Theil Inequality Coefficient (TIC) which is defined by the following relationship [29]

$$\text{TIC} = \frac{\sqrt{\frac{1}{N_v} \sum_{i=1}^{N_v} (\hat{y}_i - \mathbf{h}(\mathbf{x}_i, \hat{\mathbf{u}}_i, \mathbf{p}_v))^2}}{\sqrt{\frac{1}{N_v} \sum_{i=1}^{N_v} \hat{y}_i^2 + \frac{1}{N_v} \sum_{i=1}^{N_v} \mathbf{h}(\mathbf{x}_i, \hat{\mathbf{u}}_i, \mathbf{p}_v)^2}} \quad (3.28)$$

The TIC provides a basis of judgment regarding the degree of predictability of a mathematical (estimated) model via a normalized metric between 0 and 1. A value of $\text{TIC} = 0$ denotes a perfect match whereas $\text{TIC} = 1$ indicates the worst case scenario, i.e., the mathematical model is not able to explain any of the data. Values of $\text{TIC} \leq 0.25$ correspond to accurate prediction for rigid wing aircraft [101, 58]. Table 3.10 summarizes the TIC values for this work. Results shows that the angle of attack α , pitch angle θ are pitch rate q are captured with high accuracy as well as the airspeed response V_T despite the uncertainties mentioned above.

Table 3.10: Theil Inequality Coefficients

	V_T	α	θ	q
TIC	0.04	0.20	0.21	0.15

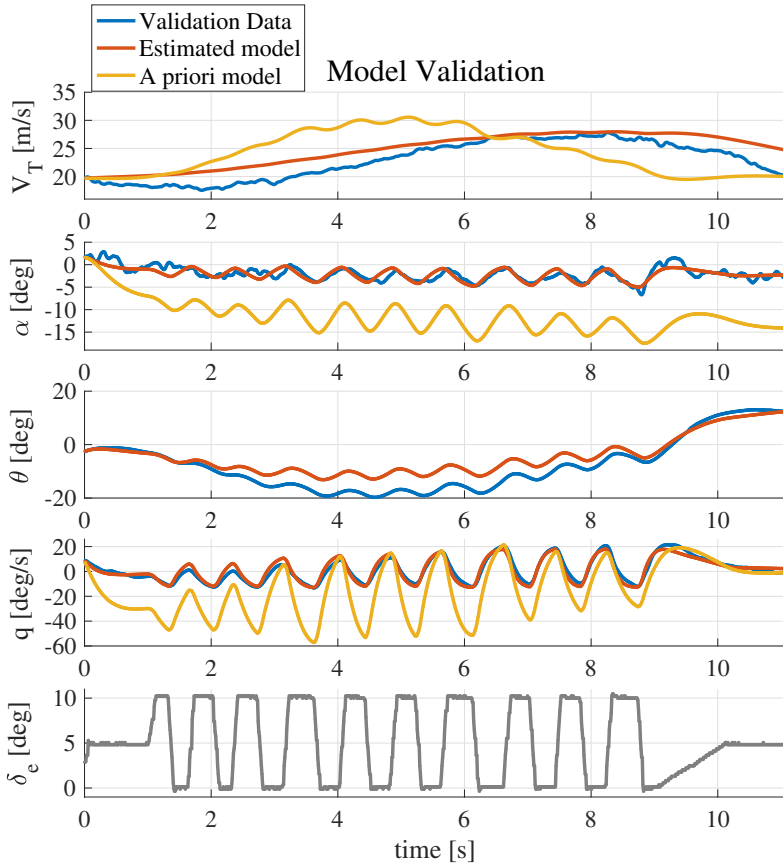


Figure 3.28: **[Experimental data]** Model structure assessment via validation data set. The a priori pitch angle θ response is not shown due to its large deviation w.r.t. the obtained experimental values.

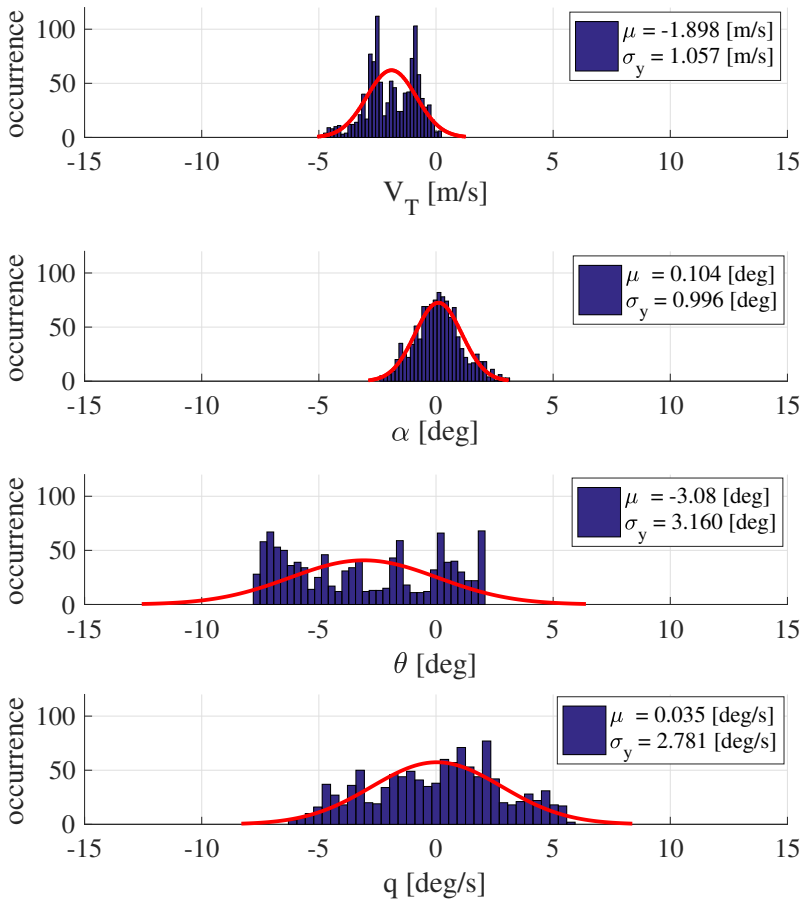


Figure 3.29: **[Experimental data]** Residual distribution analysis for the validation data set with corresponding mean value μ and standard deviation σ .

Chapter 4

Optimization and Analysis of Crosswind Flight Trajectories

Regardless of the system type, the airfoil is required to fly in cyclic patterns to maximize net power produced per cycle. Additionally, AWESs need to be scaled-up in order to be attractive for investments as well as to be competitive compared to conventional wind turbines. However, due to the numerous variables that need to be taken into account simultaneously, the computation of efficient and feasible flight trajectories is not trivial. In many cases, non-optimized flight paths are used as the basis of system sizing and performance prediction, and it is not necessarily obvious how such performance compares with fully optimized trajectories.

In this chapter it is shown how to compute optimized flight trajectories and concurrently to assess the system efficiency prior to manufacturing and flight tests. The proposed method provides an upper bound of expected performance and it relies on the formulation of an Optimal Control Problem (OCP), where the system dynamics are modeled as a set of Differential Algebraic Equations (DAEs). The OCP is implemented using an open-source tool designed to facilitate the formulation OCPs tailored to AWESs. The simulation data are validated against real flight test experiments. Several scenarios are analyzed in terms of control strategy, trajectory topology, trajectory shape, average power output, and for different wind condition. Finally, the power curve of the case study is carried out and its harvesting factor is analyzed.

Outline

The chapter is organized as follows. Section 4.1 formulates an OCP that aims towards the optimization of flight trajectories to maximize the average power output. The mathematical model is described by an index-1 Differential Algebraic Equation (DAE), path and boundary constraints are enforced in agreement with the physical limitation of the case study, and to enforce the periodicity condition, respectively. Within this section, it is also shown how to systematically generate a reasonable initial guess, both using a lemniscate and a circular trajectory, and the open-source tool used to formulate the OCP is briefly introduced. In Section 4.2 the optimal control strategy for a pumping mode AWES is shown and its average power output computed for a specific wind condition. Subsequently, holding patterns that minimize that power consumption during low wind conditions are carried out. Finally, the lemniscate trajectory is compared w.r.t. a circular trajectory in terms of average power output and size, and an hypothetical AWE wind farm configuration is proposed to assess the power density per unit area for both cases. The optimization tool is validated against a set of experimental data in Section 4.3. Within such analysis, the discrepancy between an optimal open-loop solution with a simulated closed-loop solution carried out using the actual FCC designed by Ampyx Power B.V. is quantified. Finally, in Section 4.4 the power curve, Annual Energy Production AEPs and harvesting factor are computed for the case study by solving a sequence of optimal control problems for a range of wind speeds.

4.1 Formulation of an OCP for AWES

In this section, a brief introduction to continuous time OCPs subject to DAEs is provided. Subsequently, an OCP for maximum average power output is formulated for the case study. Finally, it is shown how to efficiently initialize the underlying optimization routine and the software implementation is briefly described.

4.1.1 Overview of continuous time OCPs

In an DAE setting, a continuous time OCP can be stated as follows [33]

$$\underset{\mathbf{x}(\cdot), \mathbf{z}(\cdot), \mathbf{u}(\cdot)}{\text{minimize}} \quad \int_0^T \mathbf{L}(\mathbf{x}(t), \mathbf{z}(t), \mathbf{u}(t)) dt + \mathbf{M}(\mathbf{x}(T), \mathbf{z}(T)) \quad (4.1a)$$

$$\text{subject to} \quad \bar{\mathbf{F}}(\dot{\mathbf{x}}(t), \mathbf{x}(t), \mathbf{z}(t), \mathbf{u}(t)) = 0, \quad t \in [0, T] \quad (4.1b)$$

$$\mathbf{h}(\dot{\mathbf{x}}(t), \mathbf{x}(t), \mathbf{z}(t), \mathbf{u}(t)) \leq 0, \quad t \in [0, T] \quad (4.1c)$$

$$\mathbf{r}(\mathbf{x}(0), \mathbf{x}(T)) = 0 \quad (4.1d)$$

with T the observation time, $\mathbf{L}(\cdot)$ the integrand (*Lagrange*) term and $\mathbf{M}(\cdot)$ the terminal (*Mayer*) cost term. The OCP (4.1) is subject to a system described by a set of fully-implicit DAEs (4.1b), path constraints (4.1c) which bound the system dynamics in agreement with e.g. physical limitations, whereas the boundary constraints (4.1d) embrace either fixed initial values or periodic conditions as well as consistency constraints associated to the DAE formulation.

Within this work, continuous time OCP is addressed via *direct* approaches [19], using *collocation/transcription* techniques [36, 51]. By means of direct methods, (4.1) is approximated via a discretization procedure, and the subsequent numerical solution is given by a large but finite-dimensional, constrained optimization problem [15]. In particular, collocation methods provide a discretized optimal solution for a selected number of *collocation points*, approximating the differential states using interpolating polynomials of order k .

Nowadays, direct collocation techniques are widely implemented for solving OCPs [19], particularly for aerospace applications [18], due to features which allow to [33]

- obtain good numerical stability properties;
- robustly handle path and boundary constraints;
- deal with highly non-linear and/or unstable systems;
- retrieve an highly sparse NLP;
- handle stiff systems due to the *A-stability* property.

In particular, if a *Radau* collocation scheme is implemented [20], the collocation method is additionally *L-stable* i.e. eigenvalues at $-\infty$ can be handled within this framework. As a consequence, transcription methods that implement Radau collocation schemes are best suited for solving OCPs based on DAEs [46]. For this application, a Radau scheme that uses $k = 3$ collocation points is chosen.

4.1.2 Characterization of cost function

The main goal of an AWES is to maximize the average power output using an efficient control strategy while simultaneously delivering feasible flight trajectories in agreement with the system characteristics. By definition, the mechanical average power P_{AV} over a trajectory can be written as

$$P_{AV} = \frac{1}{T} \int_0^T P_m(t) dt \quad (4.2)$$

where in this case the instantaneous mechanical power $P_m(t)$ can be expressed either using the rotational or translational variables, i. e.,

$$P(t) = \dot{E}(t) = \mathbf{f}_{t_\lambda}(t) \cdot \mathbf{v}_l(t) = \mathbf{m}_{t_\lambda}(t) \cdot \boldsymbol{\omega}_d(t). \quad (4.3)$$

If one assumes that for $t = 0$ the harvested energy E is equal to 0, then P_{AV} can be expressed as a Mayer cost term within the OCP (4.1) as follows

$$P_{AV} = \mathbf{M}(\mathbf{x}(T), \mathbf{z}(T)) = \frac{E(T)}{T}. \quad (4.4)$$

In other words, the mechanical average power can be defined as a function of the harvested energy evaluated at the final time T .

Beyond the maximization of the system performance, well designed flight trajectories should preferably avoid aggressive maneuvers, high accelerations that may provide unacceptable mechanical stress on the aircraft, tether damage as well as significant side forces caused by high side slip angles. For these reasons, the Lagrange cost term is formulated as follows

$$\mathbf{L}(\mathbf{x}(t), \mathbf{u}(t)) = \|\mathbf{u}(t)\|_{\Sigma_{\mathbf{u}}^{-1}}^2 + \|\dot{\boldsymbol{\omega}}^{\mathbf{b}}(t)\|_{\Sigma_{\boldsymbol{\omega}}^{-1}}^2 + \sigma_{\beta}^{-1} \beta^2(t) \quad (4.5)$$

with $\Sigma_{\mathbf{u}}^{-1} \in \mathbf{R}^{4 \times 4}$, $\Sigma_{\boldsymbol{\omega}}^{-1} \in \mathbf{R}^{3 \times 3}$, $\sigma_{\beta}^{-1} \in \mathbf{R}$ the weighting matrices associated to the control inputs, aircraft angular accelerations and side slip angle, respectively. Finally, one also aims to harvest the maximum amount of energy within the shortest but feasible time in order to enhance the overall system efficiency. As a consequence, the cycle duration T is considered as an optimization variable within the OCP (4.1).

4.1.3 Characterization of the mathematical model

In Section 2.5 it was shown that the autonomous aircraft is constrained to evolve in the manifold described by the consistency condition $c(\mathbf{x}(t)) = \mathbf{p}^{\mathbf{n}\top} \mathbf{p}^{\mathbf{n}} - l^2 = 0$. As a consequence, the mathematical model of a pumping mode AWES relies on a set of DAEs, more precisely an index-3 DAE.

In order to deploy the obtained mathematical model within an OCP framework, the index-3 DAE was converted into an index-1 DAE via an index reduction procedure. The resulting model derived in Section 2.5 is newly shown below for completeness:

$$\Lambda(\mathbf{x}(t)) \begin{bmatrix} \dot{\mathbf{x}}(t) \\ \mathbf{z}(t) \end{bmatrix} - \mathbf{b}(\mathbf{x}(t), \mathbf{u}(t)) = 0 \quad (4.6)$$

with differential states $\mathbf{x} = [\mathbf{p}^{\mathbf{n}}, \mathbf{v}^{\mathbf{n}}, \mathbf{R}_{\mathbf{nb}}, \omega^{\mathbf{b}}, \delta, l, v_l, E]^\top \in \mathbf{R}^{24}$, control inputs, $\mathbf{u} = [v_{\delta_a}, v_{\delta_e}, v_{\delta_e}, a_l]^\top \in \mathbf{R}^4$ and algebraic variable $\mathbf{z} = \lambda \in \mathbf{R}$, where the matrices $\Lambda(\cdot)$ and $\mathbf{b}(\cdot)$ are equal to

$$\Lambda(\mathbf{x}(t)) = \begin{bmatrix} \mathbf{I}_3 & * & * & * & * & * & * & * & * & * \\ * & m\mathbf{I}_3 & * & * & * & * & * & * & * & \mathbf{p}^{\mathbf{n}} \\ * & * & \mathbf{I}_3 & * & * & * & * & * & * & * \\ * & * & * & \mathbf{J} & * & * & * & * & * & * \\ * & * & * & * & \mathbf{I}_3 & * & * & * & * & * \\ * & * & * & * & * & 1 & * & * & * & * \\ * & * & * & * & * & * & 1 & * & * & * \\ * & * & * & * & * & * & * & 1 & -l\Gamma_d\omega_d & * \\ * & \mathbf{p}^{\mathbf{n}\top} & * & * & * & * & * & * & * & * \end{bmatrix} \quad (4.7)$$

$$\mathbf{b}(\mathbf{x}(t), \mathbf{u}(t)) = \begin{bmatrix} \mathbf{R}_{\mathbf{nb}} \cdot \mathbf{v}^{\mathbf{b}} \\ \mathbf{R}_{\mathbf{nb}} \cdot \left(\mathbf{f}_{t_\lambda}^{\mathbf{b}} + \mathbf{f}_{t_g}^{\mathbf{b}} + \mathbf{f}_{t_a}^{\mathbf{b}} + \mathbf{f}_a^{\mathbf{b}} + \mathbf{f}_g^{\mathbf{b}} \right) \\ \mathbf{R}_{\mathbf{nb}} \cdot \Omega \\ \mathbf{m}_a^{\mathbf{b}} - (\omega^{\mathbf{b}} \times \mathbf{J} \cdot \omega^{\mathbf{b}}) \\ \mathbf{v}_\delta \\ v_l \\ a_l \\ * \\ -\mathbf{v}^{\mathbf{n}\top} \mathbf{v}^{\mathbf{n}} + v_l^2 + la_l \end{bmatrix} \quad (4.8)$$

where * denotes zeros of suitable dimensions. Additionally, in order to obtain a meaningful solution consistency conditions (2.46) (2.56) and (2.4) must be

fulfilled for $t_0 = 0$, i. e. [47, 46, 15]:

$$0 = \mathbf{p}^{\mathbf{n}\top}(0) \mathbf{p}^{\mathbf{n}}(0) - l(0)^2 \quad (4.9a)$$

$$0 = \mathbf{p}^{\mathbf{n}\top}(0) \mathbf{v}^{\mathbf{n}}(0) - l(0) v_l(0) \quad (4.9b)$$

$$0 = \mathbf{R}_{\mathbf{nb}}(0) \cdot \mathbf{R}_{\mathbf{nb}}(0)^\top - \mathbf{I}_3. \quad (4.9c)$$

Finally, the Baumgarte stabilization is used to deal with possible numerical drifts (see Section 2.5.2).

4.1.4 Characterization of path constraints

Path constraints $\mathbf{h}(\cdot)$ (4.1c) play an important role for obtaining meaningful flight trajectories. In agreement with both flight envelope constraints and physical limitations of the system, path constraints must be carefully chosen in order to ensure reasonable prediction capability as well as enforce constraints on states and/or control inputs. Furthermore, one should also aim to obtain flight trajectories which allow the aircraft to operate close to some regime, such that classical industrial controllers can perform well.

For this application, path constraints are chosen in agreement with the following observations:

- Crosswind flight should be performed with high angles of attack α , since the lift generated by the aircraft increases as a function α . However, an upper bound of α is required to prevent *stall phenomenon*. Furthermore, the modeled aerodynamic forces and moments presented in section 2.2.4 are valid only for attached flows, i. e., low angles of attack [37]. Therefore, one should also bound α in a region where the aerodynamic model accuracy is acceptable.
- As mentioned in Section 4.1.2, the side slip angle β must be either bounded or penalized within the cost function to avoid additional drag [91]. Note that, high values of β also involve a non-negligible coupling between the lateral and longitudinal aircraft motions [99], and as a result the complexity relative to the control system architecture would significantly increase.
- The airspeed V_T is bounded in agreement with the flight envelope constraints [72]. It is worth to point out that stall phenomenon may occur at any speed during tethered flights.
- Due to safety issues, the aircraft is constrained to operate above a minimum altitude h_{\min} [71].

- The tether tension f_{t_λ} needs to be upper bounded in order to limit mechanical stress on the aircraft structure and tether severance. A lower bound is also required to avoid tether sag effects that mainly arise during the reel-in phase.
- The Euler angles of roll ϕ and pitch θ need to be limited for safety reasons, to avoid possible collisions between tether and airframe, as well as to simplify the control architecture relative to the aircraft attitude [95].
- Tether length l is constrained in agreement with its maximum length.
- Tether speed v_l as well as tether acceleration a_l are bounded in agreement with the winch characteristics.
- Angular velocity relative to the aircraft $\omega^{\mathbf{b}}$ is constrained according to the flight envelope constraints.
- The pumping cycle time T may be bounded, in this case, analyzing the duration of each loop within real flight tests.

Table A.10 collects both upper and lower bounds used within this chapter.

4.1.5 Characterization of boundary constraints

A generic AWES performs periodic cycles, hence, the boundary constraints $\mathbf{r}(\cdot)$ (4.1d) should contain the periodicity condition $\mathbf{x}(0) = \mathbf{x}(T)$. Additionally, consistency constraints associated to both the algebraic variable λ and the orthonormality condition $\Xi_c(\mathbf{R}_{\mathbf{nb}}(0))$ must be included, too. It turns out that such combination within an OCP framework produces a LICQ deficiency. In short, LICQ is a condition required by the underlying NLP to fulfill the necessary optimality criteria [46] and it is normally caused by redundant constraints. In this case, the orthonormality condition $\Xi_c(\mathbf{R}_{\mathbf{nb}}(0))$ combined with the periodicity constraint $\Xi_p(\mathbf{R}_{\mathbf{nb}}(0), \mathbf{R}_{\mathbf{nb}}(T))$, i. e.,

$$\Xi_c(\mathbf{R}_{\mathbf{nb}}(0)) = \mathbf{R}_{\mathbf{nb}}(0) \cdot \mathbf{R}_{\mathbf{nb}}^\top(0) - \mathbf{I}_3 = 0 \quad (4.10a)$$

$$\Xi_p(\mathbf{R}_{\mathbf{nb}}(0), \mathbf{R}_{\mathbf{nb}}(T)) = \mathbf{R}_{\mathbf{nb}}(0) - \mathbf{R}_{\mathbf{nb}}(T) = 0 \quad (4.10b)$$

deliver LICQ deficiency since nine constraints are enforced (equal to the matrix elements of $\mathbf{R}_{\mathbf{nb}}$) rather than three (the number of degree of freedoms associated to the aircraft attitude). In order to preserve the LICQ condition, one can enforce respectively three and six matrix elements for the periodicity and

orthonormality condition, with specific patterns. According to [47, 110, 46], a suitable combination of boundary constraints relative to (4.10) is given by

$$\tilde{\Xi}_c(\mathbf{R}_{\mathbf{nb}}(0)) = \begin{bmatrix} * & \cdot & \cdot \\ * & * & \cdot \\ * & * & * \end{bmatrix} = 0 \quad (4.11a)$$

$$\tilde{\Xi}_p(\mathbf{R}_{\mathbf{nb}}(0), \mathbf{R}_{\mathbf{nb}}(T)) = \begin{bmatrix} \cdot & * & * \\ \cdot & \cdot & * \\ \cdot & \cdot & \cdot \end{bmatrix} = 0 \quad (4.11b)$$

where * denotes the only matrix elements subject to constraints.

Equations 4.11 are augmented with the additional boundary condition $\tilde{\mathbf{x}}(0) - \tilde{\mathbf{x}}(T) = 0$ where $\tilde{\mathbf{x}}(t)$ is a subset of the state vector $\mathbf{x}(t)$ and equal to

$$\tilde{\mathbf{x}}(t) = [\mathbf{p}^n(t) \quad \mathbf{v}^b(t) \quad \omega^b(t) \quad \delta(t)]^\top \quad (4.12)$$

Finally, in agreement with the Mayer cost term shown in (4.4), the energy state E is set to zero for $t = 0$.

4.1.6 Formulation of an OCP for trajectory optimization

In summary, an OCP tailored for AWES to obtain feasible trajectories which maximize the average mechanical power output can be stated as follows

$$\begin{aligned} & \underset{\mathbf{x}(\cdot), \mathbf{z}(\cdot), \mathbf{u}(\cdot), T}{\text{minimize}} && \int_0^T \left(\|\mathbf{u}(t)\|_{\Sigma_{\mathbf{u}}^{-1}}^2 + \|\dot{\omega}^{\mathbf{b}}(t)\|_{\Sigma_{\omega}^{-1}}^2 + \sigma_{\beta}^{-1} \beta^2(t) \right) dt - \frac{E(T)}{T} \\ & && (4.13a) \end{aligned}$$

$$\text{subject to} \quad \mathbf{\Lambda}(\mathbf{x}(t)) \begin{bmatrix} \mathbf{x}(t) \\ \mathbf{z}(t) \end{bmatrix} - \mathbf{b}(\mathbf{x}(t), \mathbf{u}(t)) = 0, t \in [0, T] \quad (4.13b)$$

$$h(t) \geq h_{\min}, \quad t \in [0, T] \quad (4.13c)$$

$$\alpha_{\min} \leq \alpha(t) \leq \alpha_{\max}, \quad t \in [0, T] \quad (4.13d)$$

$$V_{T_{\min}} \leq V_T(t) \leq V_{T_{\max}}, \quad t \in [0, T] \quad (4.13e)$$

$$f_{t_{\min}} \leq f_{t_{\lambda}}(t) \leq f_{t_{\max}}, \quad t \in [0, T] \quad (4.13f)$$

$$\phi_{\min} \leq \phi(t) \leq \phi_{\max}, \quad t \in [0, T] \quad (4.13g)$$

$$\theta_{\min} \leq \theta(t) \leq \theta_{\max}, \quad t \in [0, T] \quad (4.13h)$$

$$l_{\min} \leq l(t) \leq l_{\max}, \quad t \in [0, T] \quad (4.13i)$$

$$v_{l_{\min}} \leq v_l(t) \leq v_{l_{\max}}, \quad t \in [0, T] \quad (4.13j)$$

$$a_{l_{\min}} \leq a_l(t) \leq a_{l_{\max}}, \quad t \in [0, T] \quad (4.13k)$$

$$\omega^{\mathbf{b}}_{\min} \leq \omega^{\mathbf{b}}(t) \leq \omega^{\mathbf{b}}_{\max}, \quad t \in [0, T] \quad (4.13l)$$

$$\delta_{\min} \leq \delta(t) \leq \delta_{\max}, \quad t \in [0, T] \quad (4.13m)$$

$$v_{\delta_{\min}} \leq v_{\delta}(t) \leq v_{\delta_{\max}}, \quad t \in [0, T] \quad (4.13n)$$

$$\tilde{\mathbf{x}}(0) - \tilde{\mathbf{x}}(T) = 0, \quad (4.13o)$$

$$\tilde{\Xi}_{\mathbf{p}}(\mathbf{R}_{\mathbf{nb}}(0), \mathbf{R}_{\mathbf{nb}}(T)) = 0, \quad (4.13p)$$

$$c(\mathbf{x}(0)) = 0, \dot{c}(\mathbf{x}(0)) = 0, \quad (4.13q)$$

$$\tilde{\Xi}_{\mathbf{c}}(\mathbf{R}_{\mathbf{nb}}(0)) = 0, E(0) = 0. \quad (4.13r)$$

where (4.13b) denotes the mathematical model described as an index-1 DAE and shown in (2.60). The inequalities from (4.13c) to (4.13n) correspond to the path constraints described in Section 4.1.4. Boundary constraints are characterized by the periodicity conditions (4.13o) and (4.13p). Finally, the consistency constraints are described by (4.13q) and (4.13r).

4.1.7 Algorithm initialization

Flight trajectory optimization of a rigid wing pumping mode AWES involve a strongly non-convex OCP due to the nonlinear and coupled dynamics yield by the mathematical model. As a consequence, the OCP (4.13) needs to be carefully initialized with a suitable initial guess.

One way to obtain an initial guess is either by numerical simulation using a complex hierarchical control system as in [95] or by experimental data, though, both approaches are rather time consuming and costly. A much more efficient way that allows to systematically generate a reasonable initial guess is via an *homotopy strategy* [54, 48].

An homotopy procedure aims towards the formulation of a relaxed OCP to obtain an optimal solution which can be used as initialization for (4.13). In this case, the main nonlinearity contained in the dynamic equations (2.60) is provided by the body forces and moments, hence, one can significantly relax the overall problem by replacing them with augmented forces $\mathbf{f}_{\text{aug}}^{\text{b}}$ and moments $\mathbf{m}_{\text{aug}}^{\text{b}}$ that are equal to

$$\begin{bmatrix} \mathbf{f}_{\text{aug}}^{\text{b}} \\ \mathbf{m}_{\text{aug}}^{\text{b}} \end{bmatrix} = \zeta \begin{bmatrix} \mathbf{f}_{\text{t}}^{\text{b}} + \mathbf{f}_{\text{a}}^{\text{b}} + \mathbf{f}_{\text{g}}^{\text{b}} \\ \mathbf{m}_{\text{a}}^{\text{b}} \end{bmatrix} + (1 - \zeta) \begin{bmatrix} \mathbf{f}_{\text{p}}^{\text{b}} \\ \mathbf{m}_{\text{p}}^{\text{b}} \end{bmatrix} \quad (4.14)$$

where $\mathbf{f}_{\text{p}}^{\text{b}} \in \mathbf{R}^{3 \times 1}$, $\mathbf{m}_{\text{p}}^{\text{b}} \in \mathbf{R}^{3 \times 1}$ correspond to the *pseudo* forces and moments, whereas $\zeta \in \mathbf{R}$ denotes the *homotopy parameter*.

Subsequently, one needs to formulate a new OCP that resembles (4.13), though, based on a mathematical model with augmented forces and moments as in (4.14), Mayer term $\mathbf{M}(\cdot)$ equal to zero and Lagrange term \mathbf{L} equal to

$$\mathbf{L}(\mathbf{p}^{\text{n}}, \mathbf{f}_{\text{p}}^{\text{b}}, \mathbf{m}_{\text{p}}^{\text{b}}) = \|\mathbf{p}^{\text{n}}(t) - \mathbf{p}_{\text{ref}}^{\text{n}}(t)\|^2 + \|\mathbf{f}_{\text{p}}^{\text{b}}\|^2 + \|\mathbf{m}_{\text{p}}^{\text{b}}\|^2. \quad (4.15)$$

Starting from the fully relaxed problem ($\zeta = 0$), the modified OCP can be initialized even with a poor initial guess. Within this work, two common types of trajectories are taken into account: lemniscate and circular trajectories.

A *pseudo-code* for initial trajectories generation is provided in Algorithm 1. The routine requires as inputs the number of discretization intervals N , duration T and trajectory topology (*'lemniscate'* or *'circular'*), while the corresponding

outputs are the initial position \mathbf{p}^n , translational velocity \mathbf{v}^n (both in NED frame) and DCM \mathbf{R}_{nb} .

Exemplary, Figure 4.1 shows the initial trajectory generated by the routine based on Algorithm 1 with $N = 60$, $T = 44$ s and trajectory = 'lemniscate'. The homotopy procedure is then applied, where the parameter ζ is gradually increased so that for $\zeta = 1$ only the original forces and moments are contained in the system dynamics.

Algorithm 1 Algorithm Initialization

```

function [ $\mathbf{p}^n, \mathbf{v}^n, \mathbf{R}_{nb}$ ] = INITIALIZEOCP(N, T, trajectory)
  Let  $\mathbf{p}^n[1 \dots N], \mathbf{v}^n[1 \dots N], \mathbf{R}_{nb}[1 \dots N]$  be new arrays
   $r_t = 300$  ▷ lemniscate/circle radius [m]
   $l_{max} = 450$  ▷ maximum length between winch and trajectory [m]
   $h_{min} = 100$  ▷ minimum altitude [m]
   $l_c = \sqrt{l_{max}^2 - r_t^2}$  ▷ length between winch and center of trajectory [m]
   $\Theta = \arcsin(r_t/l_{max}) + \arcsin(h_{min}/l_{max})$  ▷ elevation angle [rad]
   $\mathbf{R}_y = \begin{bmatrix} \cos \Theta & 0 & \sin \Theta \\ 0 & 1 & 0 \\ -\sin \Theta & 0 & \cos \Theta \end{bmatrix}$ 
  for  $k = 1$  to  $N + 1$  do
    parameter =  $(k - 1)/N$ 
     $\Psi = (2\pi \cdot \text{parameter} - \pi)$ 
     $\dot{\Psi} = 2\pi/T$ 
    if trajectory = 'lemniscate' then
       $\mathbf{p}^n[k] = \mathbf{R}_y \cdot [l_c \quad r_t \cdot \sin(\Psi) \quad -(r_t/2) \cdot \sin(2\Psi)]^\top$ 
       $\mathbf{v}^n[k] = \mathbf{R}_y \cdot [0 \quad r_t \cdot \cos(\Psi) \cdot \dot{\Psi} \quad -r_t \cos(2\Psi) \cdot \dot{\Psi}]^\top$ 
    else if trajectory = 'circular' then
       $\mathbf{p}^n[k] = \mathbf{R}_y \cdot [l_c \quad (r_t/2) \cdot \sin(\Psi) \quad (r_t/2) \cdot \cos(\Psi)]^\top$ 
       $\mathbf{v}^n[k] = \mathbf{R}_y \cdot [0 \quad (r_t/2) \cdot \cos(\Psi) \cdot \dot{\Psi} \quad -(r_t/2) \cdot \sin(\Psi) \cdot \dot{\Psi}]^\top$ 
    end if
     $\mathbf{e}_x[k] = \mathbf{v}^n / \|\mathbf{v}^n\|$  ▷ aircraft body x-axis
     $\mathbf{e}_z[k] = -\mathbf{p}^n / \|\mathbf{p}^n\|$  ▷ aircraft body z-axis
     $\mathbf{e}_y[k] = \mathbf{e}_z \times \mathbf{e}_x$  ▷ aircraft body y-axis
     $\mathbf{R}_{nb}[k] = [\mathbf{e}_x, \mathbf{e}_y, \mathbf{e}_z]$  ▷ Build DCM
  end for
end function

```

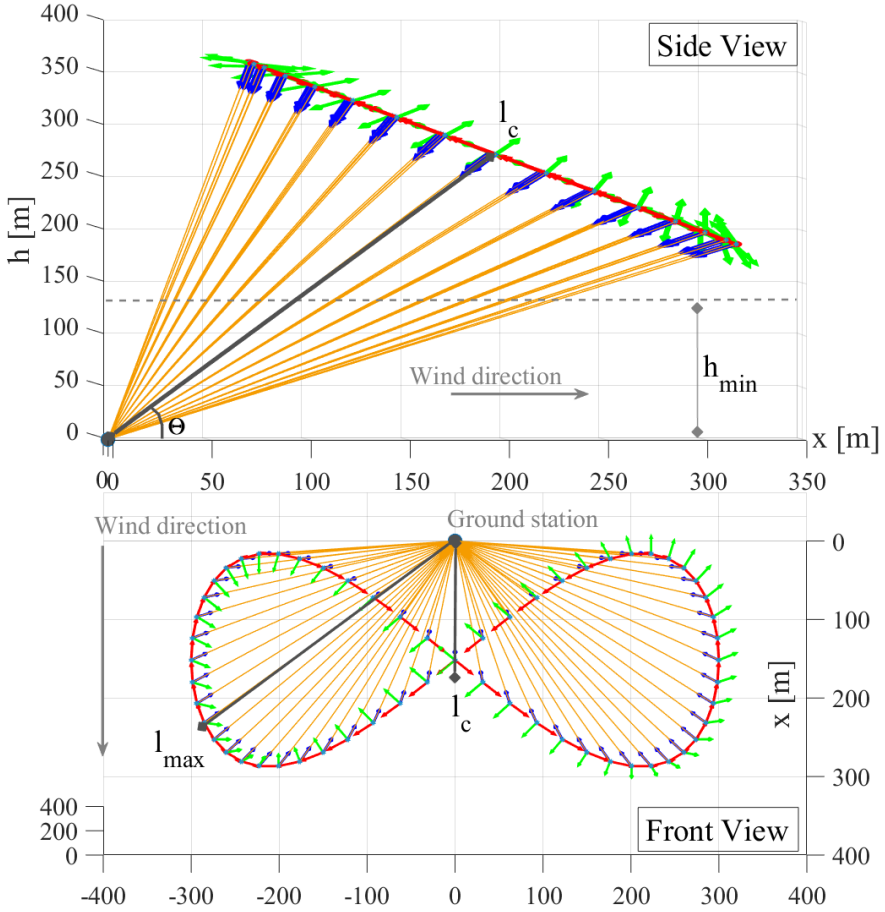


Figure 4.1: Initial trajectory generated by the Algorithm 1 with $N = 60$, $T = 44$ and trajectory = 'lemniscate'.

4.1.8 Algorithm implementation

Within this work, the OCPs are computed using OPENAWE [62], an open-source tool for the Matlab/Octave Environment. OpenAWE is implemented using object oriented programming and it contains a library for modeling components of a typical AWES such as aircraft, winch, and tether. More precisely, two types of tether models are provided: a straight-line tether for flight trajectory optimizations and a static tether approximation that is capable of representing the tether shape, e.g., for launch and landing trajectory optimizations [66]. OPENAWE is built upon an open-source optimal control library named OPENOCL [63] and based on CASADI [10]. In short, the continuous-time optimization problem is discretized and formulated as a NLP automatically by OPENOCL using direct collocation techniques [20]. The resulting NLP is subsequently solved by IPOPT [104] with linear solver MA27 [56]. In [64] it is possible to find a simplified, non-confidential version of the proposed work based on the case study.

4.2 Flight trajectory analysis

Within this section, an optimal control strategy with the corresponding flight trajectory is shown for nominal wind conditions. Further, a reverse pumping strategy which minimizes the power output via holding pattern during low wind conditions are obtained. The lemniscate trajectory is subsequently compared to a circular trajectory in terms of control strategy, average power output, and trajectory size.

4.2.1 Optimal control strategy

The OCP (4.13) is initialized using the homotopy strategy described in Section 4.1.7 with the initial guess shown in Figure 4.1. A wind speed measured at the anemometer height h_a equal to $w_{h_a} = 8$ m/s and northern wind direction is assumed. The obtained optimal control strategy for a rigid wing pumping mode AWES is depicted in Figures 4.3, 4.2, 4.4, 4.5. As expected, an optimal control strategy suggests to perform crosswind flight with high angle of attack α , high airspeed V_T and maximum (allowable) roll angle ϕ . As a result, the lift generated by the aircraft causes a high tension which is used to unroll the tether with speed v_l . The corresponding winch angular speed $\omega_d = \frac{v_l}{r_d}$ and torque m_λ produce a certain amount of mechanical power P_m that is subsequently converted to electrical power P_e by the generator.

The reel-in (power consumption) phase arises between ≈ 11 s and ≈ 25 s (see left corner of Figure 4.3). During this phase, the angle of attack decreases simultaneously with the pitch angle and airspeed, while the tether tension drops and the aircraft climbs up to a predefined altitude h . Simultaneously, the winch rolls up the tether with low tension (hence low power consumption) and maximum angular speed. Afterwards, a new reel-out (power production) phase occurs by a fast change in the pitch angle.

Note that a further reel-in phase occurs also between ≈ 35 s and ≈ 40 s which corresponds to the right corner of the flight trajectory. After the power production phase, the aircraft must regain altitude, but the kinetic energy is not sufficient to restore the desired altitude, due to dissipative effects coming from aerodynamic drag of both tether and aircraft. As a consequence, during the climbing phase the aircraft slows down and the winch is prone to perform an additional reel-in phase to prevent loss of airspeed of the aircraft. Such behavior has also been experienced within real crosswind flight tests as described in [95].

Along the entire trajectory the angle of side slip β is kept close to zero as required. Ultimately, assuming that the case study adopts the control strategy described above, the expected average power output P_{AV} is roughly 4.6 kW.

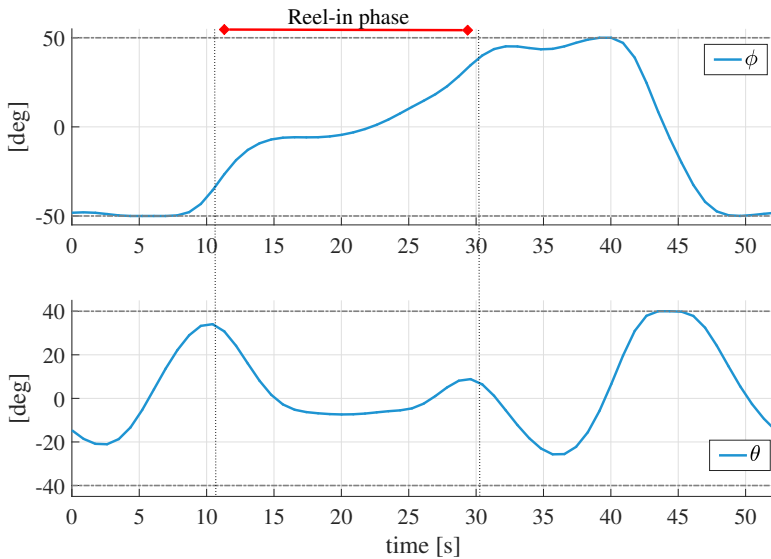


Figure 4.2: Optimal solution relative to the angle of roll ϕ and pitch θ for a rigid wing pumping mode AWES. Path constraints are shown in dash dot grey line.

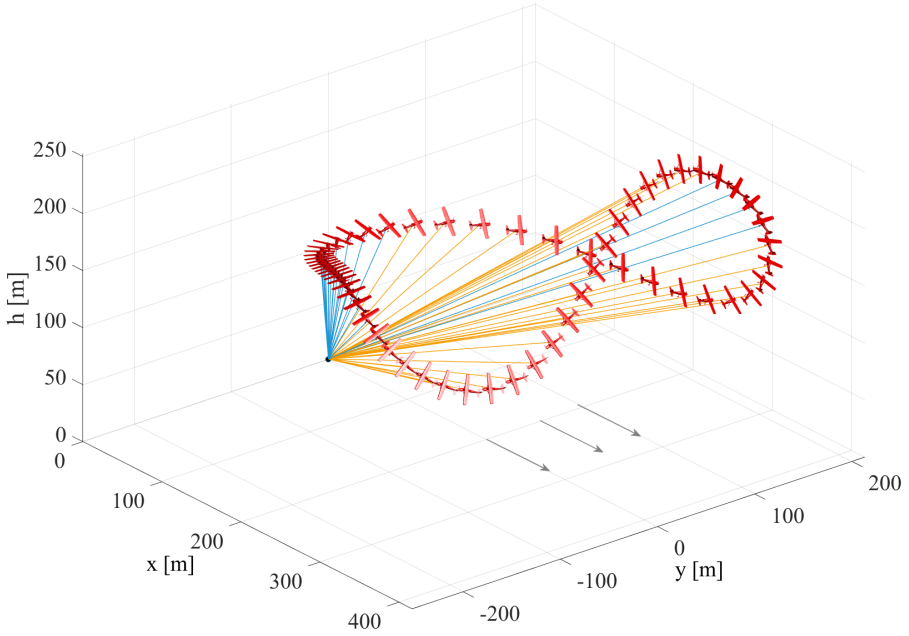


Figure 4.3: Optimal trajectory for a rigid wing pumping mode AWES in 3D (lemniscate pattern). The blue tether corresponds to the reel-in (power consumption) phase, while the orange tether denotes the reel-out (power production) phase. The main reel-in phase arises in the left corner, though, a further reel-in phase occurs in the right corner so as to prevent the loss of airspeed of the airborne component.

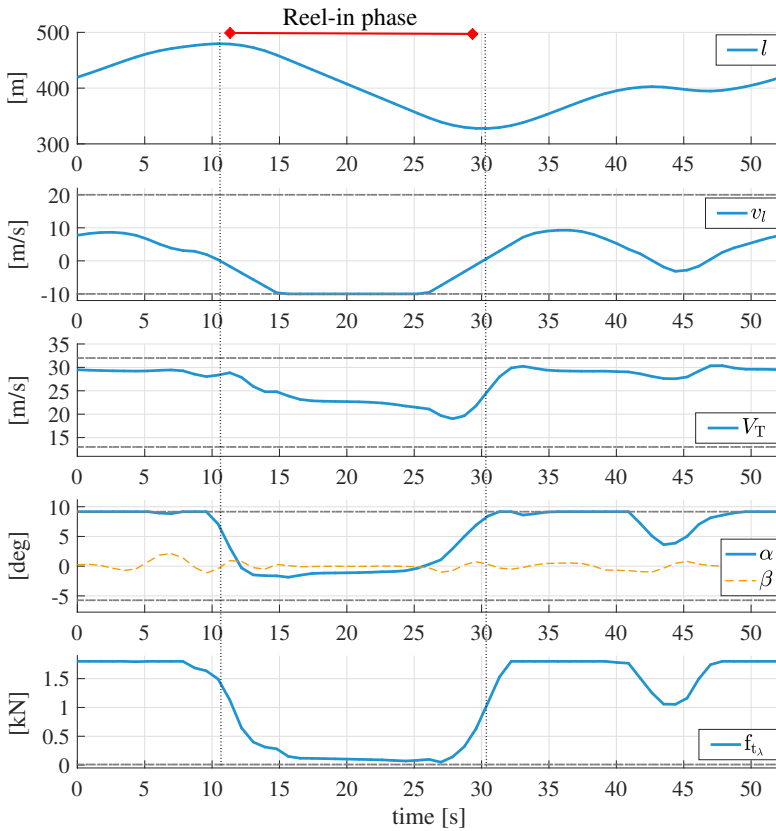


Figure 4.4: Optimal solution relative to tether length l , tether speed v_l , airspeed V_T , angle of attack α , angle of side slip β and tether tension f_{t_λ} for a rigid wing pumping mode AWES. Path constraints are shown in dash dot grey line.

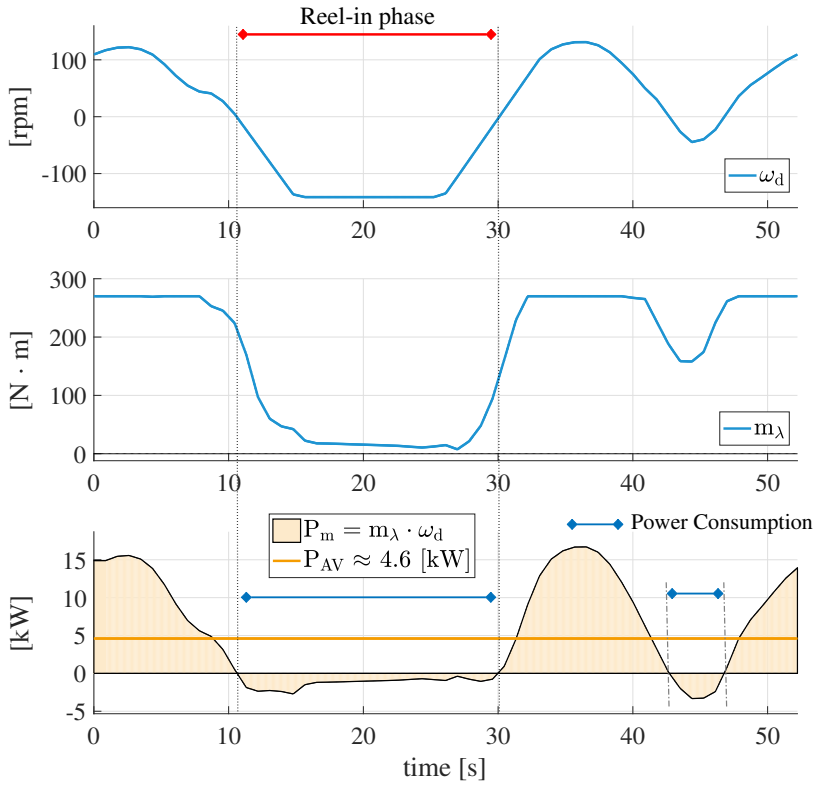


Figure 4.5: Optimal solution relative to the winch angular speed ω_d , torque m_λ , instantaneous mechanical power P_m with corresponding averaged value P_{AV} for a rigid wing pumping mode AWES. Under optimal conditions, the expected average power output P_{AV} is roughly 4.6 kW

4.2.2 Reverse pumping mode

AWES are designed to operate within a large range of weather conditions, though, whenever the wind speed approaches zero the amount of energy consumed during the reel-in phase might exceed the amount of energy generated during the reel-out phase. One might then prefer to land until favorable wind conditions occur. However, launching and landing techniques for a tethered aircraft require sophisticated and expensive startup methodology, e. g., rotating arm mechanisms as described in [41]. Launch and landing mechanisms such as a pneumatic catapult are also investigated by Ampyx Power B.V. and shown in [7].

Alternatively, one can design a suitable control strategy that minimizes the power consumption during low wind conditions by means of holding trajectories. Such control strategy can be easily retrieved by solving the OCP (4.13) under the assumption of w_{ha} sufficiently close to zero. The obtained flight trajectory with $w_{ha} = 0.1$ m/s is depicted in Figure 4.7, whereas the corresponding control strategy is shown in Figure 4.6.

One can observe that the winch inserts kinetic energy into the system by pulling the tether to keep the aircraft aloft. In order to minimize the tether drag, the flight trajectory converges at the minimum allowable altitude ($h_{min} = 100$ m) above the winch. Simultaneously, the aircraft glides constantly at high angle of attack so that a certain amount of lift is always produced, whereas the airspeed increases when the tether is pulled by the winch. The gained kinetic energy is then converted into potential energy in a cyclical way. Such periodical cycle with a negative net energy is known in the literature as *reverse pumping* mode [44]. For this simulation, results shows that the case study consumes in average $P_{AV} \approx 760$ W to keep the aircraft airborne via an optimal holding trajectory.

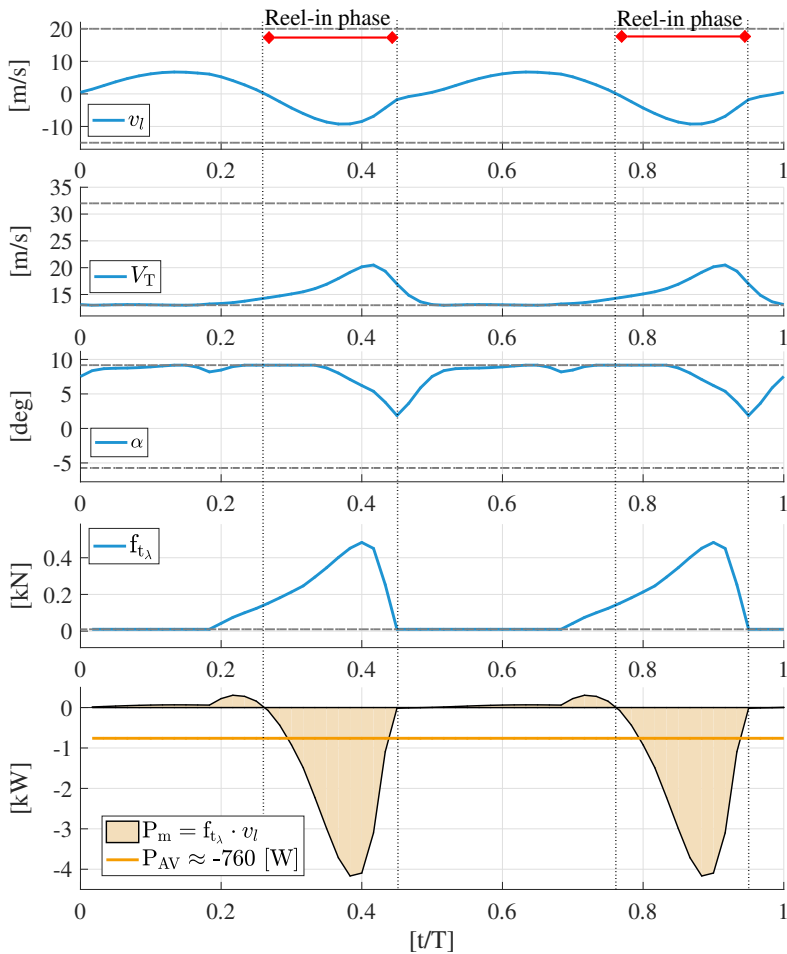


Figure 4.6: Optimal solution relative to tether speed v_l , airspeed V_T , angle of attack α , angle of side slip β and tether tension f_{t_λ} and mechanical power P_m for low wind conditions. Path constraints are shown in dash dot grey line.

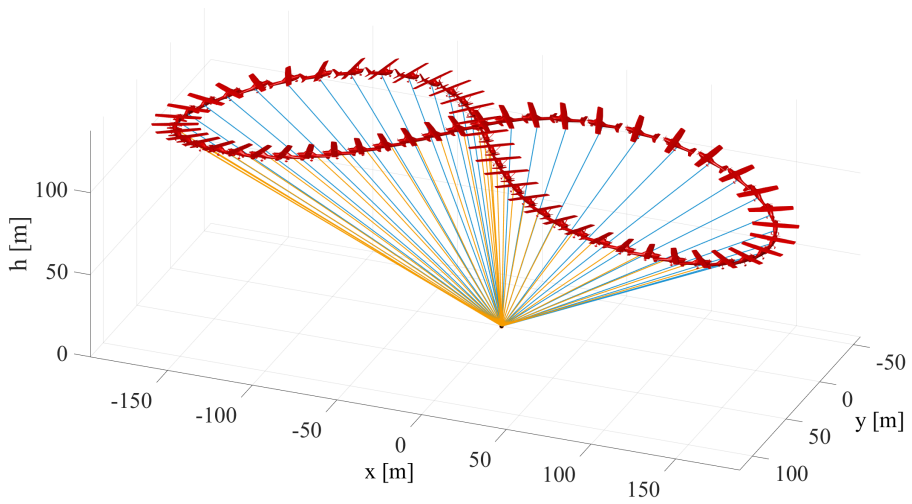


Figure 4.7: Optimal holding pattern in 3D for low wind conditions. The blue tether corresponds to the reel-in (power consumption) phase, while the orange tether denotes the reel-out (power production) phase.

4.2.3 Lemniscate versus circular optimal trajectory

In the AWE field, two common trajectory typologies are considered: lemniscate and circular trajectory. On the one hand, a circular trajectory is often preferred in practice for its simplicity, though, the winch must be equipped with a swivel mechanism in order to avoid tether winding issues. On the other hand, a lemniscate trajectory avoids swivel mechanisms, though, the aircraft might be subject to high angular accelerations [48]. In this subsection, lemniscate and circular optimal trajectory are compared in terms of average power output and size.

Since a common goal for an AWES is the maximization of the average power output P_{AV} , one may wonder if P_{AV} is sensitive to the trajectory topology, in other words if a trajectory can deliver a higher P_{AV} when using a different topology. For this purpose, let us solve the OCP in (4.13) with boundary conditions equal to Section 4.2.1, but using a circular trajectory as initial guess (see Section 4.1.7). The obtained optimal circular trajectory for the case study is depicted in Figure 4.10. Despite the difference in terms of topology, both trajectories exhibit the same control strategy that is described in Section 4.2.1. Furthermore, in both cases the average power output P_{AV} is close to 4.5kW, as shown in Figure 4.8. Therefore, under the assumption of equal boundary conditions, a rigid wing pumping mode AWES harvests the same amount of energy over the time T regardless of the topology of the flight trajectory.

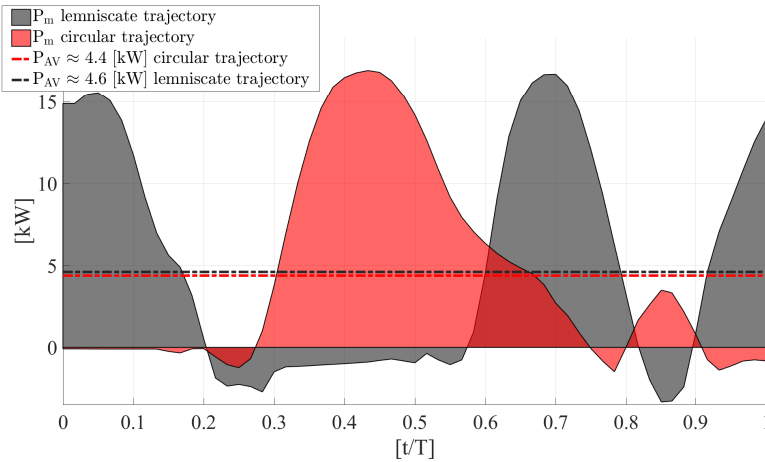


Figure 4.8: Average power outputs comparison with normalized time between lemniscate and circular trajectory.

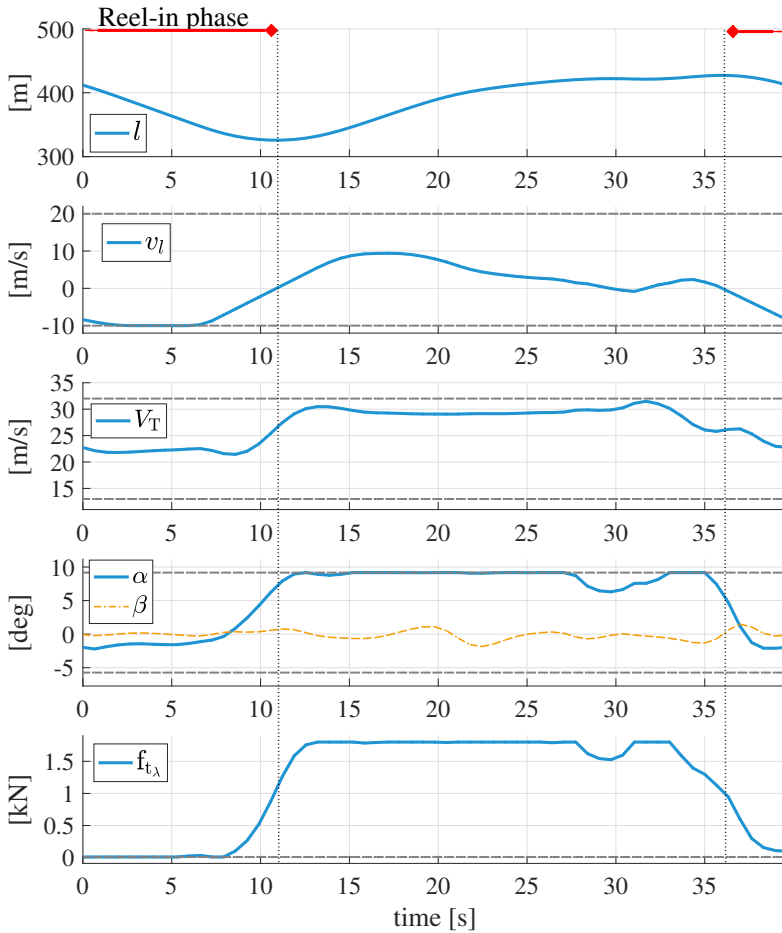


Figure 4.9: Optimal solution relative to tether length l , tether speed v_l , airspeed V_T , angle of attack α , angle of side slip β and tether tension f_{t_λ} for a circular flight trajectory. Path constraints are shown in dash dot grey line.

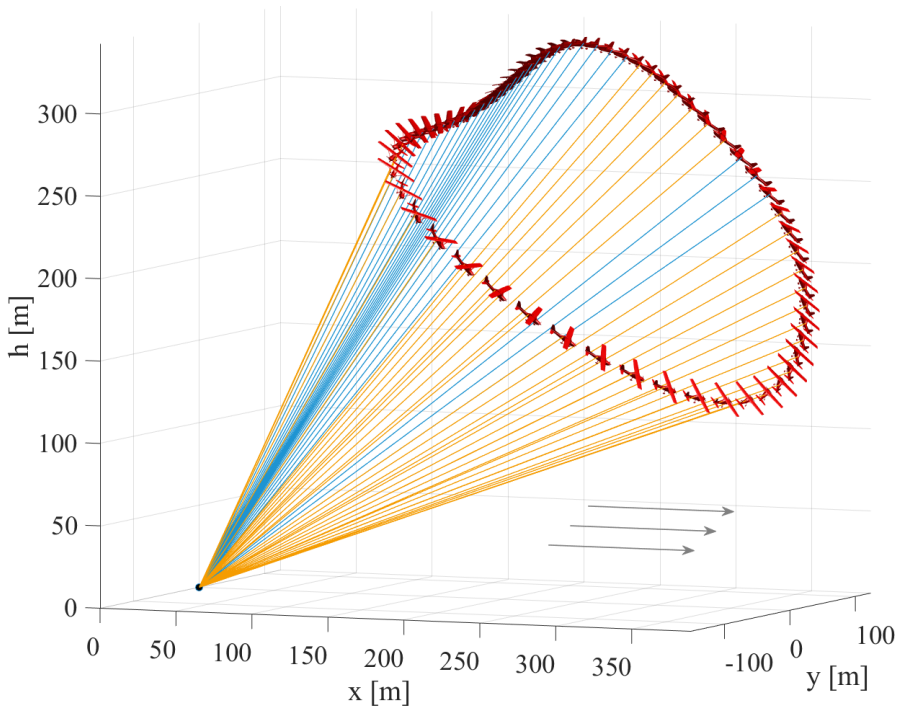


Figure 4.10: Optimal trajectory for a rigid wing pumping mode AWES in 3D (circular pattern). The blue tether corresponds to the reel-in (power consumption) phase, while the orange tether denotes the reel-out (power production) phase.

4.2.4 Size trajectory comparison and AWE wind farm

In order to generate a noticeable amount of energy, AWES need to be arranged in so called *wind farms*, i. e. a set of AWES installed at the same location with a specific layout. As shown in Figure 4.11, for conventional wind farms it is common practice to introduce spacing between wind turbines equal to $14l_B$ in the wind prevalent direction and $8l_B$ in the transverse direction with l_B the blade length, so that the *wake effects* are minimized [96].

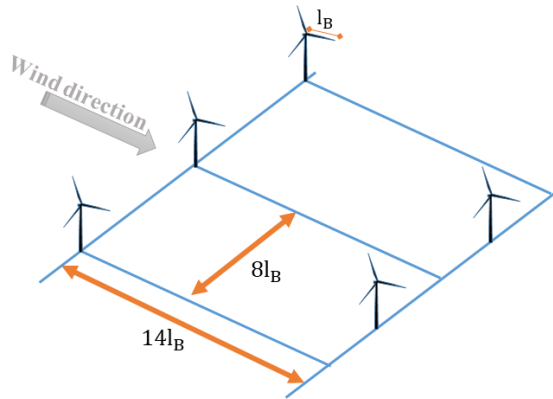


Figure 4.11: Layout of conventional wind farms [38]. l_B denotes the blade length.

A standardized layout for AWE farms is object of ongoing research, though, it is expected that wake losses are quite limited in comparison to conventional wind turbines. As a consequence, the spacing between AWES can be significantly reduced so that the surface power density (MW/km^2) is enhanced. Additionally, one can compare the flight trajectories obtained in Section 4.2.3 and Section 4.2.1 to assess which topology may require less surface. It turns out that despite both trajectories theoretically produce the same amount of power, the circular trajectory is less wide than the lemniscate trajectory (see Figure 4.13). As a consequence, in an AWE farm, circular trajectories can deliver a higher surface power density compared to lemniscate trajectories. Exemplary, let us consider the layout proposed in [67] with a facility density of $1.2/l_{\max}^2$ where l_{\max} is the maximum tether length. The layout implicitly assumes that the aircraft trajectories do not interfere each other with additional safety margin. Results show that for this specific set-up, circular trajectories can reduce up to $\approx 40\%$ of area required compared to lemniscate trajectories, see Figure 4.12.

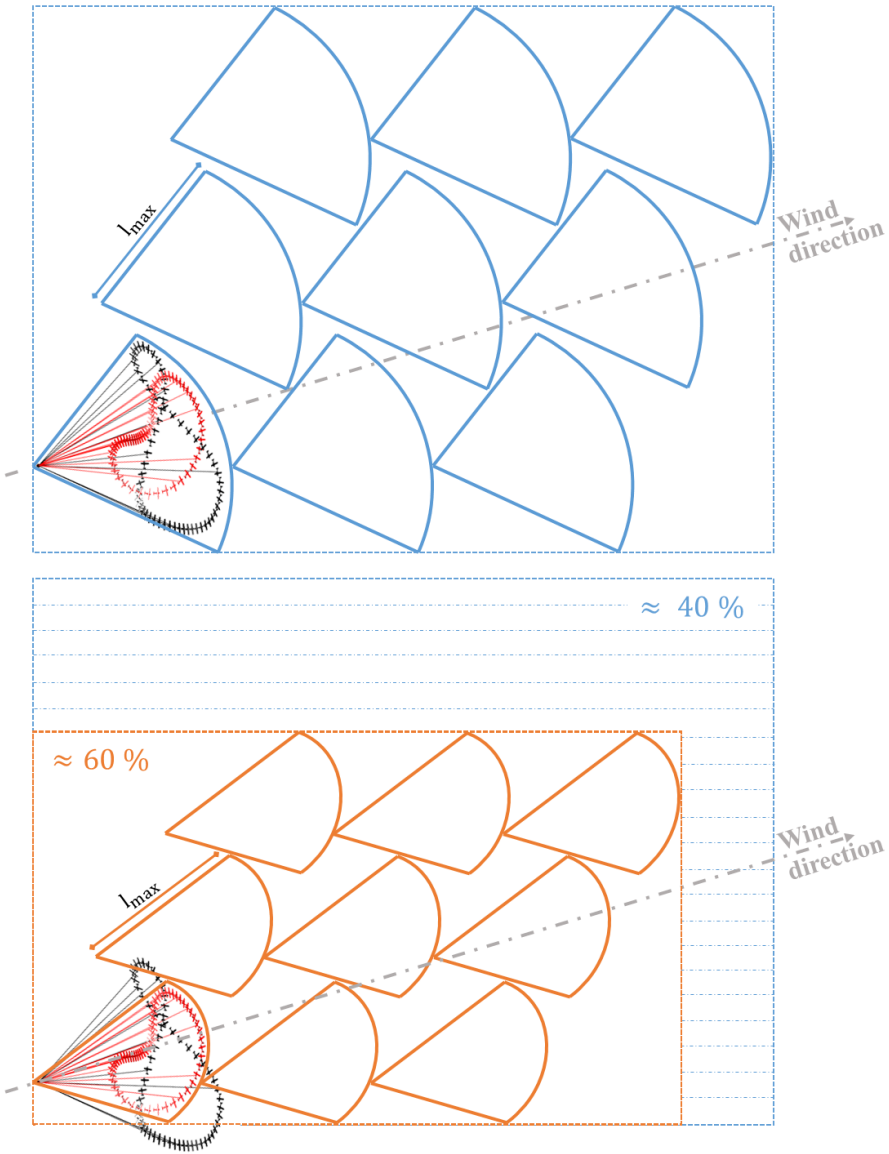


Figure 4.12: AWE farm layout with facility density of $1.2/l_{\max}^2$ for a given wind direction proposed in [67]. l_{\max} denotes the maximum tether.

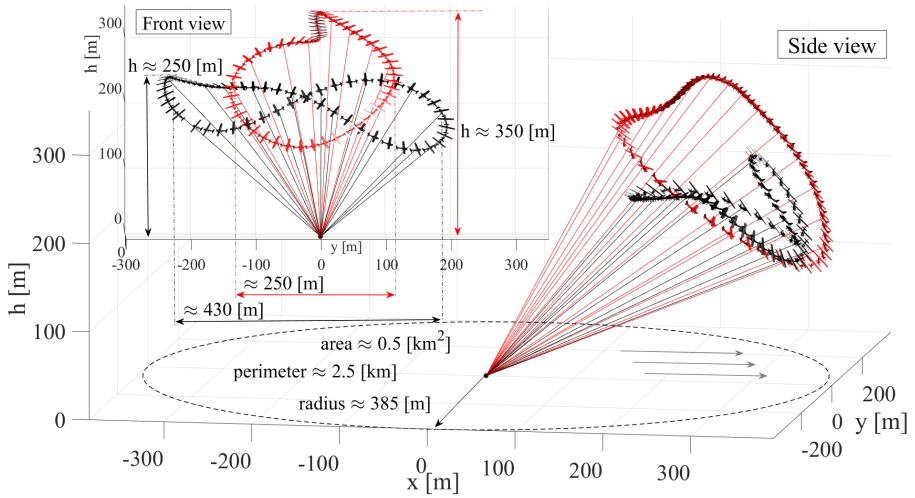


Figure 4.13: Size comparison between lemniscate and circular trajectory under equal boundary conditions.

4.3 Algorithm validation

In general, AWES need to be scaled-up in order to be competitive with respect to conventional wind turbines. Such process is not trivial and it requires several iterations due to the numerous variables that need to be taken into account simultaneously. Within this framework, mathematical tools that are able to compute both feasibility and average power output assessments for a plant with specific physical properties are crucial for scaling-up purposes.

One way to systematically address such analysis is through the OCP implemented within this chapter. Basically, if the mathematical model taken into account in the OCP (4.13) is sufficiently accurate, the obtained optimal solution will correspond to a feasible trajectory with a certain average power output. As a result, one can obtain an insight regarding the system performance without actual experiments.

However, solutions that are carried out via an optimal control approach are based on strong assumptions, such as the mathematical formulation which describes the system dynamics of the real plant is fully free from model mismatch and parametric uncertainty. Additionally, one implicitly assumes that the plant operates in a disturbance-free scenario. Hence, if these assumptions were true, the real plant can operate in open-loop, i. e., no feedback controls are required.

In the previous chapters, it was shown that the mathematical representation of an AWES is subject to many uncertainties and it relies on several model assumptions. Further, the system operates in a gusty environment. As a consequence, the model prediction deviates from the actual plant behavior. In order to deal with such *model-plant mismatch* issues, it is common practice to design ad-hoc feedback control systems with specific margins of robustness. Therefore, in a real environment the plant operates in closed-loop, though, from classical control theory it is well known that robust feedback laws involve a degradation of the overall system performance. Additionally, industrial control systems are often tuned via heuristic techniques which may lead to further performance losses. In this case, the average power output obtained via a closed-loop solution is reduced w.r.t. its equivalent optimal open-loop solution.

Ideally, for validation purposes one should compare the OCP outcome with experimental data sets where the reference input tracking is a computed optimal flight trajectory. Unfortunately, only experimental data sets carried out with non-optimal, though well tuned flight trajectories are available. In this case, one can still validate the optimal outcomes by initializing the OCP (4.13) with a simulated closed-loop solution obtained by the actual Flight Control Computer (FCC). Subsequently, the system performance can be compared in terms of average power output. Validation results are then satisfactory if the deviation

of the average power output P_{AV} between the open and closed-loop trajectory obtained in a simulation environment is roughly equal to the corresponding deviation obtained within a real environment.

In agreement with the considerations mentioned above, let us initialize the OCP (4.13) with a solution obtained in closed-loop using the highly accurate simulator designed by Ampyx Power B.V. [3]. The closed-loop simulation is carried out under realistic atmospheric conditions and using the actual control system embedded in the FCC. In this case, homotopy strategies are not required since the initial guess is already a feasible solution.

In Figure 4.14, 4.15, 4.16 the initial guess (closed-loop simulation) is compared with the corresponding optimal open-loop solution. The OCP converges to a wider trajectory with a slightly higher elevation angle compared to the closed-loop simulation retrieved by tracking a flight trajectory heuristically tuned. In both cases a second reel-in phase occurs at the left trajectory corner to counteract the loss of airspeed relative to the airborne component, and eventually to avoid slack phenomena in the tether.

In an optimal scenario the expected average power output P_{AV} is roughly 4.6 kW, whereas in a sub-optimal scenario characterized by a cascade control architecture described in [95], with reference input tracking a flight trajectory tuned with heuristic techniques, the performance are reduced by the $\approx 10\%$ w.r.t. the optimal scenario. Such loss of performance is attributed primarily to the tracker controllers relative to the tether tension and the angle of attack (see Figure 4.15). The tension controller is based on an indirect control of the tether tension by means of the winch speed, and results show that there a margin of improvement in terms of system efficiency by performing a better tuning of the control gains. As far as it regards the angle of attack, it turns out that from a practical point of view the designing of a controller that is able to hold constantly the angle of attack during crosswind flights is rather difficult. As a results, the lift generated during the power generation phase is not uniform and with a minor magnitude w.r.t. the optimal scenario.

Once the gap between the optimal open-loop trajectory and the closed-loop simulation performed with the actual set-up is known, the optimal solution is measured against real crosswind flights. For the purpose of validation, the mechanical average power output P_{AV} is taken into account. The experimental data set is retrieved from [95] and they are shown in Figure 4.17 compared to optimal values obtained via the OCP (4.13).

For this application, results show that the actual system performance is reduced by roughly 15% w.r.t. the predicted optimal behavior, where $\approx 10\%$ are associated to the controllers performance, whereas the remaining 5% are caused by communication latencies between the aircraft and the ground station, and

turbulence [95]. Further, various model-plant mismatches act on the overall system performance, e. g., due to the simplification of the wind shear, inaccuracy in the aerodynamic properties as well as tether dynamics approximation with corresponding drag assumed within this work. Nevertheless, the error between the actual and the predicted system performance is acceptable.

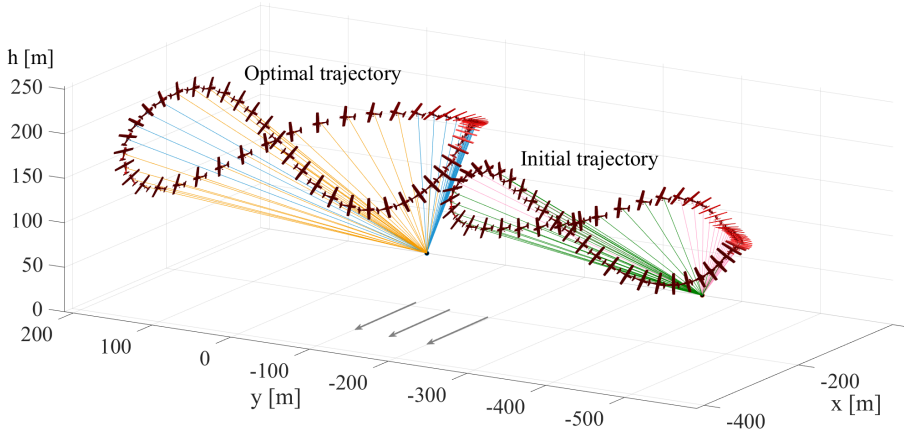


Figure 4.14: Comparison in 3D between optimal open-loop trajectory (left) and simulated closed-loop trajectory (right) used as initial guess with average wind speed at operating altitude $w(h) \approx 10$ m/s. In the open(closed)-loop solution the reel-in phase is denoted with blue(pink) tether, whereas the orange(green) tether corresponds to the reel-out phase. The main reel-in phase arises in the right corner (picture view), though, a further reel-in phase occurs in the left corner to prevent loss of airspeed of the airborne component.

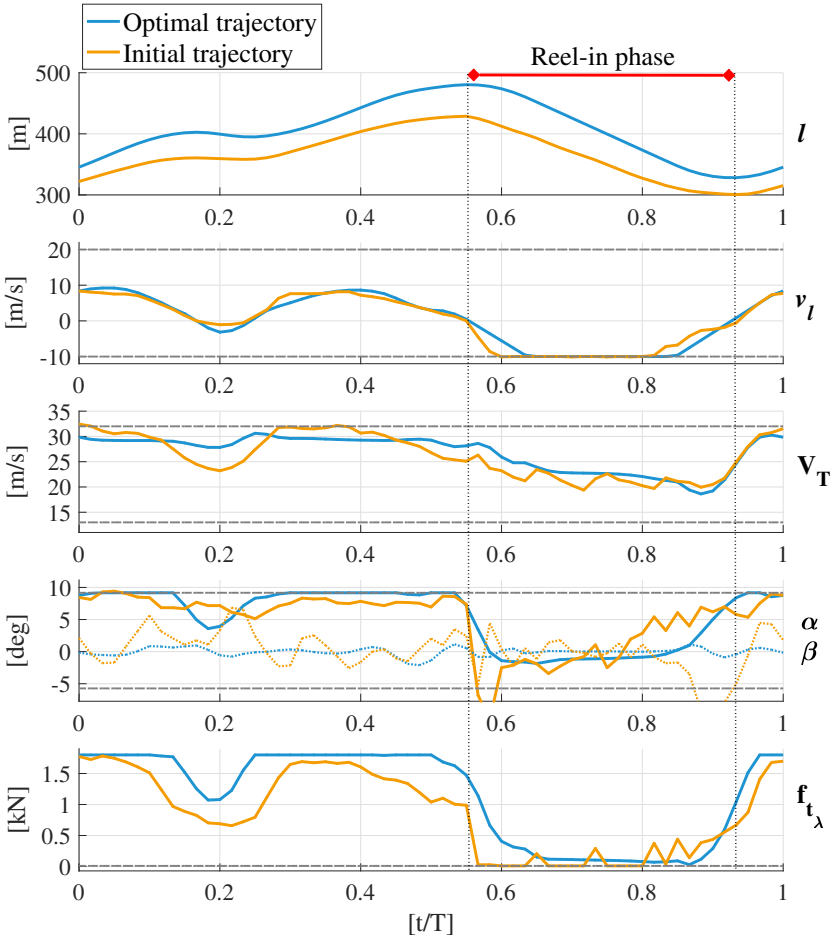


Figure 4.15: Comparison between optimal open-loop (blue) and closed-loop simulation (orange) used as initial guess. From the top it is shown in normalized time scale the tether length l , tether speed v_l , airspeed V_T , angle of attack α , angle of side slip β (dot lines) and tether tension f_{t_λ} . Path constraints are shown in dash dot grey line. In both cases a second reel-in phase occurs in order to prevent the loss of airspeed of the aircraft. The pumping cycle time is $T \approx 50$ s and $T \approx 43$ s for the optimal and initial trajectory, respectively. Finally, as far as it regards the angle of side slip β , on the one hand its value is kept close to zero (as required) along the entire optimal trajectory. On the other hand, the control system designed by Ampyx Power B.V. is capable to bound β under realistic atmospheric conditions.

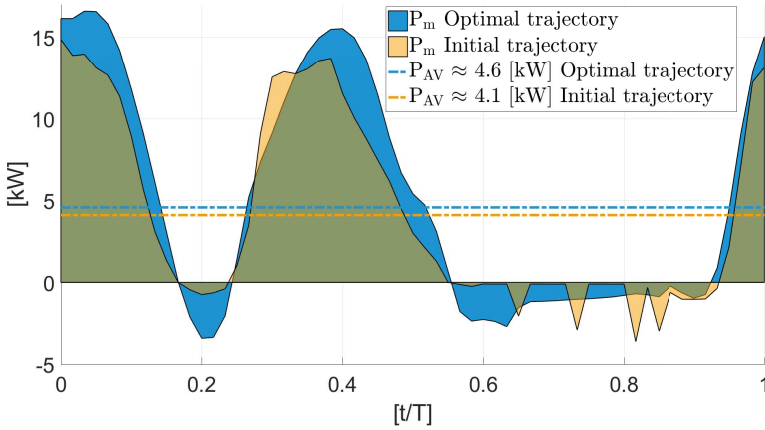


Figure 4.16: Mechanical power P_m comparison between optimal open-loop trajectory and closed-loop simulation with corresponding average power output P_{AV} , with normalized time scale. The tether speed v_l and tether tension f_{t_λ} produce a certain amount of mechanical power P_m that is subsequently converted to electrical power P_e by the generator. Under optimal conditions, the expected average mechanical power output P_{AV} is roughly 4.6 kW, whereas it is expected that the current control system implemented by Ampyx Power B.V. causes a loss of performance $\approx 10\%$ w.r.t. the optimal scenario.

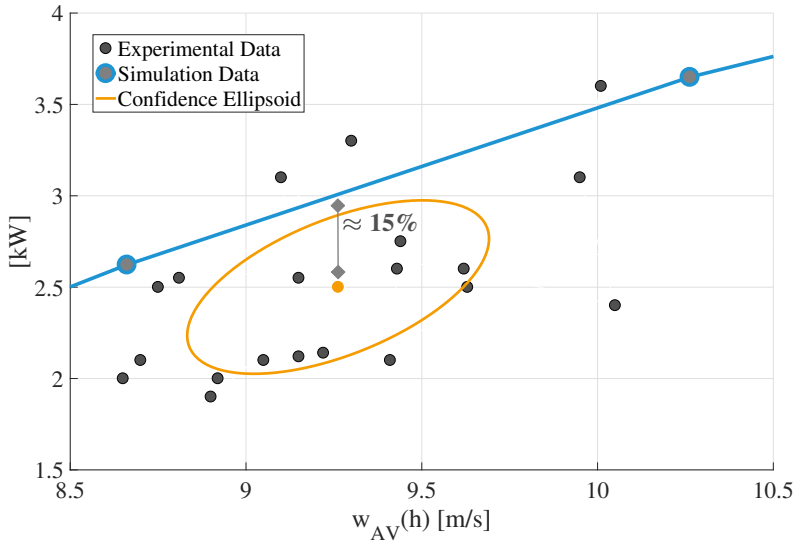


Figure 4.17: Optimal average power output P_{AV} (grey dots) with corresponding interpolation (blue line) compared against an experimental data set (black dots).

4.4 Performance analysis

Reliable tools capable of computing performance analyses of an AWES prior to real experiments are crucial for viability assessments for scaling-up purposes. Similarly to conventional wind turbines, AWES performance can be evaluated analyzing their corresponding power curves, i. e., the net power produced along a range of wind speeds. However, in contrast to other wind energy conversion systems, the net electrical power output of an pumping mode AWES refers to the average power that the system can generate over the whole pumping cycle under optimal conditions [52].

In principle, power curves can be very costly to compute for a given AWES, since numerous variables need to be taken into account simultaneously, e. g.,

- maximum sustainable tension within the reel-out (power production) phase;
- power consumption during the reel-in phase;
- duration of reel-in and reel-out phase per loop;
- aerodynamic characteristics such as lift and drag curve of the airborne component;
- elevation angle and tether length.

Within an optimization framework, the power curve can be systematically obtained by solving a sequence of OCPs (4.13) for a range of wind speeds. The OCPs take into account equal wind shear, though, with different wind speed magnitudes that are varied by the wind speed measured at the anemometer height w_{h_a} (see (2.1)). Once the first OCP is solved, the subsequent OCP can be initialized with the previous solution and for a different value of w_{h_a} .

In Figure 4.18, an example of trajectories associated to the cases of low, medium and high wind conditions is shown. During low wind conditions, the plant operates with a high elevation angle, whereas the aircraft flies close to the winch so as to reduce the drag associated to the tether. By increasing the wind speed, the elevation angle decreases and the aircraft performs crosswind flights adopting a control strategy described in Section 4.2.1. With a further increment of the wind speed, the plant is prone to operate newly with a high elevation angle, though, far from the winch in order to limit the tension in the tether, whereas the flight trajectory is wider with a longer reel-in phase w.r.t. to the previous case.

Figure 4.19 shows the power curve relative to the case study, evaluated within a range of w_{h_a} from 0 m/s to 20 m/s with a step size of 1 m/s and interpolated

subsequently. Note that the x-axis corresponds to the average wind speed at operating altitude $w_{AV}(h)$. The power curve is divided into four parts. Between zero and the cut-in wind speed, $w(h) \approx 4$ m/s, the aircraft is kept aloft using optimal holding patterns via a reversed pumping strategy. In this case, the net power output produced along the flight trajectory is negative due to low wind conditions (see Section 4.2.2). From the cut-in wind speed onwards, power production reaches its maximum value of ≈ 9 kW for $w(h) \approx 22$ m/s. In the third part, system performance slightly decreases due to a higher investment in terms of both time and energy required during the reel-in phase. Beyond the cut-out speed $w(h) \approx 25$ m/s, it is assumed that the plant does not operate for safety reasons, hence, no power is produced.

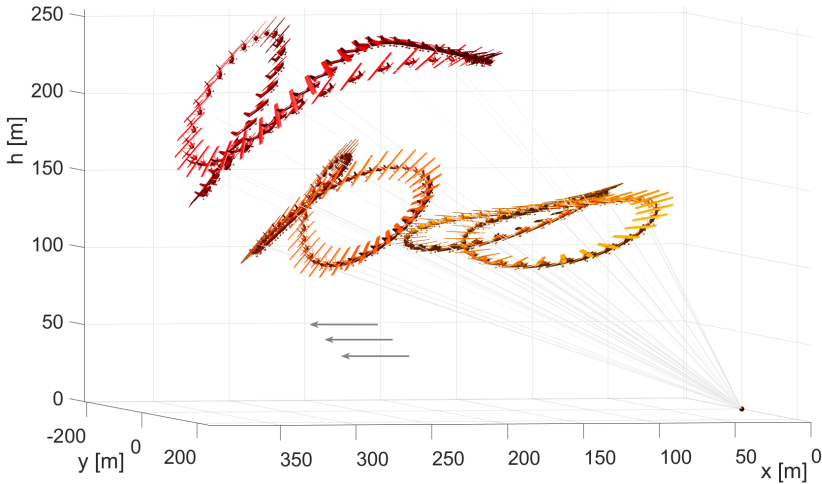


Figure 4.18: Example of trajectories associated to the cases of low, medium and high wind conditions. The grey arrows denote the wind direction.

The system performance is further assessed by means of the *Power Harvesting Factor* ξ , which is defined for a specific average wind speed $w_{AV}(h)$ at operating altitude h read as

$$\xi = \frac{P_{AV}}{P_S} \quad (4.16)$$

where P_S denotes the wind power that flows through the cross sectional area of size equal to the aircraft wing area S , i. e.,

$$P_S = \frac{1}{2} \rho S w_{AV}^3(h). \quad (4.17)$$

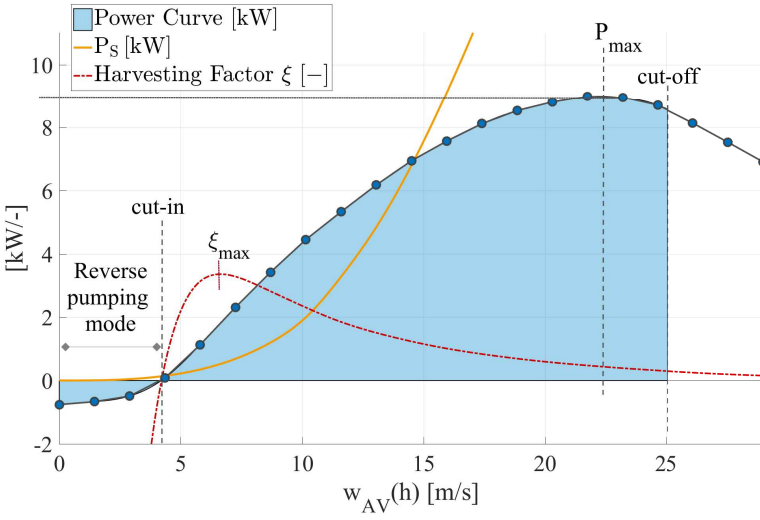


Figure 4.19: System performance expressed in power curve. In the y-axis, optimal average mechanical power P_{AV} (blue dot line), theoretical power produced by a wing of area A (orange line), and power harvesting factor ξ (dash-dot red line) versus average wind speed at operating altitude $w(h)$ (x-axis).

Nowadays, conventional wind turbines have a Power Harvesting Factor of approximately 5.5 [31]. For the case study, the maximum Power Harvesting Factor ξ_{\max} is ≈ 3.5 and it occurs at $w_{AV}(h) \approx 6.5$ m/s, as also depicted in Figure 4.18. Such a low value is not surprising since the plant considered within this work is used as a case-study for testing and verification purposes only.

4.4.1 Annual energy production and capacity factor

Once the power curve is known, one can obtain an estimation of the Annual Energy Production (AEP) that takes into account the wind variations through distribution functions. The probability of occurrence of a given wind speed w can be well described in most locations by a Weibull probability density function $g(\cdot)$ equal to

$$g(w) = \frac{k}{w_m} \left(\frac{w}{w_m} \right)^{k-1} \cdot e^{-\left(\frac{w}{w_m}\right)^k} \quad (4.18)$$

where k is a unit-less shape parameter, and w_m a scale parameter given in m/s. Typical values of k are between 1.5 and 2, whereas w_m is proportional to the average wind speed w_{AV} [76]. Both parameters can be tuned based on either previous measurements related to a specific location or using the international standard IEC 61400-12-1 [57]. Exemplary, the wind distribution wind class-1A shown in Figure 4.20 is considered within this work [79].

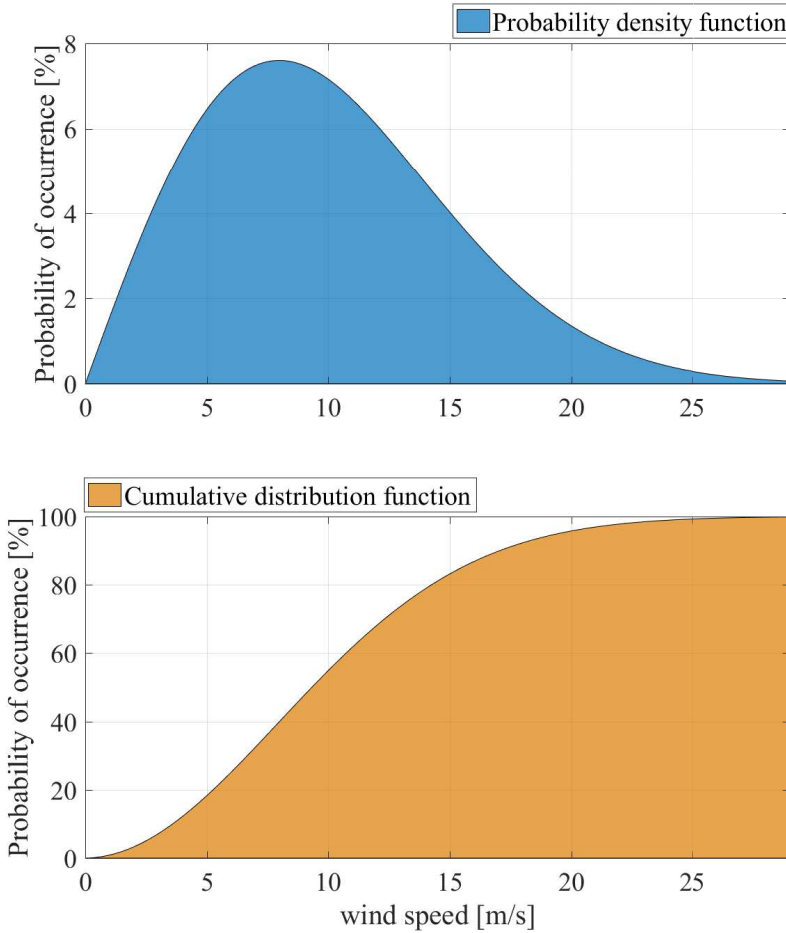


Figure 4.20: Wind class-1A density function with corresponding cumulative distribution function.

The AEP of an AWES is then calculated by integration of the product between the power curve (see Figure 4.19) and the wind distribution (4.18). The outcome regarding the case study under the assumptions of optimal crosswind flights is depicted in Figure 4.21.

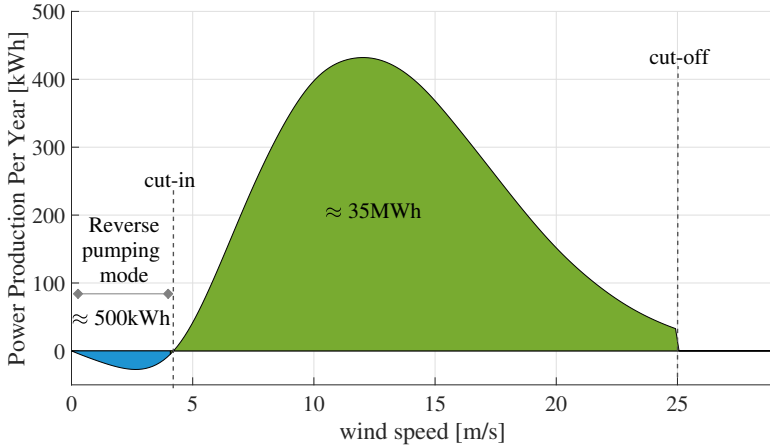


Figure 4.21: Power Production per year relative to the case study. The blue area denotes the total energy used to keep the aircraft airborne during low wind conditions, whereas the green area correspond to the total energy harvested.

It turns out that the energy produced over one year by a small pumping mode AWES with wing area of 5.5 m^2 is approximately 35 MWh. Such analysis also reveals that the relative cost, i.e. the ratio between the energy consumption to keep the system aloft (using a reverse optimal pumping strategy) and the total energy harvested by the system is $\approx 1.5\%$. Therefore, the choice to continue flying during low wind conditions can potentially avoid the need for costly and time consuming launch and landing procedures compared to a negligible amount of energy used to keep the aircraft airborne [72].

Additionally, if one assumes that the energy has a time-independent tariff, it is possible to describe the performance of a system by the so called *capacity factor* CF defined as the ratio between the actual energy produced over a year (E_{AEP}), and the potential maximum power output P_{max} if it were possible for the AWES to operate at full capacity continuously over one year, i. e.,

$$\text{CF} = \frac{E_{\text{AEP}}}{8760 \cdot P_{\text{max}}} \quad (4.19)$$

where 8760 is the number of hours per (non-leap) year. Conventional wind turbines have a CF between 30% and 35% [76]. For such AWES, the capacity factor is equal to 42.5%.

In conclusion, AEP and CF can be augmented with further analysis related to Operating and Maintenance costs (O&M), various market factors and economic viability indicators. For more details the reader is referred to [76].

Chapter 5

Conclusions

This work focused on the identification of aerodynamic models and trajectory optimization with subsequent performance assessment of a rigid wing pumping mode Airborne Wind Energy System (AWES). The proposed methods were validated against experimental data obtained using a 5.5 m wing span prototype designed by the Dutch company Ampyx Power B.V. [3].

In Chapter 2, the mathematical formulation of a rigid wing AWE pumping system suitable for system identification and Optimal Control Problems (OCPs) has been presented. Each system component was described separately via Newtonian mechanics, whereas the tether was modeled as a rigid link and with an approximation of its aerodynamic characteristics. Finally, the overall mathematical model was formulated as a set of Differential Algebraic Equations (DAEs).

In Chapter 3, successful flight test campaigns that aim towards the identification of aerodynamic models of a high lift, autonomous aircraft have been presented. A comprehensive non-linear mathematical model for system identification purposes was introduced underlying model assumptions. The flight test procedures have been described, and in order to both simplify the overall system modeling and to avoid disturbances caused by possible tether vibrations, the flight tests were performed untethered, with fixed airspeed and straight direction. Further, the excitation signals were carried in open-loop and with propeller switched off to improve the Signal-to-Noise Ratio (SNR), though, a flight envelope protection was designed to avoid loss of stability with subsequent crash of the vehicle. A set of three experiments relative longitudinal dynamics were collected via conventional excitation signals widely used within the aerospace field, i. e. the 3-2-1-1 maneuver, and guideline on how to heuristically tune such maneuver was provided.

Within this chapter, it was also shown how to design optimal experiments that aim to reduce the number of flight tests by reducing the parameter uncertainties using optimized maneuvers, and simultaneously enforcing safety constraints. The optimized experiments were carried out for the roll, pitch and yaw dynamics for the steady state wing level trim condition. The Optimum Experimental Design (OED) problem was initialized using a priori aerodynamic derivatives obtained via lifting line methods augmenting them with previous flight test campaign. In all cases the proposed OED led to a bang-bang type input signal with finite slope. The optimal solutions were compared with the 3-2-1-1 maneuvers and their estimation performance were assessed by the Cramen Rao Lower Bound (CRLB). On the one hand, simulation results have shown that optimal inputs are able to reduce the estimation uncertainty more than well tuned 3-2-1-1 maneuvers. On the other hand, experimental results have demonstrated that given a fair accuracy of the a priori model, the open-loop aircraft response is bounded within the prescribed constraints. Note that, for safety reasons the optimal aileron sequence was not carried out completely. In any case, it is advisable to apply conventional signal inputs during the preliminary stage of the flight test campaign where high inaccuracies might be present.

Once the experimental data were collected, the aircraft aerodynamic model was identified via a Model-Based Parameter Estimation (MBPE) algorithm. In order to deal with turbulence effects, aerodynamic derivatives were estimated within one single large-scale optimization problem which takes into account all collected data carried out by both conventional and optimized maneuvers for a given steady state wing-level trim condition. The identified model was assessed by a time domain model validation, residual distribution analysis and Theil Inequality Coefficients (TIC). Estimation results have brought to light that aerodynamic model identification via flight tests are able to improve the predictive capability of low fidelity a priori models for a high lift, rigid wing aircraft. However, baseline (a priori) models are equally important to deal with non identifiable dynamics as well as for designing maneuvers for system identification purposes.

In Chapter 4, flight trajectories relative to the case study have been obtained through solution of an Optimal Control Problem (OCP) based on a mathematical model described by an index-1 DAE. System characteristics and path constraints were defined in agreement with the actual plant. The OCP was formulated within the open-source toolbox OPENAWE [62], and a non-confidential version of the optimization tool has been released.

The OCP was validated against a set of experimental data in terms of mechanical average power output. Within such analysis, the discrepancy between an optimal open-loop solution with a simulated closed-loop solution carried out using the actual Flight Control Computer (FCC) designed by Ampyx Power

B.V. was quantified. On the one hand, it turns out that non-optimal flight trajectories combined with a cascade control architecture characterized by industrial controllers can achieve performances close to the optimal scenario. On the other hand, it was shown that the system efficiency might be further enhanced by improving the controllers performance relative to the angle of attack and tension control. For this specific application, the performance losses were $\approx 15\%$ compared to the optimal scenario.

A lemniscate trajectory was compared with a circular trajectory under equal boundary conditions, showing that in both cases the same amount of energy is harvested per loop, in other words, the system performance does not depend on the trajectory topology. However, circular trajectories may potentially deliver a higher surface power density due to a smaller width of the pattern.

Ultimately, by solving a sequence of optimal control problems for a range of wind speeds, the power curve and harvesting factor were systematically obtained for the case study. Within such analysis, it was demonstrated how the optimization tool suggests to perform holding patterns with minimum allowable altitude and close to the ground station for low wind conditions so as to minimize the tether drag and consequently the power losses. Further, simulation results have shown that the choice to continue flying during low wind conditions can potentially avoid the need for costly and time consuming launch and landing procedures compared to a negligible amount of energy used to keep the aircraft airborne. In contrast, for high wind speeds it is advisable to increase both the tether length and elevation angle to limit the tension that arises on the airframe during the power generation phase.

In conclusion, it has been shown that many decision tasks relative to the scaling up of an AWES can be significantly facilitated with the proposed tool.

Appendix A

List of Tables

Table A.1: friction coefficient c_f for various terrain types [81].

Terrain characteristics	c_f [-]
Smooth hard ground, calm water	0.10
Tall grass on level ground	0.15
High crops, hedges and shrubs	0.20
Small town with trees and shrubs	0.30
Large city with tall buildings	0.40

Table A.2: Physical properties of the aircraft designed by Ampyx Power B.V. [3].

Name	Symbol	Value	Unit
Mass	m	36.8	[kg]
Moment of inertia	J_x	25	[kg · m ²]
Moment of inertia	J_y	32	[kg · m ²]
Moment of inertia	J_z	56	[kg · m ²]
Cross moment of inertia	J_{xz}	0.47	[kg · m ²]
Reference wing span	b	5.5	[m]
Reference chord	\bar{c}	0.55	[m]
Reference wing area	S	3	[m ²]
Aspect ratio	AR	10	[-]

Table A.3: Polynomial coefficients relative to C_X , C_Y and C_Z .

C_X	c_0	c_1	C_Y	c_0	c_1	C_Z	c_0	c_1	c_2
C_{X_α}	-	8.32	C_{Y_β}	-0.19	-	C_{Z_α}	-	1.23	10.20
C_{X_q}	-0.60	4.41	C_{Y_p}	-0.10	-	C_{Z_q}	-7.56	0.13	6.15
$C_{X_{\delta_e}}$	-0.01	0.11	C_{Y_r}	0.17	0.14	$C_{Z_{\delta_e}}$	-0.32	-	0.29
C_{X_0}	0.46	-	$C_{Y_{\delta_a}}$	-0.05	-	C_{Z_0}	-5.40	-	-
-	-	-	$C_{Y_{\delta_r}}$	0.10	-	-	-	-	-

Table A.4: Polynomial coefficients relative to C_l , C_m and C_n .

C_l	c_0	c_1	C_m	c_0	c_1	c_2	C_n	c_0	c_1
C_{l_β}	-0.06	-	C_{m_α}	-	0.21	-	C_{n_β}	0.06	-0.09
C_{l_p}	-0.56	-	C_{m_q}	-11.30	-	5.29	C_{n_p}	-0.06	-0.91
C_{l_r}	0.18	0.65	$C_{m_{\delta_e}}$	-1.02	-	-	C_{n_r}	-0.05	-
$C_{l_{\delta_a}}$	-0.25	0.04	C_{m_0}	-0.32	-	-	$C_{n_{\delta_a}}$	0.02	-0.12
$C_{l_{\delta_r}}$	-	-	-	-	-	-	$C_{n_{\delta_r}}$	-0.04	-

Table A.5: Physical properties of tether.

Name	Symbol	Value	Unit
Drag coefficient	C_{D_t}	1.2	[-]
Linear density	ρ_t	0.0046	[kg/m]
Diameter	d_t	0.002	[kg]

Table A.6: Sensors noise standard deviation σ_y

Sensor	Variable	σ_y	Unit
Five hole pitot tube	V_T	1.0	m/s
Five hole pitot tube	(α, β)	0.5	deg
IMU	(ϕ, θ, ψ)	0.1	deg
IMU	(p, q, r)	0.1	deg/s

Table A.7: A priori longitudinal dimensional aerodynamic derivatives for the steady wing-level flight condition with $V_{T_e} = 20$ [m/s].

X-axis	Value	Z-axis	Value	M-axis	Value
X_V	-0.147	Z_V	-0.060	M_V	0.0
X_α	7.920	Z_α/V_{T_e}	-4.400	M_α	-7.688
X_q	-0.163	Z_q/V_{T_e}	0.896	M_q	-1.963
X_{δ_e}	-0.232	Z_{δ_e}/V_{T_e}	-0.283	M_{δ_e}	-10.668

Table A.8: A priori lateral dimensional aerodynamic derivatives for the steady wing-level flight condition with $V_{T_e} = 20[\text{m/s}]$.

Y-axis	Value	L-axis	Value	N-axis	Value
Y_β/V_{T_e}	-0.167	L'_β	-8.201	N'_β	3.214
Y_p	0.0	L'_p	-11.292	N'_p	-0.750
Y_r	-0.976	L'_r	3.853	N'_r	-0.457
Y_{δ_a}/V_{T_e}	-0.046	L'_{δ_a}	-32.600	N'_{δ_a}	0.716
Y_{δ_r}/V_{T_e}	0.093	L'_{δ_r}	0.524	N'_{δ_r}	-2.370

Table A.9: Flight envelope and OED constraints relative to the trim condition at $V_{T_e} = 20[\text{m/s}]$.

Variable	Flight envelope	OED constraints	Range	Unit
V_T	(12,30)	(17,23)	6	[m/s]
β	(-20,20)	(-7.5,7.5)	15	[deg]
α	(-8,20)	(-4.36,3.64)	8	[deg]
ϕ	(-35,35)	(-28,28)	56	[deg]
θ	(-30,40)	(-28.77,27.33)	56	[deg]
p	(-60,60)	(-48,48)	96	[deg/s]
q	(-40,40)	(-32,32)	64	[deg/s]
r	(-40,40)	(-32,32)	64	[deg/s]
$(\delta_a, \delta_e, \delta_r)$	(-, -)	(-5,5)	10	[deg]
$(\dot{\delta}_a, \dot{\delta}_e, \dot{\delta}_r)$	(-, -)	(-3.25,3.25)	7	[rad/s]

Table A.10: Path constraints.

Name	Variable	min	max	unit
angle of attack	α	-6.0	9.0	[deg]
angle of side slip	β	-20.0	20.0	[deg]
airspeed	V_T	13.0	32.0	[m/s]
altitude	h	100.0	-	[m]
tether tension	$f_{t,\lambda}$	10.0	1800.0	[N]
roll angle	ϕ	-50.0	50.0	[deg]
pitch angle	θ	-40.0	40.0	[deg]
tether length	l	10.0	700.0	[m]
tether speed	v_l	-15.0	20.0	[m/s]
tether acceleration	a_l	-2.3	2.4	[m/s ²]
aircraft angular velocity	$\omega^{\mathbf{b}}$	-50.0	50.0	[deg/s]
aileron deflection	δ_a	-20.0	20.0	[deg]
elevator deflection	δ_e	-30.0	30.0	[deg]
rudder deflection	δ_r	-30.0	30.0	[deg]
servo speed	\mathbf{v}_δ	-2.0	2.0	[rad/s]
trajectory time	T	20.0	70.0	[s]

Appendix B

List of Figures

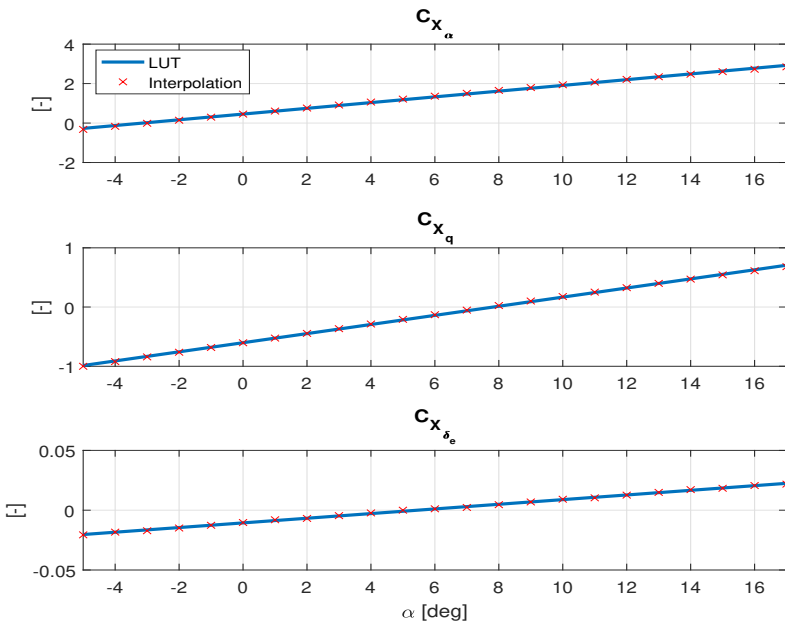


Figure B.1: 1-D look-up tables of C_X derivatives versus α with their corresponding polynomial interpolation.

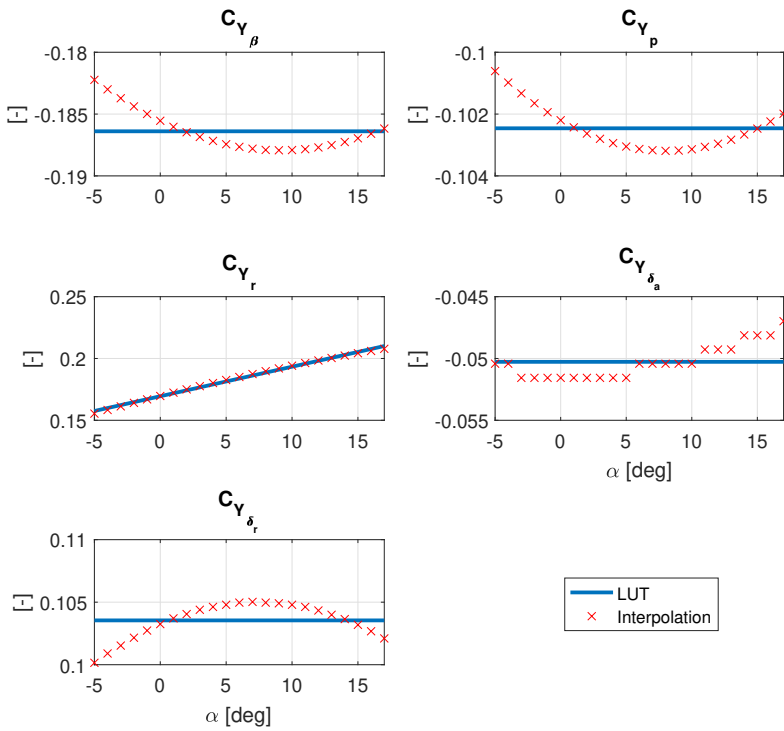


Figure B.2: 1-D look-up tables of C_Y derivatives versus α with their corresponding polynomial interpolation.

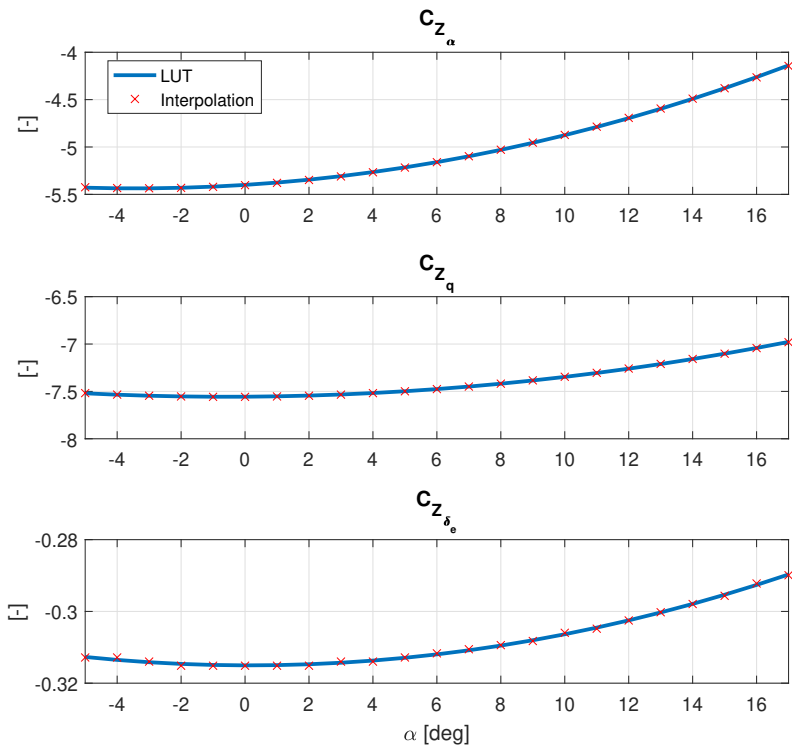


Figure B.3: 1-D look-up tables of C_Z derivatives versus α with their corresponding polynomial interpolation.

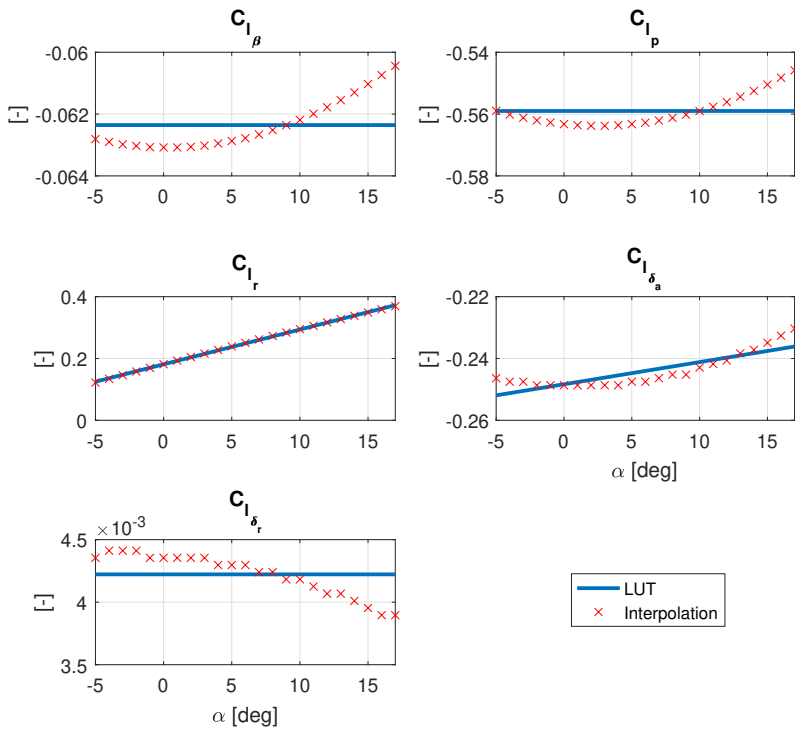


Figure B.4: 1-D look-up tables of C_{l_1} derivatives versus α with their corresponding polynomial interpolation.

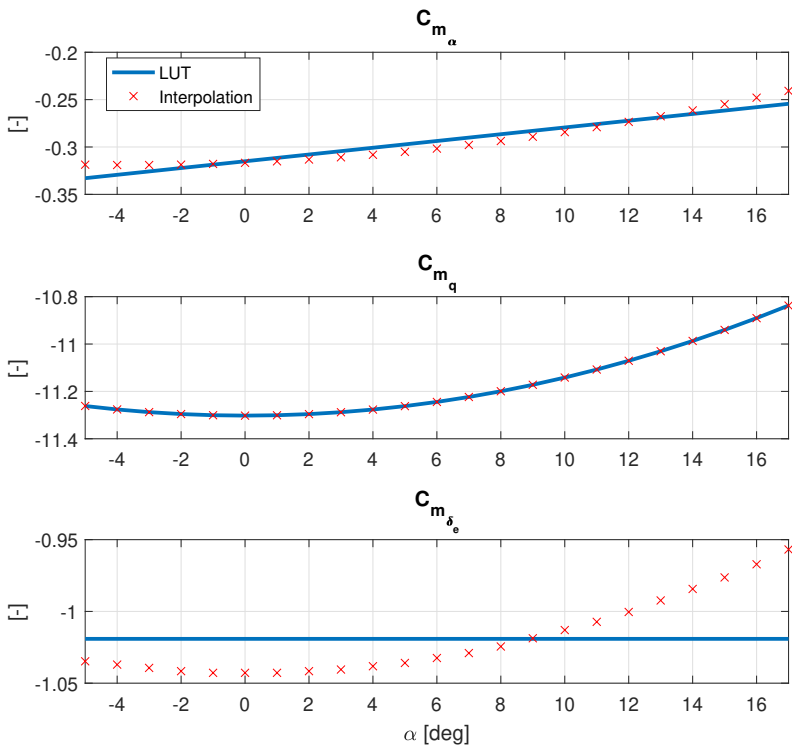


Figure B.5: 1-D look-up tables of C_m derivatives versus α with their corresponding polynomial interpolation.

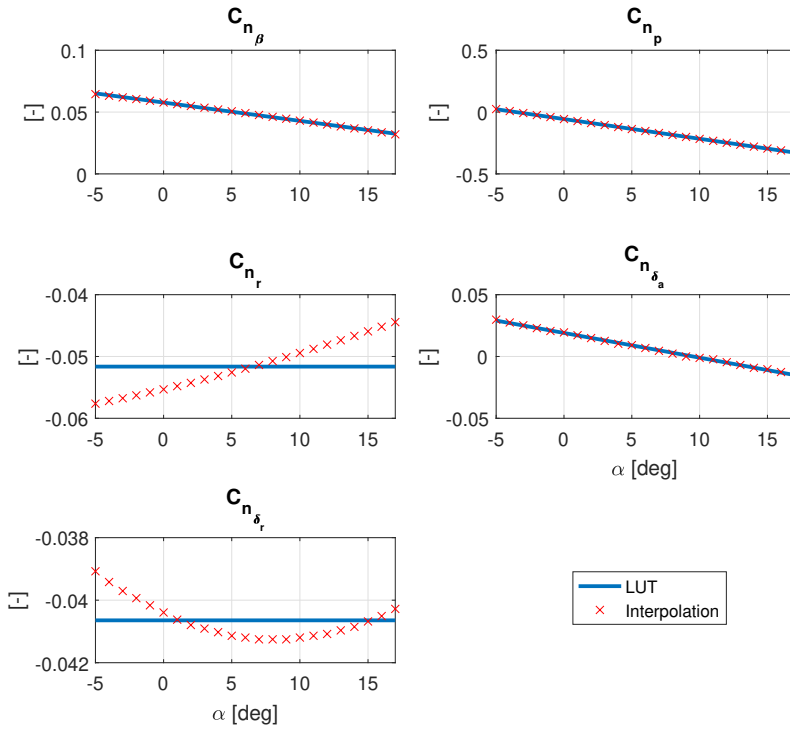


Figure B.6: 1-D look-up tables of C_n derivatives versus α with their corresponding polynomial interpolation.

Bibliography

- [1] Ampyx Power B.V., Optimal System Identification Flight Test. <https://www.youtube.com/watch?v=KBq5TTT0qf8>, 2017.
- [2] Makani. <https://x.company/makani/>, 2017.
- [3] Ampyx power: Airborne wind energy. <https://www.ampyxpower.com>, 2018.
- [4] e-kite. <http://www.e-kite.com/>, 2018.
- [5] kitemill. <http://www.kitemill.com/>, 2018.
- [6] Kps: Kite power solutions. <http://www.kps.energy/>, 2018.
- [7] Launch and landing mechanism for tethered aircraft designed by ampyx power b.v. <https://www.ampyxpower.com/ap3/launch/index>, 2018.
- [8] Twingtec: Wind energy 2.0. <http://twingtec.ch/>, 2018.
- [9] ANDERSON JR, J. D. *Fundamentals of Aerodynamics*, 6th ed. McGraw-Hill, 2017.
- [10] ANDERSSON, J. A. E., GILLIS, J., HORN, G., RAWLINGS, J. B., AND DIEHL, M. CasADi – A software framework for nonlinear optimization and optimal control. *Mathematical Programming Computation* (In Press, 2018).
- [11] ARCHER, C. L. An introduction to meteorology for airborne wind energy. In *Airborne wind energy*. Springer, 2013, pp. 81–94.
- [12] ARCHER, C. L., AND JACOBSON, M. Z. Evaluation of global wind power. *Journal of Geophysical Research: Atmospheres* 110, D12 (2005).
- [13] ARGATOV, I., RAUTAKORPI, P., AND SILVENNOINEN, R. Estimation of the mechanical energy output of the kite wind generator. *Renewable Energy* 34, 6 (2009), 1525–1532.

- [14] ARGATOV, I., AND SILVENNOINEN, R. Efficiency of traction power conversion based on crosswind motion. In *Airborne Wind Energy*. Springer, 2013, pp. 65–79.
- [15] ASCHER, U. M., AND PETZOLD, L. R. *Computer Methods for Ordinary Differential Equations and Differential-Algebraic Equations*, vol. 61. SIAM, 1998.
- [16] BANK, T. W. Fossil fuel energy consumption. <https://data.worldbank.org/indicator>, 2018.
- [17] BAUMGARTE, J. Stabilization of constraints and integrals of motion in dynamical systems. *Computer methods in applied mechanics and engineering* 1, 1 (1972), 1–16.
- [18] BETTS, J. T. Survey of numerical methods for trajectory optimization. *Journal of Guidance, Control, and Dynamics* 21, 2 (1998), 193–207.
- [19] BETTS, J. T. *Practical methods for optimal control and estimation using nonlinear programming*. SIAM, 2010.
- [20] BIEGLER, L. T. *Nonlinear Programming: Concepts, Algorithms, and Applications to Chemical Processes*, vol. 10. Siam, 2010.
- [21] BOCK, H. G., CARRARO, T., JÄGER, W., KÖRKEKEL, S., RANNACHER, R., AND SCHLÖDER, J. *Model Based Parameter Estimation: Theory and Applications*, vol. 4. Springer Science & Business Media, 2013.
- [22] BOCK, H. G., AND PLITT, K.-J. A multiple shooting algorithm for direct solution of optimal control problems. In *IFAC world congress* (Jul 1984), Elsevier.
- [23] BÜRGER, A. casiopeia – Casadi Interface for Optimum experimental design and Parameter Estimation and Identification Applications. <https://github.com/adbuenger/casiopeia>, 2016.
- [24] BÜRGER, A., KOUZOUPIS, D., ALTMANN-DIESES, A., AND DIEHL, M. A schur complement method for optimum experimental design in the presence of process noise. In *IFAC World Congress* (Jul 2017), Elsevier.
- [25] CHEN, R. T. Input design for aircraft parameter identification: Using time-optimal control formulation. Tech. rep., Advisory Group for Aerospace Research & Development (AGARD): Methods for Aircraft State and Parameter Identification, 1975.
- [26] CIMEN, T. Workshop on flight dynamics, simulation and control with matlab and simulink. IFAC World Conference, Toulouse, France, Jul 2017.

- [27] COBLEIGH, B. R. *Design of optimal inputs for parameter estimation flight experiments with application to the X-31 drop model*. PhD thesis, George Washington University, 1991.
- [28] COLEMAN, J., AHMAD, H., PICAN, E., AND TOAL, D. Non-reversing generators in a novel design for pumping mode airborne wind energy farm. In *Airborne wind energy*. Springer, 2013, pp. 587–597.
- [29] COOK, M. *Flight Dynamics Principles: A Linear Systems Approach to Aircraft Stability and Control*, 3rd ed. Elsevier, 2013.
- [30] DE JONG, R., AND MULDER, J. Accurate estimation of aircraft inertia characteristics from a single suspension experiment. *Journal of Aircraft* 24, 6 (1987), 362–370.
- [31] DIEHL, M. Airborne wind energy: Basic concepts and physical foundations. In *Airborne Wind Energy*. Springer, 2013, pp. 3–22.
- [32] DIEHL, M. *Modeling and System Identification*. University of Freiburg, 2017.
- [33] DIEHL, M., AND GROS, S. *Numerical Optimal Control*. University of Freiburg, 2017.
- [34] DIEHL, M., SCHMEHL, R., AND AHRENS, U. *Airborne Wind Energy. Green Energy and Technology*. Springer Berlin Heidelberg, 2014.
- [35] DOROBANTU, A., MURCH, A., METTLER, B., AND BALAS, G. System identification for small, low-cost, fixed-wing unmanned aircraft. *Journal of Aircraft* 50, 4 (2013), 1117–1130.
- [36] ENRIGHT, P. J., AND CONWAY, B. Discrete approximations to optimal trajectories using direct transcription and nonlinear programming. *Journal of Guidance, Control, and Dynamics* 15, 4 (1992), 994–1002.
- [37] ETKIN, B. *Dynamics of Atmospheric Flight*. Wiley, 1972.
- [38] FAGIANO, L. *Control of Tethered Airfoils for High Altitude Wind Energy Generation*. PhD thesis, Politecnico di Torino, 2009.
- [39] FAGIANO, L., AND MILANESE, M. Airborne wind energy: An overview. In *American Control Conference (ACC)* (June 2012), pp. 3132–3143.
- [40] FASEL, U., KEIDEL, D., MOLINARI, G., AND ERMANNI, P. Aerostructural optimization of a morphing wing for airborne wind energy applications. *Smart Materials and Structures* 26, 9 (2017), 095043.

- [41] GEEBELEN, K., VUKOV, M., ZANON, M., GROS, S., WAGNER, A., DIEHL, M., VANDEPITTE, D., SWEVERS, J., AND AHMAD, H. An experimental test setup for advanced estimation and control of an airbornewind energy system. In *Airborne wind energy*. Springer, 2013, pp. 459–471.
- [42] GERLACH, O. The determination of stability derivatives and performance characteristics from dynamic manoeuvres (report vth-163). Tech. rep., Delft University of Technology, Department of Aeronautical Engineering, Mar 1971.
- [43] GERLACH, O. H. Analysis of a possible method for the measurement of performance and stability and control characteristics in non-steady symmetrical flight (report vth-117). Tech. rep., Delft University of Technology, Faculty of Aerospace Engineering, 1964.
- [44] GILLIS, J., GOOS, J., GEEBELEN, K., SWEVERS, J., AND DIEHL, M. Optimal periodic control of power harvesting tethered airplanes: how to fly fast without wind and without propellor? In *American Control Conference (ACC)* (2012), IEEE, pp. 2527–2532.
- [45] GOMAN, M., AND KHRABROV, A. State-space representation of aerodynamic characteristics of an aircraft at high angles of attack. *Journal of Aircraft* 31, 5 (1994), 1109–1115.
- [46] GROS, S. Numerical optimal control with differential algebraic equations. <https://www.syscop.de/teaching/ws2015/nocdae>, Feb 2016.
- [47] GROS, S., AND DIEHL, M. Modeling of airborne wind energy systems in natural coordinates. In *Airborne wind energy*. Springer, 2013, pp. 181–203.
- [48] GROS, S., ZANON, M., AND DIEHL, M. A relaxation strategy for the optimization of airborne wind energy systems. In *European Control Conference (ECC)* (2013), IEEE, pp. 1011–1016.
- [49] GROS, S., ZANON, M., VUKOV, M., AND DIEHL, M. Nonlinear mpc and mhe for mechanical multi-body systems with application to fast tethered airplanes. In *Nonlinear Model Predictive Control Conference* (Aug 2012), Elsevier, pp. 86–93.
- [50] GUPTA, N. K., AND HALL JR, W. E. Input design for identification of aircraft stability and control derivatives. Tech. rep., NASA, Feb 1975.
- [51] HARGRAVES, C. R., AND PARIS, S. W. Direct trajectory optimization using nonlinear programming and collocation. *Journal of Guidance, Control, and Dynamics* 10, 4 (1987), 338–342.

- [52] HEILMANN, J., AND HOULE, C. Economics of pumping kite generators. In *Airborne Wind Energy*. Springer, 2013, pp. 271–284.
- [53] HOAK, D., AND FINCK, R. *USAF Stability and Control DATCOM*. National Technical Information Service, 1975.
- [54] HORN, G., GROS, S., AND DIEHL, M. Numerical trajectory optimization for airborne wind energy systems described by high fidelity aircraft models. In *Airborne wind energy*. Springer, 2013, pp. 205–218.
- [55] HOUSKA, B., AND DIEHL, M. Optimal control for power generating kites. In *European Control Conference (ECC) (2007)*, IEEE, pp. 3560–3567.
- [56] HSL. A collection of fortran codes for large scale scientific computation. <http://www.hsl.rl.ac.uk/>, 2017.
- [57] IEC. Wind energy generation systems - part 12-1: Power performance measurements of electricity producing wind turbines. <https://webstore.iec.ch/publication/26603#additionalinfo>, 2018.
- [58] JATEGAONKAR, R., FISCHENBERG, D., AND VON GRUENHAGEN, W. Aerodynamic modeling and system identification from flight data-recent applications at dlr. *Journal of Aircraft* 41, 4 (2004), 681–691.
- [59] KIEFER, J., AND WOLFOWITZ, J. Optimum designs in regression problems. *The Annals of Mathematical Statistics* 30, 2 (1959), 271–294.
- [60] KIEFER, J., AND WOLFOWITZ, J. The equivalence of two extremum problems. *Canadian Journal of Mathematics* 12, 5 (1960), 363–365.
- [61] KOEHLER, R., AND WILHELM, K. Auslegung von eingangssignalen für die kennwertermittlung. *DFVLR-IB* (1977), 154–77.
- [62] KOENEMANN, J. Openawe – open Airborne Wind Energy. <https://openawe.github.io/>, 2017.
- [63] KOENEMANN, J. Openocl – open Optimal Control Library. <http://www.openocl.org/>, 2017.
- [64] KOENEMANN, J., AND LICITRA, G. Flight Trajectories Optimization of Rigid Wing Pumping Mode awes. <https://github.com/openawe/openawe>, 2017.
- [65] KOENEMANN, J., WILLIAMS, P., SIEBERLING, S., AND DIEHL, M. Modeling of an airborne wind energy system with a flexible tether model for the optimization of landing trajectories. *IFAC-PapersOnLine* 50, 1 (2017), 11944–11950.

- [66] KOENEMANN, J., WILLIAMS, P., SIEBERLING, S., AND DIEHL, M. Modeling of an airborne wind energy system with a flexible tether model for the optimization of landing trajectories. In *IFAC 2017 World Congress* (July 2017), Elsevier, pp. 11944–11950.
- [67] KRUIJFF, M., AND RUITERKAMP, R. A roadmap towards airborne wind energy in the utility sector. In *Airborne Wind Energy, Green Energy and Technology*. Springer Nature Singapore Pte Ltd, 2018.
- [68] LANDBERG, L. *Meteorology for Wind Energy: An Introduction*. John Wiley & Sons, 2015.
- [69] LELOUP, R., RONCIN, K., BLES, G., LEROUX, J.-B., JOCHUM, C., AND PARLIER, Y. Estimation of the lift-to-drag ratio using the lifting line method: Application to a leading edge inflatable kite. In *Airborne Wind Energy*. Springer, 2013, pp. 339–355.
- [70] LICITRA, G., BÜRGER, A., WILLIAMS, P., RUITERKAMP, R., AND DIEHL, M. Optimum experimental design of a rigid wing awe pumping system. In *56th Conference on Decision and Control (CDC)* (Dec 2017), IEEE.
- [71] LICITRA, G., KOENEMANN, J., HORN, G., WILLIAMS, P., RUITERKAMP, R., AND DIEHL, M. Viability assessment of a rigid wing airborne wind energy pumping system. In *21st International Conference on Process Control (PC)* (Jul 2017), IEEE, pp. 452–458.
- [72] LICITRA, G., SIEBERLING, S., ENGELEN, S., WILLIAMS, P., RUITERKAMP, R., AND DIEHL, M. Optimal control for minimizing power consumption during holding patterns for airborne wind energy pumping system. In *European Control Conference (ECC)* (Jan 2016), IEEE, pp. 1574–1579.
- [73] LICITRA, G., WILLIAMS, P., GILLIS, J., GHANDCHI, S., SIEBERLING, S., RUITERKAMP, R., AND DIEHL, M. Aerodynamic parameter identification for an airborne wind energy pumping system. In *IFAC 2017 World Congress* (July 2017), Elsevier, pp. 11951–11958.
- [74] LJUNG, L. *System identification: Theory for the User*. Prentice Hall PTR, 1998.
- [75] LOYD, M. L. Crosswind kite power (for large-scale wind power production). *Journal of Energy* 4, 3 (1980), 106–111.
- [76] LUCHSINGER, R. H. Pumping cycle kite power. In *Airborne wind energy*. Springer, 2013, pp. 47–64.

- [77] LUISE, M., AND VITETTA, G. *Teoria dei Segnali, seconda edizione*. The McGraw-Hill Companies, 2003.
- [78] LYONS, D. Obtaining optimal results with filar pendulums for moment of inertia measurements. *Society of Allied Weight Engineers* 62, 2 (2002), 5–20.
- [79] MANWELL, J. F., MCGOWAN, J. G., AND ROGERS, A. L. *Wind energy explained: theory, design and application*. John Wiley & Sons, 2010.
- [80] MARCHAND, M. Untersuchung der bestimmbarkeit der flugmechanischen derivative des ccv-versuchsträgers f-104 g. Tech. rep., DFVLR IB, 1977.
- [81] MASTERS, G. M. *Renewable and Efficient Electric Power Systems*. John Wiley & Sons, 2013.
- [82] MCRUER, D. T., GRAHAM, D., AND ASHKENAS, I. *Aircraft Dynamics and Automatic Control*. Princeton University Press, 2014.
- [83] MEHRA, R., AND EUPTA, N. K. Status of input design for aircraft parameter identification. Tech. rep., Advisory Group for Aerospace Research & Development (AGARD): Methods for Aircraft State and Parameter Identification, 1974.
- [84] MEHRA, R. K. Frequency-domain synthesis of optimal inputs for multiinput-multioutput (mimo) systems with process noise. In *Conference on Decision and Control (CDC)* (Nov 1974), IEEE, pp. 410–418.
- [85] MEHRA, R. K. Time-domain synthesis of optimal inputs for system identification. In *Conference on Decision and Control (CDC)* (Nov 1974), IEEE, pp. 480–487.
- [86] MORELLI, E., AND KLEIN, V. Optimal input design for aircraft parameter estimation using dynamic programming principles. In *Atmospheric Flight Mechanics Conference* (Aug 1990), AIAA.
- [87] MORELLI, E. A. *Practical Input Optimization for Aircraft Parameter Estimation Experiments*. National Aeronautics and Space Administration, Langley Research Center, 1993.
- [88] MORELLI, E. A. Practical aspects of the equation-error method for aircraft parameter estimation. In *Atmospheric Flight Mechanics Conference* (Aug 2006), vol. 6144, AIAA.
- [89] MULDER, J. Design and evaluation of dynamic flight test manoeuvres (report lr-497). Tech. rep., Delft University of Technology, Faculty of Aerospace Engineering, 1986.

- [90] MULDER, J., SRIDHAR, J., AND BREEMAN, J. *Identification of Dynamic System - Application to Aircraft. Part 2: Nonlinear Analysis and Manoeuvre Design*. Advisory Group for Aerospace Research & Development (AGARD), 1994.
- [91] MULDER, J., VAN STAVEREN, W., AND VAN DER VAART, J. *Flight dynamics (lecture notes)*. TU Delft, 2000.
- [92] NAHI, N., AND WALLIS, D. Optimal inputs for parameter estimation in dynamic systems with white observation noise. In *10th Joint Automatic Control Conference* (Aug 1969).
- [93] NAHI, N. E., AND NAPJUS, G. A. Design of optimal probing signals for vector parameter estimation. In *Conference on Decision and Control (CDC)* (Dec 1971), IEEE, pp. 162–168.
- [94] NODERER, K. *Analysis of the aerodynamics characteristics of the X-31 model obtained from flight tests data*. PhD thesis, George Washington University, 1992.
- [95] RUITERKAMP, R., AND SIEBERLING, S. Description and preliminary test results of a six degrees of freedom rigid wing pumping system. In *Airborne wind energy*. Springer, 2013, pp. 443–458.
- [96] SAMORANI, M. *The wind farm layout optimization problem*. Springer, 2013.
- [97] SCHULZ, V. H., BOCK, H. G., AND STEINBACH, M. C. Exploiting invariants in the numerical solution of multipoint boundary value problems for dae. *SIAM journal on scientific computing* 19, 2 (1998), 440–467.
- [98] SODERSTROM, T., AND STOICA, P. *System Identification*. Prentice-Hall, 2001.
- [99] STEVENS, B. L., LEWIS, F. L., AND JOHNSON, E. N. *Aircraft Control and Simulation: Dynamics, Controls Design, and Autonomous Systems*. Wiley, 2015.
- [100] STUYTS, J., HORN, G., VANDERMEULEN, W., DRIESEN, J., AND DIEHL, M. Effect of the electrical energy conversion on optimal cycles for pumping airborne wind energy. *IEEE Transactions on Sustainable Energy* 6, 1 (2015), 2–10.
- [101] TISCHLER, M. B., AND REMPLE, R. K. *Aircraft and Rotorcraft System Identification*. AIAA Education Series, 2006.

- [102] TOBAK, M., AND SCHIFF, L. B. On the formulation of the aerodynamic characteristics in aircraft dynamics. Tech. rep., NASA, 1976.
- [103] VERSTEEG, H. K., AND MALALASEKERA, W. *An introduction to computational fluid dynamics - the finite volume method*. Addison-Wesley-Longman, 1995.
- [104] WÄCHTER, A., AND BIEGLER, L. T. On the implementation of an interior-point filter line-search algorithm for large-scale nonlinear programming. *Mathematical Programming* 106, 1 (2006), 25–57.
- [105] WILLIAMS, P., LANSDORP, B., AND OCKELS, W. Modeling and control of a kite on a variable length flexible inelastic tether. In *Guidance, navigation and control conference (2007)*, AIAA.
- [106] WILLIAMS, P., LANSDORP, B., AND OCKESL, W. Optimal crosswind towing and power generation with tethered kites. *Journal of Guidance, Control, and Dynamics* 31, 1 (2008), 81–93.
- [107] WILLIAMS, P., AND TRIVAILO, P. Dynamics of circularly towed aerial cable systems, part 2: Transitional flight and deployment control. *Journal of Guidance, Control, and Dynamics* 30, 3 (2007), 766–779.
- [108] WILLIAMS, P., AND TRIVAILO, P. Dynamics of circularly towed aerial cable systems, part i: optimal configurations and their stability. *Journal of Guidance, Control, and Dynamics* 30, 3 (2007), 753–765.
- [109] ZANON, M., GROS, S., ANDERSSON, J., AND DIEHL, M. Airborne wind energy based on dual airfoils. *IEEE Transactions on Control Systems Technology* 21, 4 (2013), 1215–1222.
- [110] ZANON, M., GROS, S., AND DIEHL, M. Model predictive control of rigid-airfoil airborne wind energy systems. In *Airborne wind energy*. Springer, 2013, pp. 219–233.

FACULTY OF ENGINEERING
DEPARTMENT OF MICROSYSTEMS ENGINEERING
SYSTEMS CONTROL AND OPTIMIZATION LABORATORY
Georges-Köhler-Allee 101
DE-79110 Freiburg i. Br.

